# MESOPOROUS SPINEL-TYPE COBALT OXIDE, COBALT FERRITE AND ALUMINA BY NANOCASTING

## DISSERTATION

zur Erlangung des Grades

'Doktor der Naturwissenschaften'

(Dr. rer. nat.)

der Fakultät für Naturwissenschaften

der Universität Paderborn

vorgelegt von

STEFANIE HAFFER

Paderborn, November 2013

Die vorliegende Arbeit wurde in der Zeit von April 2009 bis Juni 2010 am Institut für Anorganische und Analytische Chemie der Justus-Liebig-Universität Gießen sowie von Juli 2010 bis Oktober 2013 am Institut für Anorganische und Analytische Chemie der Universität Paderborn in der Arbeitsgruppe von Prof. Dr. Michael Tiemann angefertigt.

Gutachter:             Prof. Dr. Michael Tiemann

                       Prof. Dr. Bernd Smarsly

Tag der Disputation:   17.12.2013

# VERSICHERUNG

Hiermit versichere ich, die vorliegende Arbeit eigenständig und ausschließlich unter Verwendung der angegebenen Hilfsmittel und Quellen durchgeführt zu haben. Die Arbeit ist zuvor keiner Prüfungsbehörde in gleicher oder ähnlicher Form vorgelegt worden.

Paderborn, den 04.11.2013

Stefanie Haffer

## DANKSAGUNG

*Für meine Eltern*

CONTENTS

# 1 INTRODUCTION

## 1.1 Mesoporous Ordered Materials

The interest in research on mesoporous materials has risen enormously since 1992 when the M41S phases were discovered by the Mobil Oil Company with MCM-41 as the most well-known representative of the class of periodically ordered mesoporous silica materials.[1] Mesoporous materials are characterized by pores of a size between 2 and 50 nm according to the IUPAC recommendation classifying porous materials in three categories: micro-, meso- and macroporous materials with pore sizes smaller than 2 nm, between 2 and 50 nm and larger than 50 nm, respectively.[2] Their attractive properties particularly the uniform mesopores make mesoporous materials interesting for potential applications in catalysis, adsorption, sensing, lithium-ion batteries, drug delivery, and nanodevices.[3-12] The synthesis of periodically ordered mesoporous materials usually require the utilization of a porogen, this means an auxiliary species that acts as a template or structure director.[11] For the creation of periodically ordered uniform mesopores generally two synthesis approaches can be distinguished, which will be presented in the following: (i) the surfactant- or block copolymer-directed 'soft templating' method and (ii) the silica- or carbon-based 'hard templating' method.

### 1.1.1 Synthesis by 'Soft Templating'

In the 'soft templating' approach supramolecular aggregates of amphiphilic species (surfactants, block copolymers, *etc.*) serve as porogens while the desired product is formed in a sol-gel-based process leading to a mesostructured composite material with the porogen incorporated as schematically displayed in Figure 1, (a). Removal of the latter one by calcination or extraction yields the mesoporous product (b). This synthesis concept is considered in a couple of literature reviews.[5,13-17]

One of the most important aspects for a successful synthesis is a controllable hydrolysis-condensation behavior of the precursor species; a favorable interaction between porogen and precursor is a prerequisite for yielding an ordered mesostructure while phase separation needs to be avoided. For the formation process of the mesostructured composite material

two alternative mechanisms were found to be relevant: (i) a true liquid-crystal templating (TLCT) and (ii) a cooperative liquid-crystal templating. In case of the first one the concentration of the surfactant is high enough for a lyotropic liquid-crystalline phase forming already without the presence of the precursor. However, a structure formation is also possible at lower surfactant concentrations by a cooperative self-assembly involving both the porogen and the precursor species which has already been added.
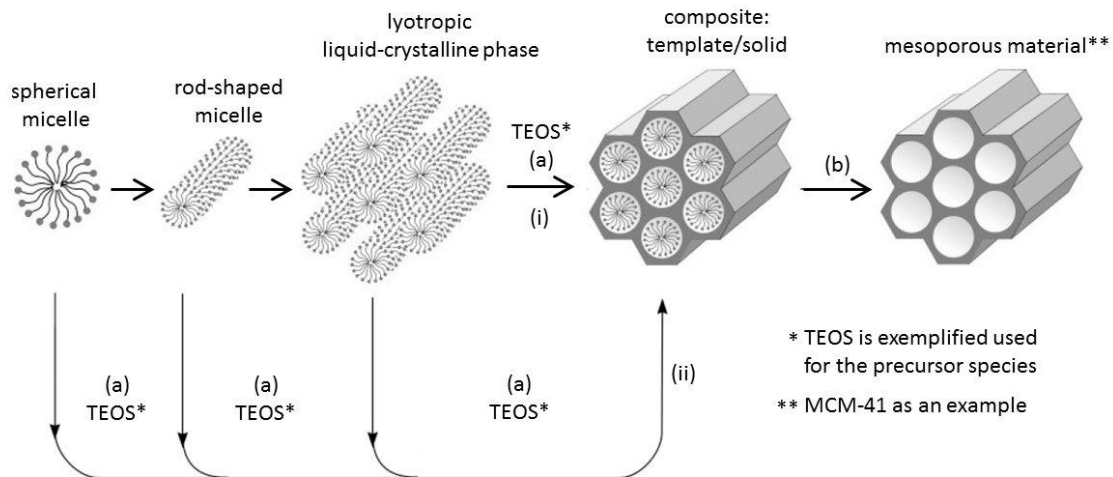


**Figure 1.** Schematic drawing of the synthesis of mesoporous materials by 'soft templating' via a (i) true liquid-crystal templating (TLCT) or (ii) cooperative liquid-crystal templating: after addition of the precursor compound a composite with the porogen incorporated is formed (a), while removal of the latter one yield the mesoporous product (b);modified from reference.[16]

This sol-gel based synthesis method has turned out to be successful particularly for systems that preferably form amorphous phases at moderate temperature. For instance, silica with its flexible Si-O-Si bond angle tends to form solid phases with only corner-sharing $SiO_4$ tetrahedral units without crystallizing under the prevailing conditions during the 'soft templating' synthesis. This is advantageous since amorphous silica can easily adapt to the curvature of the mesopore channels. Thus, numerous mesoporous silica phases, like MCM-41,[1,18,19] MCM-48,[19] SBA-15,[20,21] SBA-16,[21] or KIT-6[22] can be synthesized by the 'soft templating' method. In this thesis the following two, block-copolymer based, ordered mesoporous silica materials are utilized: (i) SBA-15 and (ii) KIT-6 silica, both schematically displayed in Figure 2.
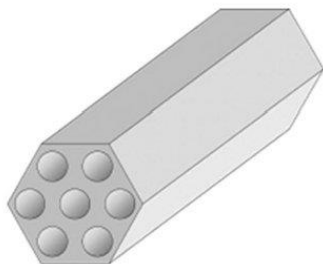
**SBA-15**                                                      **KIT-6**
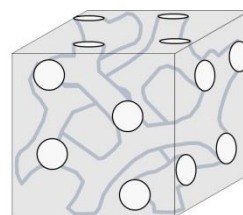


**Figure 2.** Schematic drawing of mesoporous silica materials with hexagonal (left) and cubic (right) ordered pore system symmetry existing in SBA-15 and KIT-6 silica, respectively.

The SBA-15 silica phase (left) consists of uniform linear cylindrical mesopore channels in a hexagonally ordered arrangement (*p6mm*). In comparison, KIT-6 silica (right), the cubic analogue to SBA-15, contains an enantiomeric pair of interpenetrating branched networks of mesopore channels with cubic ordered pore system symmetry ($Ia\bar{3}d$).[22] The mesopores of both silica phases are interconnected by micropores or small mesopores which are distributed inside the pore walls in a disordered way. The pore size can be systematically varied between 4 and 12 nm depending on the synthesis temperature or duration for the hydrothermal treatment.[20,22] The pore size can also be increased by changing the copolymer, particularly by varying the block size of the copolymer, or by addition of an organic species as a swelling agent, such as 1,3,5-trimethylbenzene (TMB), even to about 30 nm while the periodic structure is still retained.[20]

In contrast to the amorphous silica phases, most metal oxides have the tendency to form dense crystalline phases with high lattice energies even at low temperature, frequently associated with phase-separation from the organic amphiphiles. Further reasons, why this method cannot be employed universally for ordered, mesoporous materials in general may be the lack of appropriate precursor compounds, or the redox activity during the removal of the organic species by thermal combustion resulting in a collapse of the solid's mesostructure.[11,23] As a consequence, only a limited number of non-siliceous systems are accessible by this approach, such as mesoporous carbon,[24] and some metal oxides.[13,25-28]

The 'soft templating' method mostly results in mesoporous powders without defined particle morphology. However some techniques are available to obtain the mesoporous materials with a defined shape. For instance, mesoporous films or membranes can be synthesized by the 'evaporation-induced self-assembly' (EISA) method.[29,30] Furthermore the preparation of

monoliths of variable size and shape is facilitated.[31-33] Both methods have been shown to be also applicable to some mesoporous metal oxides.[34-41]

Table 1 gives an overview of metal oxides that are accessible by the 'soft templating' method.

**Table 1.** Overview of mesoporous metal oxides obtained by 'soft templating'.

| soft templating | binary | $TiO_2$,[25,26, 42,43] $ZrO_2$,[25,26,43] $Al_2O_3$,[25,26,43-47] $SnO_2$,[25,26,48] $WO_3$,[25,26] $Nb_2O_5$,[25,26] $Ta_2O_5$,[25,26,] $HfO_2$,[25,26] |
|---|---|---|
| | ternary | $SiAlO_x$,[25,26] $Al_2TiO_x$,[25,26] $ZrTiO_x$,[25,26] $SrTiO_x$,[25,26] $ZrW_2O_x$,[25,26] $ZnTiO_3$,[49] $SrTiO_3$,[50] $BaTiO_3$,[50] $BiFeO_3$[51] |

## 1.1.2 Synthesis by 'Hard Templating'

An alternative synthesis approach to prepare mesoporous materials which avoids the before-mentioned problems is by the 'hard templating' route which is also referred to as 'nanocasting'.[10,23,52-58] This method facilitates the approach to a much larger variety of mesoporous materials, including carbon,[53,57,58] metal oxides,[10,23,52-55] and organic materials.[56] Figure 3 shows a schematic drawing of the structure replication concept. The desired product is formed *in situ* in the pores of a structure matrix ('hard template'), most frequently silica (a), which is selectively removed afterwards to yield the product as the negative replica of the matrix (b). However, for some metal oxides, especially for those that are not resistant against the prevailing chemical conditions (etching) applied for the removal of the silica matrix, two structure replication steps are required via a first replication step. In this first step of 'hard templating' mesoporous carbon is obtained which is afterwards used as structure matrix for the second replication procedure (c, d).
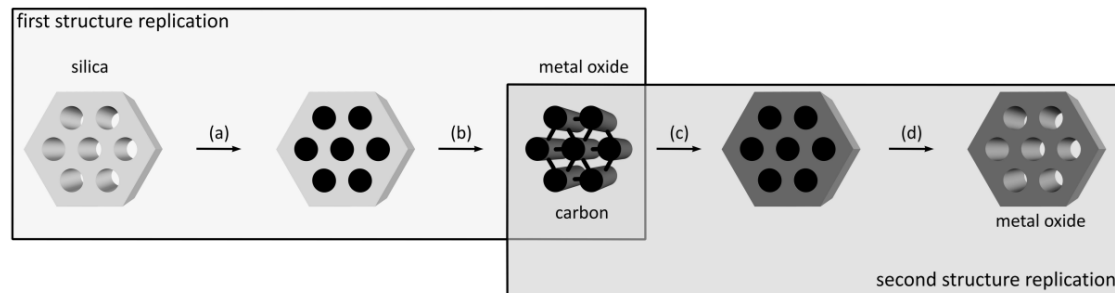
**Figure 3.** Schematic drawing of the synthesis by nanocasting of mesoporous metal oxides, obtained after one or two structure replication procedures: the desired product is formed inside the pores of a silica matrix (a), which is removed afterwards yielding the product as a negative replica (b). A carbon replica can also serve as structure matrix for a second replication procedure (c, d), which is useful when metal oxides are not resistant against the conditions employed for the removal of the silica matrix.[11]

Thus, both mesoporous silica and mesoporous carbon materials can be utilized as structure matrices for the synthesis of mesoporous metal oxides. While the former ones, such as MCM-48, SBA-15, or KIT-6 are obtained by the 'soft templating' method in a preceding synthesis step, the carbon materials like CMK-3, or CMK-8 are synthesized via 'hard templating' by replication from SBA-15 or KIT-6, respectively. For pore filling metal salts are frequently used as precursor compounds for metal oxides which are thermally converted into the desired product. Since the conversion from metal nitrate into the respective metal oxide goes along with substantial volume shrinkage,[59,60] these steps of infiltration and subsequent conversion into the product usually need to be repeated more than once ensuring a more sufficient pore filling in the matrix. After the last cycle of impregnation and conversion into the product the structural mold is removed. This is accomplished either by etching with hydrofluoric acid (HF) or with a strong base, *e.g.* concentrated sodium hydroxide (NaOH) solution in case of a silica matrix or by thermal combustion when carbon is used as structural mold.

The infiltration of the precursor compound into the pores of the matrix is one of the key factors for a successful structure replication procedure to yield an ordered mesoporous replica material; structurally stable products can only be formed when sufficiently large fractions of the pores get filled.[11] Even if the pores are initially filled entirely with the precursor compound after the conversion into the product only 5-15 % of the pore volume is filled;[59] this means that parts of the pores remain empty. However, in contrast, it has to be considered that an excess of precursor should also be avoided since deposition outside the pores of the matrix will take place, which results in formation of non-porous material.

Therefore, various impregnation techniques have been developed for an optimized pore filling.[11] Particularly, the following three methods are the most employed ones: impregnation by using (i) a metal salt solution, (ii) solvent free melts of the precursor, or (iii) two solvents;[11] the different techniques are schematically displayed in Figure 4.
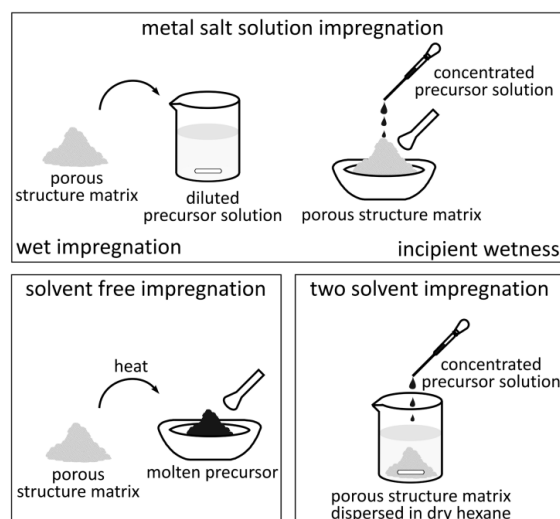


**Figure 4.** Schematic drawing of different methods for infiltrating the pores of a structure matrix with the precursor compound during the synthesis by nanocasting.[11]

When applying metal salt solutions (Figure 4, above) two methods are established depending on the concentration of the precursor solution, the 'wet impregnation' and the 'incipient wetness' technique.[23,61-65] In case of the former one the powdery structure matrix is dispersed in a diluted solution of precursor compound so that the solute species can diffuse into the pores and remain adsorbed at the pore walls after solvent evaporation. The degree of pore filling employing this method is rather low and several impregnation steps are usually required. However, the 'wet impregnation' method bears the advantage of only low precursor deposition outside the pores of the matrix. Contrary to that, by the 'incipient wetness' technique a saturated precursor solution is employed for impregnation instead, which improves the loading of the pores but also the amount of deposited precursor species at the outer surface of the matrix may be promoted. In this approach, only a definite volume is used, which corresponds to the total pore volume of the matrix, to avoid formation of non-porous material due to deposition at the outer surface of the matrix. A still more efficient loading of the pores up to the theoretical optimum is facilitated by completely avoiding a solvent in the 'solvent free impregnation' (also called 'solid-liquid') method (Figure 4, left).[66-69] However, some metal salts, especially the low melting ones, often

contain some crystal water, which means that (solvent-free) melts of such precursors still include certain amounts of water. Finally, in the 'two solvent impregnation' method (Figure 4, right), the structure matrix is initially dispersed in a non-polar solvent (*e.g.* hexane) while the precursor dissolved in a polar solvent is added drop-wise, thereby replacing the non-polar solvent inside the pores.[70,71] This method may result in a more uniform pore filling. In case of mesoporous carbon serving as the structure matrix it may be beneficial when the precursor compound is dissolved in a less polar solvent due to the non-polar surface of the carbon even though this is accompanied by a reduced solubility of the metal salts.[65] Apart from these impregnation methods supercritical fluids,[72] ultrasonication,[73] or vapor-phase infiltration[74] are sometimes utilized.

The obtained products of the nanocasting procedure possess ordered mesopore systems, high specific surface areas, and usually crystalline pore walls, as well as high thermal stability. The two latter aspects are particularly relevant with respect to many potential applications of these materials, *e.g.* gas sensing or catalysis.[6,11,23] Compared to products obtained by 'soft templating' with poor or no crystallinity at all and with low thermal stability, the 'nanocasting' procedure facilitates the formation of mesoporous materials with high degree of crystallinity. The increased crystallinity is caused by the higher temperature that can be applied for the conversion of the precursor into the desired product in comparison to those employed during the synthesis by the 'soft templating' method; the structure matrix serve as a rigid skeleton, preventing collapse of the mesostructure. The thermal treatment at higher temperatures is further associated with a higher thermal stability of the products after the matrix removal. This makes 'nanocasting' an advantageous synthesis method for mesoporous materials, especially metal oxides, as compared to the 'soft templating' method, even accepting that the structure replication procedure comprises two or three synthesis steps since the structure matrix also needs to be prepared in a preceding synthesis step.

Furthermore, the 'nanocasting' procedure provides opportunities to control structural properties like pore size, pore wall thickness, and specific surface area, as well as particle size and morphology to some degree, which is also relevant for application of these materials.[75-78] With respect to the morphology and particle size a well-defined morphology can be transferred from the structure matrix to the replica particles (Figure 5, a). For

instance, micrometer-sized porous silica spheres have been shown to lead to porous replica particles of the same size and shape,[76] or mesoporous carbon rods were obtained by replication of silica rods.[79] Apart from this direct relation between size and morphology of the matrix on the one hand and the replica on the other hand a well-defined morphology may also be possible even when the structure matrix does not have a well-defined particle morphology, *i.e.* without a direct relation between the particles of the matrix and of the resulting replica. For example, it was shown that mesoporous $In_2O_3$ particles with spherical or ellipsoidal morphology are obtained by using KIT-6 or SBA-15 silica structure matrices, respectively, which do not have a defined morphology by their own (Figure 5, b). Here, the uniform morphology of the $In_2O_3$ replica particles was shown to originate from a special growth/formation mechanism inside the pores of the matrix.[80] Additionally, it was reported that variation of the ambient atmosphere during the conversion into the product may also influence the particle size and morphology as well as the crystallinity of the replica materials to some degree.[59]
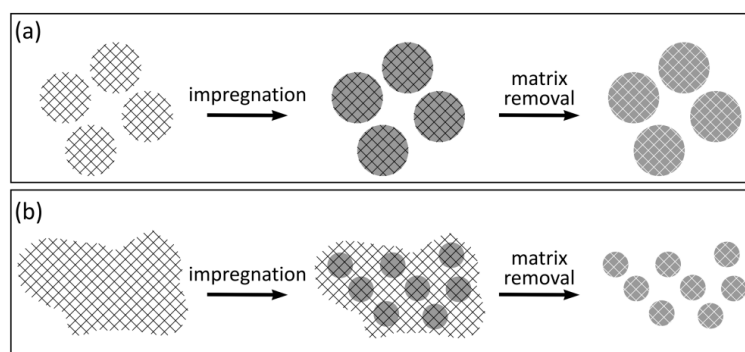


**Figure 5.** Schematic drawing for obtaining replica particles with defined (spherical) morphology during a nanocasting procedure utilizing a structure matrix with (a) or without (b) defined morphology.[11]

To date a large number of ordered mesoporous binary metal oxides, such as $Co_3O_4$, $In_2O_3$, $SnO_2$, $ZnO$, $Al_2O_3$, $MgO$, $Fe_2O_3$ or $NiO$, for example, have been prepared by this method. Recently this approach was shown to be also successful for the synthesis of ternary metal oxides, including spinel-type systems, like $CoFe_2O_4$, $NiFe_2O_4$, $NiCo_2O_4$, and $MnCo_2O_4$, as well as perovskites, like $LaCoO_3$, $LiFeO_3$, and $LaMnO_3$. Ternary or multimetal oxides in general, which contain more than one type of metal cation, are often characterized by superior properties as compared to the binary systems.[81,82,83] For instance, the ferrimagnetic coercivity of pure (binary) $\gamma$-$Fe_2O_3$ is substantially enhanced by modifying the metal oxide with cobalt; in case of $Co_3O_4$ the catalytic activity can be enhanced by partial substitution

with other 3*d*- transition metals. However, the synthesis of mesoporous ternary systems by nanocasting is more challenging than for binary systems due to the requirement of controlling the composition, stoichiometry and crystal structure, *etc*.[84,85,86]

Table 2 displays an overview of some metal oxide systems including binary and ternary ones that have been successfully synthesized by 'nanocasting'.

**Table 2.** Overview of mesoporous metal oxides obtained by 'nanocasting' during a one-step or two-step structure replication procedure.

| | | |
|---|---|---|
| one-step nanocasting with silica matrix (SBA-15 and KIT-6) | binary | $Co_3O_4$,[62,63,87-92] $In_2O_3$,[62,80,93,94] $Mn_xO_y$,[61,71,75] $SnO_2$,[60,69,75,95-97] $CeO_2$,[61,64,98-100] $NiO$,[61,91,101] $WO_3$,[98,102] $Cr_2O_3$,[61,63,103,104] $Fe_2O_3$,[61,105] $TiO_2$,[106] $RuO_2$[107] |
| | ternary | $CoFe_2O_4$,[84,92,108] $CuFe_2O_4$,[109] $NiFe_2O_4$,[108-110] $CuAl_2O_4$,[111] $NiAl_2O_4$,[111] $MgAl_2O_4$,[111] $FeAl_2O_4$,[111] $CuCo_2O_4$,[82] $MnCo_2O_4$,[82] $NiCo_2O_4$,[82,83,91] $MgFe_2O_4$,[108] $ZnFe_2O_4$,[112] $LaCoO_3$,[86,113,114] $LaFeO_3$,[86,115] $LaMnO_3$[86] |
| two-step nanocasting with carbon matrix (CMK-3 and CMK-8) | binary | $Al_2O_3$,[116-118] $MgO$,[119,120] $ZnO$,[121-123] $CeO_2$,[124] $CuO$[125] |

## 1.2  Metal Oxide Systems

In the following the metal oxide systems that are relevant to this thesis will be concisely described, particularly with respect to their crystalline structure, properties and applications.

### 1.2.1  Cobalt Oxide

Cobalt (II,III) oxide is the thermodynamically most stable form of cobalt oxide. In contrast to the rock-salt like structure of cobalt (II) oxide (CoO), $Co_3O_4$ crystallizes in the 'normal' spinel structure with two distinct kinds of cobalt ions, $Co^{2+}$ and $Co^{3+}$. Figure 6 displays the unit cell of a 'normal' spinel. The conventional unit cell of spinel structures consists of 56 atoms comprising 8 tetrahedrally ($Co^{2+}$), 16 octahedrally coordinated ions ($Co^{3+}$) and 32 $O^{2-}$ ions.

According to the 'normal' spinel structure of $Co_3O_4$, the oxide ions form a cubic closed-packed (*fcc*) arrangement, one-eighth of the tetrahedral interstices are occupied by the bivalent ions ($Co^{2+}$) while the trivalent ones ($Co^{3+}$) reside in one-half of the octahedral interstices.[126]
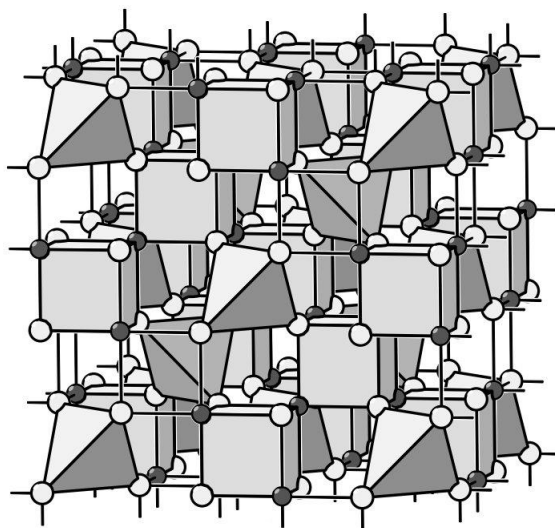


**Figure 6.** The cubic unit cell of a 'normal' spinel structure; the octahedrally coordinated ions ($Co^{3+}$) are denoted by the dark gray spheres, while the bivalent ions ($Co^{2+}$) are in the center of the tetrahedral; the $O^{2-}$ are represented by the white spheres; modified from reference.[127]

In contrast to the iron analogue $Fe_3O_4$ with the same spinel structure, $Co_3O_4$ as an antiferromagnet does not have a permanent magnetic moment. Below the Néel temperature (about 40 K; see 4.2.4.1) a transition from paramagnetic behavior to the ordered antiferromagnetic state occurs associated with a change from the high-temperature modification ($Fd\overline{3}m$) to the low-temperature one ($F4\overline{3}m$), where each $Co^{2+}$ ion is surrounded by four neighbors with oppositely oriented spins. The magnetic moment of $Co_3O_4$ only results from the $Co^{2+}$ ions, while the $Co^{3+}$ ones do not have a permanent moment due to the splitting of the $3d$ levels in an octahedral crystal field with entirely filled $t_{2g}$ levels $(t_{2g})^6$ compared to $(e)^4(t_2)^3$ for the tetrahedrally coordinated $Co^{2+}$ ions. Based on this electronic configuration the total spins are $S = 0$ and $S = 3/2$ for the $Co^{3+}$ and $Co^{2+}$ ions, respectively.[128]

Contrary to rock salt-like cobalt (II) oxide which is an insulator with a band gap of 6 eV, the cobalt (II,III) spinel is a *p*-type semiconductor with an (indirect) band gap between 1.6 and 2.2 eV.[129] $Co_3O_4$ represents an important semiconducting material which is of great interest due to its prominent applications in various fields, mostly in heterogeneous catalysis, electrochemical devices and gas sensing.[130] For instance, $Co_3O_4$ is one of the most suitable

metal oxide catalysts for CO oxidation even at low temperatures, thus rendering it as alternative to the rare and expensive precious metals, the most efficient CO active catalysts.[131-135] Apart from the prominent catalytic activity towards CO, cobalt (II,III) oxide also shows good performance as an electrocatalyst for water splitting.[136] Furthermore, the properties of $Co_3O_4$ make it attractive for gas-sensing applications at low temperatures, in particular for CO monitoring,[137-140] but also for ethanol,[141,142] methane, hydrogen, ammonia and nitrogen dioxide.[138] $Co_3O_4$ is further used as an anode material in lithium ion batteries.[142-144] It shows superior electrochemical performance with high capacity for reversible lithium storage up to three times larger compared to graphite electrodes [130,144]

## 1.2.2  Cobalt Iron Oxide

Cobalt iron oxide (cobalt ferrite) crystallizes in a spinel structure between the 'normal' and an 'inverse' spinel structure. In an 'inverse' spinel all bivalent ions ($Co^{2+}$) occupy the octahedral sites together with half of the trivalent ions ($Fe^{3+}$), while the other half of those are on tetrahedral sites (which usually are occupied by the bivalent ions in case of a 'normal' spinel). The structure of the 'partial inverse' spinel $CoFe_2O_4$ can be described by the formula $^T(Co_{1-x}Fe_x)^O(Co_xFe_{2-x})O_4$ where T and O represent the tetrahedral and octahedral sites, respectively. In case of a partial inverse structure the spinel is disordered since the bi- and trivalent ions may be randomly distributed, either at tetrahedral or octahedral sites. The cation distribution is characterized by the inversion parameter $x$ in the before-mentioned formula which represents the fraction of tetrahedral sites that are occupied by the bivalent ions ($Co^{2+}$).[145,146]

$CoFe_2O_4$ is a ferrimagnetic material below a Curie temperature of 793 K,[147] in which the spins of the two ferromagnetic sublattices are opposed oriented. Since the magnetizations of the two sublattices are different, a remaining magnetization is observed at zero-field, characteristic of a ferrimagnet. Furthermore, cobalt ferrite possesses high coercivity and moderate saturation magnetization, thus rendering it a well-known hard magnetic material which is particularly applied for high-density digital recording.[81,84,148]

The magnetic properties combined with mechanical and chemical stability make cobalt ferrite also interesting for applications in electronic devices,[149] and biological and clinical applications.[150] Furthermore $CoFe_2O_4$ was shown to exhibit an attractive photoelectric

response in the visible region and photocatalytic activities in degradation of environmental pollutants.[151] Another field of application is the catalysis where cobalt iron oxide is applied as catalyst, *e.g.* for the decomposition of methanol[152] or alkylation reactions.[153,154]

### 1.2.3  Aluminum Oxide

Apart from the thermodynamically stable α-aluminum oxide ('corundum') a number of further, metastable phases, like γ-, δ-, κ-$Al_2O_3$, can be differentiated. In case of α-$Al_2O_3$ the oxygen ions are hexagonally closed-packed while the $Al^{3+}$ are located in two-thirds of the available octahedral interstices in the way that each $Al^{3+}$ ion is surrounded by 6 $O^{2-}$ ions and each $O^{2-}$ ion by 4 $Al^{3+}$ ones. In contrast, γ-$Al_2O_3$ possesses cubic closed-packed arrangement of $O^{2-}$ ions with $Al^{3+}$ ions statistically distributed at both octahedral and tetrahedral interstices while some of those remain vacant which are generally occupied by the bi- and trivalent ions in a 'normal' spinel structure. Thus the structure of γ-$Al_2O_3$ can be regarded as a 'defective' spinel structure.[155-157]

Alumina plays an important role in various industrial processes as a catalyst or more frequently as a support material for the catalysis.[158-162] For instance, γ-$Al_2O_3$ is used as support for hydrodesulfurization (HDS) catalysts to reduce the sulfur concentration in gasoline.[163]

### 1.2.4  Barium Titanium Oxide

Barium titanium oxide (barium titanate) crystallizes in the cubic perovskite structure with the $Ba^{2+}$ ions are located in the center and the $Ti^{4+}$ ions at the corner of cubes with the $O^{2-}$ ions forming octahedra around each $Ti^{4+}$ ion. The unit cell of the cubic perovskite structure is displayed in Figure 7.

However the cubic structure for $BaTiO_3$ ($Pm\overline{3}m$) only exists above 393 K, below this Curie temperature the paraelectric phase of $BaTiO_3$ changes to slightly distorted ferroelectric structures with tetragonal, orthorhombic and rhombohedral symmetries. At 393 K the $BaTiO_3$ structure changes to a tetragonal one with $Ti^{4+}$ moving off-center along a Ti-O bond. This phase exists down to 278 K where a further change occurs with $Ti^{4+}$ ions moving off-center along a diagonal between two Ti-O bonds. At 183 K the orthorhombic structure changes to a rhombohedral one. Such phase transitions due to distortions and

displacements of cations from their ideal sites (*e.g.* $Ti^{4+}$ ions moving from the center of $O^{2-}$-octahedra) as a consequence of the small radius of the $Ti^{4+}$ ions (75 pm) are frequently observed for perovskites and are responsible for the interesting ferroelectric and antiferroelectric behavior of perovskites.[164-166]
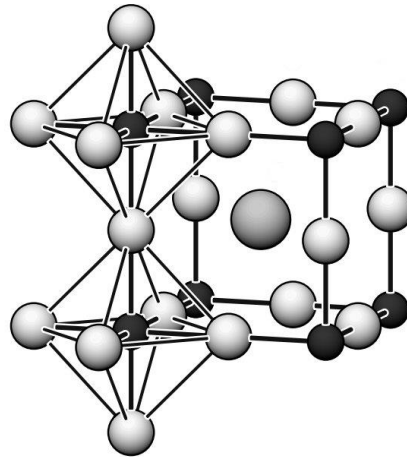


**Figure 7.** The primitive cell of the cubic perovskite structure: $Ba^{2+}$ ions are represented by the dark gray sphere, the $O^{2-}$ by the small light gray ones and the $Ti^{4+}$ions are denoted by the black spheres; modified from reference.[127]

Being one of the most prominent ferroelectric materials with remarkable dielectric properties $BaTiO_3$ plays an important role in the electronics industry. Particularly due to its high dielectric constant $BaTiO_3$ is widely used in multilayer ceramic capacitors and in the recording technology.[164,167-169] $BaTiO_3$ was also shown to be applied as a sensing layer in composite films for $CO_2$ detection.[170]

## 1.3 Multiferroics

Multiferroics are materials that simultaneously show at least two ferroic order phenomena, such as ferromagnetism and ferroelectricity, *i.e.* the spontaneous ordering of spin magnetic moments and electric dipole moments.[171] It should be noted that currently the definition also includes antiferromagnetic ferroelectrics, since the number of ferromagnetic ferroelectrics is only limited.[172] The coupling between their dual order phenomena, known as the 'magnetoelectric effect', makes multiferroic materials very promising for application in data storage, microwave devices, sensors, and transducers, as the magnetic memory can be controlled by an electric field or vice versa. The superior interest of multiferroism

becomes apparent in the number of publications which has enormously increased during the last decade; the development in research is summarized in various reviews.[172-176]

Various strategies exist for obtaining materials with multiferroic properties. In general two types of multiferroics can be principally distinguished: *type-I* materials with ferroelectricity and magnetism of different origins and occurring mostly independently of each other, and *type-II* materials, where magnetism causes ferroelectricity. Materials of the first kind are more abundant and have already been studied in the 1960s when research on multiferroics started, while *type-II* multiferroics are a relatively novel class of materials.

Among *type-I* multiferroics perovskites are the most promising materials. First work attempted to combine ferromagnetic and ferroelectric ordering in single-phase materials. This, however, turns out to be difficult even though a large number of both ferroelectric perovskites and ferromagnetic ones are known, yet without considerable overlap between the two groups. This is attributable to the respective origins of both ordering phenomena. Since ferroelectricity in perovskites is usually caused by transition metal ions like $Ti^{4+}$ or $Ta^{5+}$ with empty *d*-orbitals while magnetism usually requires partially filled *d*- or *f*-orbitals, the two ferroic properties seem to exclude each other. However, some few such perovskites are known, Bismuth ferrite ($BiFeO_3$) being one of the most studied and popular single-phase multiferroics; $BiMnO_3$ and $PbVO_3$ also belong to the rare examples. This seeming violation of the before-mentioned 'exclusion' rule, also referred to as the '$d^0$ vs. $d^n$' problem', can be explained by the fact that the ferroelectricity in case of these exceptions has a different origin compared to that of other perovskites where ferroelectricity is usually a result of instabilities in the structure caused by transition metal ions, such as $Ti^{4+}$ in $BaTiO_3$ (see 1.2.4). Contrary to that, in case of the three mentioned systems it was shown that lone pairs of $Bi^{3+}$ or $Pb^{2+}$ ions are responsible for the ferroelectricity by being displaced from their centrosymmetric position, while magnetism originates from the partially filled *d*-orbitals, $d^5$ ($Fe^{3+}$) or $d^4$ ($Mn^{3+}$), respectively. This means that ferroelectricity and magnetism can coexist in a single-phase when the atoms which are responsible for the electric dipole by being in an off-center position, are different from those that possess the magnetic moment. However, since the two order phenomena are associated with different ions, the resulting coupling between their dual order properties is rather weak. Typically, in *type-I* multiferroics ferroelectricity (FE) and magnetism occur at different temperature. The first one typically

appears at higher temperatures than ferromagnetism (FM), *e.g.* at $T_{FE}$ = 1100 K vs. $T_{FM}$ = 643 K in case of $BiFeO_3$.[171] Thus, one of the main challenges of current research is to combine magnetism and ferroelectricity with enhanced coupling especially at appropriate temperatures.[177,178]

In contrast to *type-I* multiferroics a strong coupling results in *type-II* multiferroics, where magnetism causes ferroelectricity. One of the first studied systems of this class is $TbMnO_3$ where a strong influence of the electric polarization by a magnetic field was shown. Further examples for this kind of multiferroics are $Ni_3V_2O_6$, $MnWO_4$, and $TaMn_2O_5$.

Since the number of single-phase multiferroics is rather low, alternative ways for obtaining multiferroics have been investigated. In this context composite magnetoelectric systems have attracted some interest. For example, various materials in thick-film geometry like $Pb(Zr_xTi_{1-x})O_3$, $Pb(Mg_{0.33}Nb_{0.67})O_3$-$PbTiO_3$ as ferroelectrics and $NiFe_2O_4$, $CoFe_2O_4$, or $TbDyFe_2$ as ferromagnets were studied. Furthermore, nanostructured composites combining perovskites like $BaTiO_3$, $PbTiO_3$ or $BiFeO_3$ with spinels such as $CoFe_2O_4$, $NiFe_2O_4$ or $\gamma$-$Fe_2O_3$ were investigated.[172]

Even though a lot of research, including both experimental and theoretical studies, has already been carried out, the field of multiferroics is still of superior interest. Particularly the search for novel materials is considered with each new system posing its own new challenge to explore the individual mechanisms responsible for the magnetoelectric effect. With respect to new multiferroics one focus is on composite materials. Thus, recent research concentrates on further composites of known magnets and ferroelectrics in form of multilayers and nanostructures.[171]

# 2 MOTIVATION

The structure replication method was shown to be a versatile method to synthesize mesoporous materials with ordered pore systems, large specific surface areas and high thermal stability, thus rendering them interesting for various fields of application, *e.g.* in catalysis, gas sensing, or electrochemical applications. In addition, this synthesis approach offers the opportunity to control the structural parameter on both the mesoscopic and the macroscopic scale by variation of the synthesis conditions. The adjustable structural parameters, including pore size, pore wall thickness, specific surface area, crystallite size, as well as particle size and particle morphology, have significant impact on the materials' properties. However, these structure-related properties and the structure relation between the matrix and the replica have to be investigated for each system individually.

Aim of this work is the investigation of these aspects for three distinct mesoporous systems: $Co_3O_4$, $CoFe_2O_4$ and $Al_2O_3$. These are interesting for gas sensing,[138-140] magnetic data storage application[84,148,179] and as catalyst support material.[158-160] For characterization of the nanostructure powder X-ray diffraction analysis, nitrogen physisorption, transmission- and scanning electron microscopy, energy-dispersive X-ray spectroscopy and magnetic measurements were carried out. Magnetic characterization was carried out in cooperation with Prof. Dr. Stefan G. Ebbinghaus, Martin-Luther-Universität Halle-Wittenberg, Halle.

The synthesis of mesoporous $Co_3O_4$ by nanocasting from mesoporous silica as a structure matrix has already been described in literature,[62,89] however no particular attention was dedicated so far to the evolution of $Co_3O_4$ particles inside the pores of the matrix. Therefore, detailed investigations on the structure relation between the matrix and the resultant replica were carried out, particularly with respect to their morphology and particle size. Recently it was shown that the particle size and the crystallinity of several mesoporous metal oxides, including $Co_3O_4$, can be controlled by variation of the synthesis conditions;[59] this impact on the crystallinity and the mesoscopic order was investigated in some detail. $Co_3O_4$ as an antiferromagnetic material in bulk-phase has been shown to exhibit a different magnetic behavior for the nanoscale material.[180,181] Therefore the nanostructure-related magnetic properties of ordered mesoporous $Co_3O_4$ were investigated in a detailed study particularly with respect to surface area and crystallinity.

The nanocasting approach was recently shown to be successful also for preparing ternary metal oxides, including $CoFe_2O_4$.[84] However the synthesis of ternary systems is not as straightforward as in case of binary metal oxides. Particularly the desired stoichiometry and prevention of phase separation frequently bear a challenge. Therefore one focus was drawn to the synthetic work followed by investigations of the nanostructure-related properties similar to the binary system, including the magnetic properties. Second focus of this system was the development of a synthesis approach for preparing a composite material of $CoFe_2O_4$/$BaTiO_3$ as a promising candidate with multiferroic properties, *i.e.* combining at least two ferroic ordering properties.

For mesoporous $Al_2O_3$ obtained by nanocasting, which requires a mesoporous carbon as structural mold, the considered structure relation between matrix and resultant replica was also investigated for a replication procedure from a carbon matrix. The synthesis of mesoporous $Al_2O_3$ by nanocasting has already been reported.[116] This synthesis involves a precipitation step previously to the oxide formation which was described as helpful for crystallization.[118] Therefore the role of this precipitation step and the impact on the resultant $Al_2O_3$ replica were systematically investigated. Additionally the influence of a varied synthesis approach on the final $Al_2O_3$ replica was studied.

# 3   EXPERIMENTAL

## 3.1   Synthesis of the Structure Matrices

### 3.1.1   Mesoporous Silica (SBA-15 and KIT-6)

The mesoporous silica phases SBA-15 and KIT-6 serving as structure matrices for the syntheses of mesoporous carbon and cobalt oxides (binary and ternary) were synthesized by a modification of literature procedures:[21,22] Pluronic P-123 triblock copolymer (8.0 g; Sigma-Aldrich) was dissolved in mixture of deionized water (240 mL) and hydrochloric acid (32 %; 24.6 mL) by stirring at 35 °C for 24 hours. In case of the KIT-6 synthesis $n$-butanol (9.9 mL) was added, followed by further stirring for one hour. After addition of tetraethyl orthosilicate (≥ 99.0 %; 17.0 mL; Merck) the mixture was stirred at 35 °C for another 24 hours. The resulting gel was transferred to a teflon-lined autoclave and kept for 24 hours at 80 °C and 140 °C, respectively. After the hydrothermal treatment the resulting solid product was filtered off and washed with deionized water. For the removal of P-123 block copolymer the dried product was calcined under air at 550 °C for 6 hours (heating rate 2.5 °C min$^{-1}$).

### 3.1.2   Mesoporous Carbon (CMK-3 and CMK-8)

The mesoporous CMK-3 and CMK-8 carbon materials, utilized as structure matrices for the synthesis of mesoporous aluminum oxide, were prepared according to a modification of a literature procedure:[22] In a typical synthesis 1 g of the respective silica (SBA-15 for CMK-3 and KIT-6 for CMK-8) was added to a solution of sucrose (1.25 g; Fluka) with sulfuric acid (3 %; 6 mL) and stirred at room temperature until a homogeneous suspension was obtained. For partial polymerization, the mixture was treated initially at 100 °C for 6 hours and at 160 °C for a further 6 hours. This procedure was repeated for a more sufficient pore filling with sucrose (0.8 g) in sulfuric acid (3 %; 6 mL) and followed by the same thermal treatment as before. The complete carbonization was accomplished by heating at 900 °C under nitrogen atmosphere for 4 hours (heating program: up to 300 °C with 10 °Cmin$^{-1}$, up to 360 °C with 1 °C min$^{-1}$ and up to 900 °C with 5 °C min$^{-1}$). To remove the silica matrix the

silica/carbon composite was etched with hydrofluoric acid (5 %) for 4 hours and then washed with ethanol; this procedure was repeated until the silica amount has been reduced to less than 5 % in the product verified by gravimetric analysis.

## 3.2 Synthesis of the Metal Oxide Replica

### 3.2.1 Mesoporous Cobalt Oxide ($Co_3O_4$)

Mesoporous cobalt oxide was obtained by structure replication of a silica matrix (SBA-15 or KIT-6, respectively), applying the incipient wetness technique with cobalt nitrate ($Co(NO_3)_2 \cdot 6H_2O$; Merck) as precursor. The pores of the respective silica matrix were infiltrated with a saturated aqueous cobalt nitrate solution (15 g $Co(NO_3)_2 \cdot 6H_2O$ in 10 mL deionized water); the amount of the precursor solution corresponded to the pore volume of the utilized structure matrix. For example, 0.98 mL of the saturated cobalt nitrate solution was added to 1 g of a silica material with a specific pore volume of 0.98 $cm^3 g^{-1}$. After drying at 60 °C, the sample was thermally treated under air at 300 °C for 2 hours (heating rate 2 °C $min^{-1}$) to convert the cobalt nitrate into cobalt oxide. The steps of impregnation, drying and oxide formation, denoted as a 'impregnation/oxide formation cycle' in the following, were repeated one or two times to obtain a more complete pore filling. Finally, the silica matrix was removed by repeated leaching with a sodium hydroxide solution (2 mol $L^{-1}$) at room temperature for 4 hours; the sample was finally washed with deionized water.

For the investigation of the growth by scanning electron microscopy (SEM), aliquots of the samples were taken after each cycle of impregnation/oxide formation, and the silica was removed by the same procedure as described above. For investigation of the crystallinity and temperature stability, the silica-free $Co_3O_4$ samples were post-synthetically thermally treated for another 2 hours at various temperatures (300 °C, 400 °C, 500 °C and 600 °C) with a heating rate of 5 °C $min^{-1}$. Further experiments on the influence of growth and crystallinity were carried out by variation of the synthesis conditions during the oxide formation employing a closed vessel instead of an open as generally used.

### 3.2.2 Mesoporous Cobalt Iron Oxide (CoFe$_2$O$_4$)

Mesoporous cobalt iron oxide was prepared by modification of a literature procedure:[84] The pores of a KIT-6 silica matrix were infiltrated by the incipient wetness technique with an aqueous solution of cobalt nitrate (Co(NO$_3$)$_2$•6H$_2$O; Merck) and iron nitrate (Fe(NO$_3$)$_3$•9H$_2$O; Sigma-Aldrich) as precursors in the molar ratio of 1:2; the amount of precursor solution corresponded to the pore volume of the silica matrix. For example, 1 g of the respective silica matrix with a specific pore volume of 1.2 cm$^3$g$^{-1}$ was impregnated with 1.2 mL of the precursor solution (4 g Co(NO$_3$)$_2$•6H$_2$O and 11 g Fe(NO$_3$)$_3$•9H$_2$O dissolved in 5 mL deionized water). After drying at 60 °C, the sample was thermally treated under air at 600 °C for 2 hours (heating rate 1 °C min$^{-1}$) to convert the nitrates into the oxide. This procedure was repeated three times for a more complete pore filling. To remove the silica matrix the silica/cobalt iron oxide composite material was leached with sodium hydroxide (2 mol L$^{-1}$) at room temperature for 4 hours; this was repeated twice. Finally the product was washed with deionized water.

### 3.2.3 CoFe$_2$O$_4$/BaTiO$_3$ Composite Material

For a composite material of cobalt iron oxide and barium titanium oxide, the pores of the above-described CoFe$_2$O$_4$ (see 3.2.2) were filled with a mixture of barium citrate and titanium isopropoxide (≥ 97 %, Sigma-Aldrich) in the molar ratio of barium to titanium 1:1. In a typical synthesis procedure 1.3 g CoFe$_2$O$_4$ was mixed with a barium citrate solution which was freshly prepared by dissolving citric acid (1.28 g) in deionized water (1.7 mL) and by addition of barium carbonate (0.66 g; Sigma-Aldrich). Then titanium isopropoxide (1 mL) dissolved in ethanol was added, followed by stirring at 80 °C for 2 hours. After drying at 50 °C, the sample was thermally treated at 650 °C for 5 hours (heating rate 1 °C min$^{-1}$).

### 3.2.4 Mesoporous Aluminum Oxide (Al$_2$O$_3$)

Mesoporous aluminum oxide was prepared by nanocasting applying the incipient wetness method with aluminum nitrate (Al(NO$_3$)$_3$•9H$_2$O; Fluka) as precursor, which was used both in the molten state and as a saturated solution (10 g Al(NO$_3$)$_3$•9H$_2$O in 20 mL THF). For the synthesis the pores of the carbon matrix (CMK-3 and CMK-8) were infiltrated with the precursor, while the amount of the aluminum nitrate melt or - solution corresponded to the

pore volume of the utilized carbon material. For example, 1 g of the utilized carbon matrix with a specific pore volume of 1.68 $cm^3g^{-1}$ was either mixed with 1.68 mL of the saturated solution of aluminum nitrate or in case of the melt impregnation with 2.6 g aluminum nitrate which was previously melted at 90 °C (considering a melt density of 1.53 g $mL^{-1}$ at 90 °C[182]). In case of the melt impregnation a thermal treatment at 90 °C for 24 hours was subsequently carried out to obtain a homogenous distribution of the precursor in the carbon pores; the sample prepared by impregnation with a solution was dried at 60 °C instead. For the following *in-situ* precipitation of aluminum hydroxide all samples were treated with a vapor of an aqueous ammonia solution (12.5 % $NH_4OH$) at 60 °C for 3 hours followed by gradual drying stepwise heating to 120 °C. In order to facilitate precipitation occurring homogeneously over the entire sample a large contact area between the impregnated samples with the ammonia vapor is prerequisite. Subsequent conversion of aluminum hydroxide into aluminum oxide was carried out at 700 °C under nitrogen atmosphere for one hour (heating rate 2 °C $min^{-1}$). Finally, the carbon matrix was removed by combustion under air at 450 °C for 48 hours (heating rate 1 °C $min^{-1}$).

For further investigation with respect to the crystallinity the temperature of the oxide formation (500, 700, and 900 °C) as well as the duration of the ammonia vapor exposure (1, 3, 7, 24, and 48 hours) was varied.

## 3.3   Characterization Methods

### 3.3.1   Powder X-ray Diffraction

Powder X-ray diffraction (P-XRD) was carried out on a Bruker AXS D8 Advance diffractometer with a secondary monochromator by using Cu-Kα radiation (40 kV, 40 mA). The step size for low-angle measurements ($2\theta < 5°$) was $2\theta = 0.0075°$; for measurements in the wide-angle region ($20° < 2\theta < 80°$) the step size was 0.02° with 3 s counting time per step in both cases. P-XRD was also performed on a PANanalytical X'Pert Pro diffractometer with an X´Celerator real-time multiple-strip detector using the same radiation (Cu-Kα with 40 kV, 40 mA). The counting time was 25 s for low-angle measurements and 20 s for wide-angle measurements with steps of $2\theta = 0.0167$. If it is not explicitly noted, the first mentioned diffractometer was

utilized for characterization. For preparation the powdery samples were gently ground, placed on a sample holder and the surface was smoothed with an object slide.

### 3.3.2   Nitrogen Physisorption

Nitrogen physisorption analysis was conducted at 77 K with a Quantachrome NOVA 4000e; prior to measurement the samples were degassed at 120 °C for 24 hours. The isotherms were measured in the range of relative pressure between 0.050 and 0.995 consisting of 33 points for the adsorption and 40 points for the desorption branch, respectively. Specific surface areas were calculated from the adsorption branch by the 5 point BET method for relative pressures between 0.05 and 0.30; total pore volumes were determined at a relative pressure of 0.99 and pore size evaluation was carried out by non-local density functional theory (NLDFT)-based analysis from the desorption branch. Within this thesis the following two data kernels were utilized: 'N$_2$ at 77 K on silica (cylindrical pore, NLDFT equilibrium model)' and 'N$_2$ at 77 K on carbon (slit pore, NLDFT equilibrium model)'. The kernel for silica materials were also applied to other oxide systems, when the data obtained from the adsorption branch yielded the same results as from the desorption branch. If this was not the case, the NLDFT method was prohibitive and the BJH analysis was applied for pore size evaluation instead. However, it needs to be considered that the BJH method is not accurate and frequently underestimates the pore diameters up to 25 %.[183] For analysis of the microporosity the *t*-method according to BROEKHOFF and DE BOER[184] was applied using the data from the adsorption branch in the relative pressure range between 0.20 and 0.50.

### 3.3.3   Scanning Electron Microscopy

Scanning electron micrographs (SEM) were recorded with a HREM EDX Leo Gemini 982 and a ZEISS NEON® 40 with CrossBeam®. For sample preparation 5 μL of 20 mg sample dispersed in 1 mL deionized water were placed either on a silicon wafer in case of the ZEISS NEON® apparatus or on a carbon foil for the HREM EDX Leo Gemini 982 electron microscope, both adhered to the sample holder, and dried. If it is not explicitly noted, the first mentioned electron microscope was utilized for characterization.

### 3.3.4   Transmission Electron Microscopy

Transmission electron microscopy (TEM) and selected area electron diffraction (SAED) were performed on a Philips CM30-ST microscope; for energy-dispersive X-ray (EDX) analysis an EDAX PV 9900 was used. For preparation the powdery samples were directly placed on a copper grid.

### 3.3.5   Magnetic Measurements

Magnetic measurements were carried out on a Quantum Design PPMS 9. The field-dependent magnetization was measured with a magnetic field cycling between - 90 and + 90 kOe. For the temperature-dependent magnetization the samples were initially cooled to 10 K under a zero field before the magnetization was measured in the range from 10 K to 150 K at an applied field of 500 Oe.

# 4 RESULTS AND DISCUSSION

## 4.1 Structure Matrices

### 4.1.1 Structural Characterization of Mesoporous Silica (SBA-15 and KIT-6)

Mesoporous silica phases, SBA-15 with a hexagonal ordered pore system (*p6mm*) and KIT-6 silica with a cubic ordered pore system ($Ia\overline{3}d$), were synthesized by structure-directed sol-gel syntheses (see 3.1.1).[21,22] The thus-obtained silica materials serve as structure matrices for syntheses of mesoporous metal oxide and carbon replicas.

Figure 8 shows representative low-angle diffraction patterns of SBA-15 silica (left) as well as KIT-6 silica (right), both synthesized at 80 °C and 140 °C, respectively.
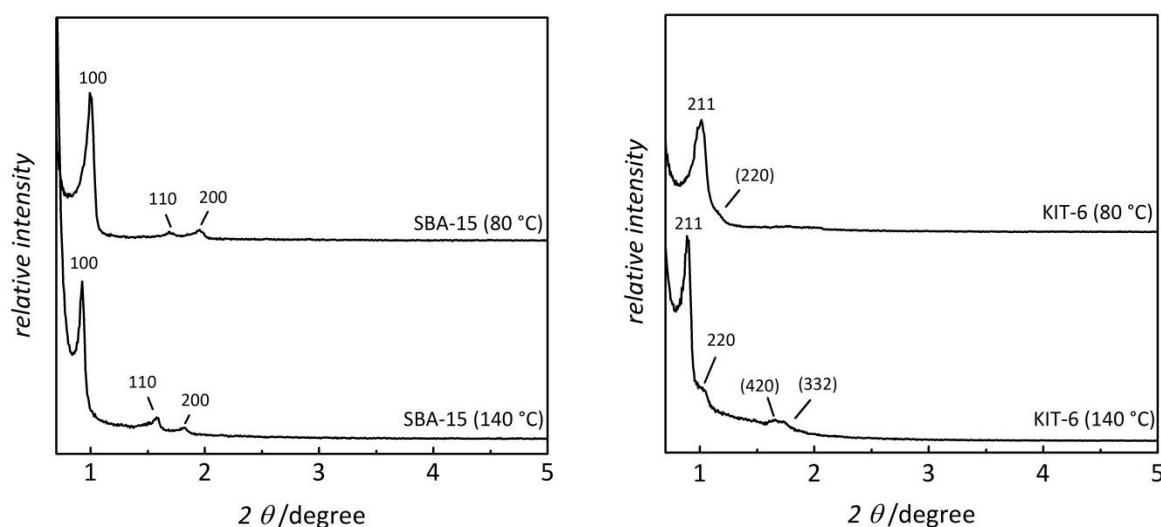


**Figure 8.** Low-angle X-ray diffraction patterns of hexagonal SBA-15 (left) and cubic KIT-6 silica (right), both synthesized at 80 °C and 140 °C. For reasons of clarity the diffractograms are vertically shifted.

The diffraction patterns of the SBA-15 silica (left) exhibit three well-resolved peaks for both samples which indicates a high structural order; the peaks can be indexed to 100, 110 and 200 associated with the hexagonal *p6mm* pore system symmetry. However, the *d*-values determined for the two silica samples are slightly different from each other; the value of SBA-15 synthesized at 140 °C is larger (*ca.* 1 nm) than that of SBA-15 synthesized at 80 °C (see Table 3). Similar findings are observed for the respective KIT-6 analogues synthesized at different temperatures. Both diffraction patterns (right) exhibit distinct peaks, where the

most intense peak can be indexed to 211, the less pronounced ones to 220, 420 and 332 according to a cubic $Ia\overline{3}d$ pore system symmetry.

Comparing the low-angle XRD patterns of both silica phases synthesized at 80 °C and 140 °C significant differences in the relative intensities between the first intensive diffraction peak and the other reflections at higher $2\theta$ values are observed. The more pronounced relative intensities of the reflections for the silica samples synthesized at 140 °C can be attributed to thinner pore walls, as already described for MCM-silica materials. [185,186]

The structural order of both silica phases is further confirmed by transmission electron microscopy (TEM). Figure 9 shows two representative images of SBA-15 (left) and KIT-6 silica (right), both synthesized at 80 °C. Pores and pore walls can be distinguished due to different densities; dark regions correspond to the pore wall, the bright ones to the pores. Both images reveal a well-ordered pore system over large distances; this is consistent with the results from the low-angle XRD patterns (see Figure 8).
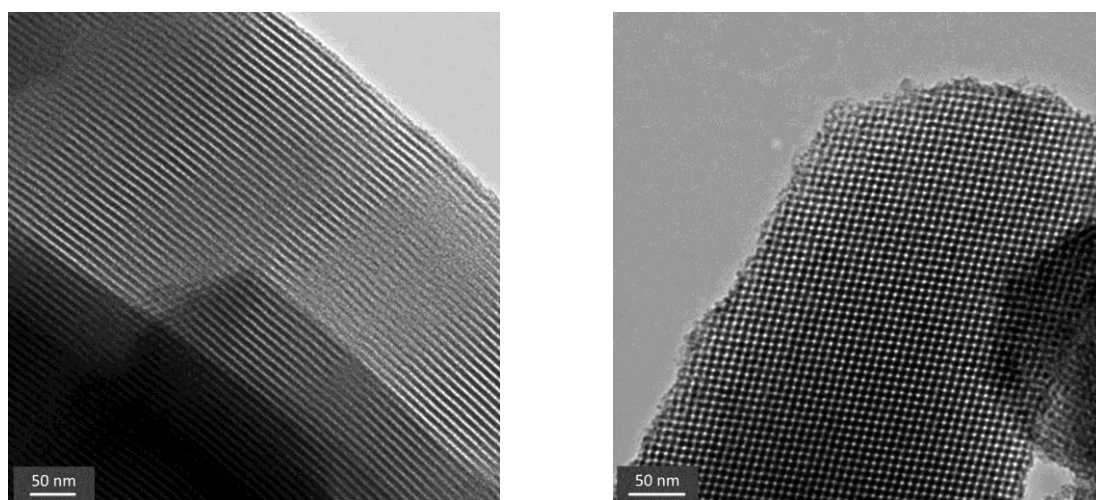


**Figure 9.** Representative TEM images of hexagonal SBA-15 (left) and cubic KIT-6 silica (right), both synthesized at 80 °C.

For characterization of the porosity nitrogen physisorption measurements were carried out. Figure 10 shows the respective isotherms of the above-described samples. All silica materials (SBA-15 and KIT-6, both hydrothermal treated at 80 °C and 140 °C) exhibit type IV isotherms with a pronounced H1-type hysteresis loop, indicating the presence of uniform cylindrical mesopores. Capillary condensation occurs for both types of silica materials (SBA-15 and KIT-6) at a relative pressure ($p/p_0$) of *ca.* 0.7 for the samples which were hydrothermal treated at 80 °C. With increasing synthesis temperature to 140 °C, the step of capillary

condensation is shifted to a higher relative pressure of about 0.8, associated with larger pores.
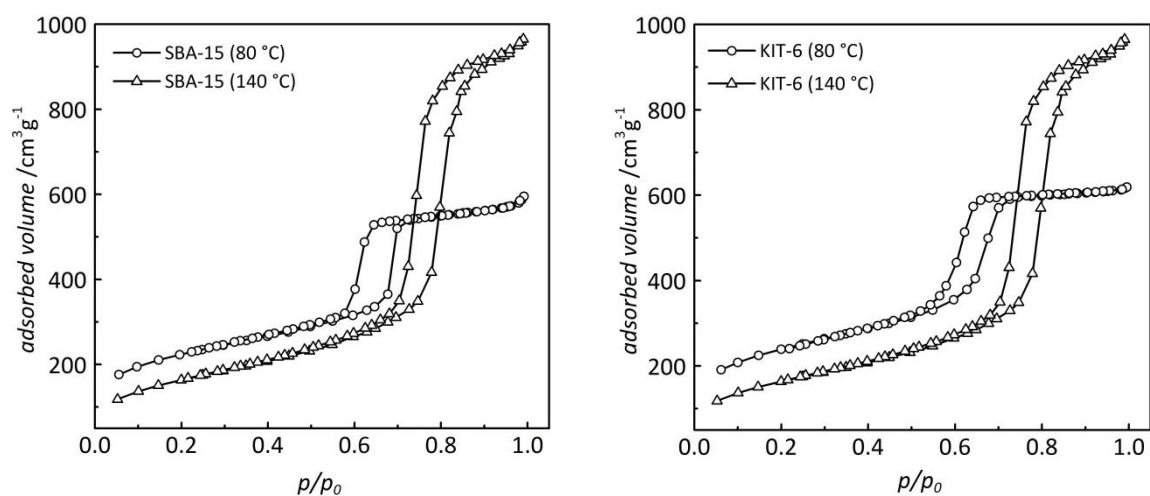


**Figure 10.** Nitrogen physisorption isotherms of hexagonal SBA-15 silica (left) and cubic KIT-6 silica (right), synthesized at 80 ° C and 140 °C, respectively.

The widths of the hystereses are smaller for both KIT-6 silica samples and for SBA-15 with the higher synthesis temperature compared to SBA-15 with an aging temperature of 80 °C. This is in good agreement with experimental data obtained by KLEITZ et al. which reveal that the hysteresis in an interconnected pore system (KIT-6) is smaller compared to those in a pore system with more independent mesopores (SBA-15).[187] With higher temperatures of the hydrothermal treatment, the independent mesopore system in SBA-15 aged at a low temperature changes to a 3-D mesoporous network, so that in case of the higher synthesis temperature the hysteresis for both silica phases (SBA-15 and KIT-6) exhibit an identical behavior.[187]

The corresponding pore size distributions obtained by NLDFT data-based evaluation, depicted in Figure 11, show the mentioned shift of the pore sizes with increasing synthesis temperature for both silica phases, SBA-15 (left) and KIT-6 (right). All four samples show narrow distributions with the maximum at 7.0 nm for both silica materials synthesized at 80 °C and at 9.8 nm for a synthesis temperature of 140 °C, which is in good agreement with results from ZHAO et al.[20,21] Slight differences in the peak width of the pore size distribution between the materials synthesized at low and high temperature are observed. In case of the higher synthesis temperature a broader distribution is obtained, which is attributed to the presence of complementary mesopores interconnecting adjacent channels through the silica wall already described by FUERTES.[188]
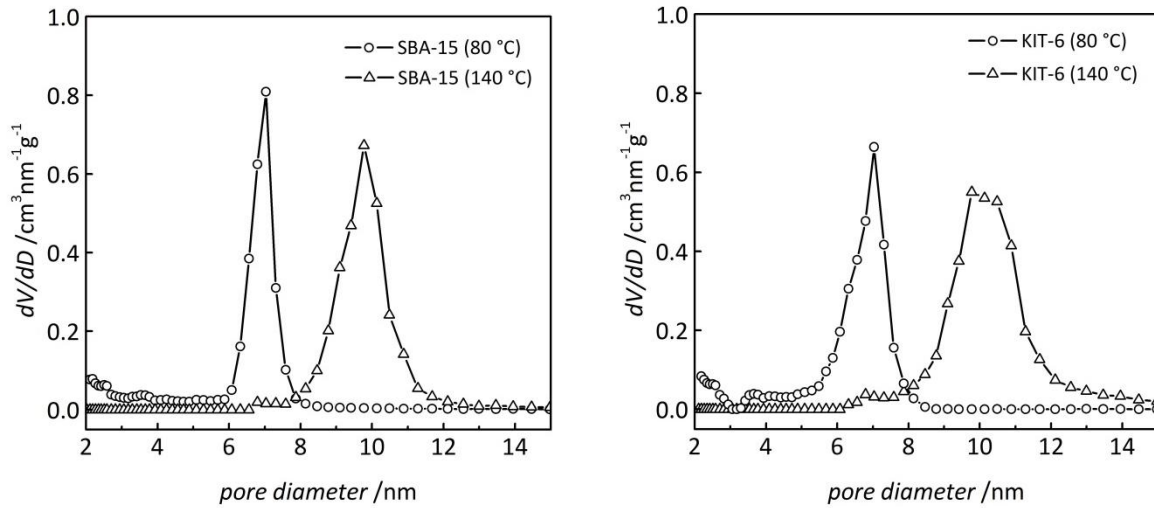
**Figure 11.** Pore size distributions (by using NLDFT data-based evaluation) of the same samples as in Figure 10.

The pore wall thickness is determined by combining the pore diameter with the lattice constant according to equation (1) for the hexagonal pore system, while equation (2) is applied in case of the cubic KIT-6 silica. The respective lattice constants *a* required for this calculation are obtained by equation (3) for the hexagonal and by equation (4) for the cubic system, respectively.[89]

$$h_{hex} = a - D \qquad (1) \qquad\qquad h_{cub} = \frac{a}{2} - D \qquad (2)$$

$$a_{hex} = \frac{2 \cdot d_{100}}{\sqrt{3}} \qquad (3) \qquad\qquad a_{cub} = d_{211} \cdot \sqrt{6} \qquad (4)$$

| | | |
|---|---|---|
| $h$ | = | pore wall thickness |
| $D$ | = | pore diameter |
| $a$ | = | lattice constant |
| $d$ | = | *d*-value |

By applying these equations the pore wall thicknesses are determined to 3.2 nm and 3.6 nm for SBA-15 and KIT-6, synthesized at 80 °C, which are thicker than those of the silica samples synthesized at 140 °C determined to 1.3 nm (SBA-15) and 2.4 nm (KIT-6). To conclude, the pore wall thickness decreases with higher synthesis temperatures whereas the pore size increases (see Table 3). This is in good agreement with the results obtained from low-angle diffraction patterns (see Figure 8), already indicating this decrease in wall thickness by the different relative intensities of the reflections.

By comparing the specific BET surface areas of the silica samples, significant differences between the samples, synthesized at 80 °C and 140 °C, are observed. The silica materials synthesized at 80 °C possess larger specific surface areas (*ca.* 800 m$^2$g$^{-1}$) than the materials synthesized at 140 °C (*ca.* 500 m$^2$g$^{-1}$); the individual BET surface areas for the respective silica samples are listed in Table 3. The differences can particularly be attributed to the higher fraction of microporosity present in the samples synthesized at a lower temperature; these micropores connecting adjacent mesopores are widened to mesopores by increasing the temperature which causes the lower specific surface area (see below).[186-191]
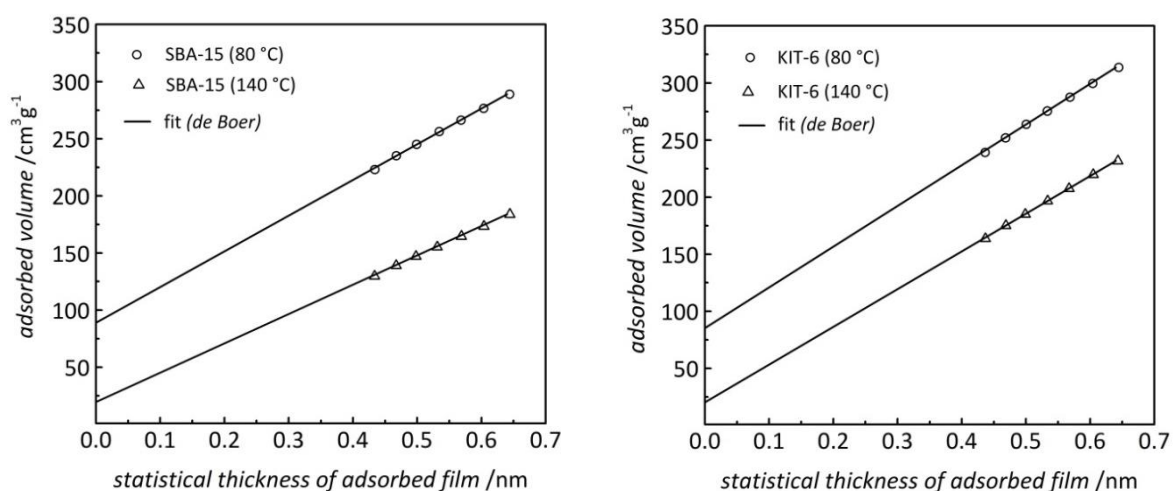


**Figure 12.** *t*-plot according to BROEKHOFF and DE BOER of the same samples as in Figure 10.

The different amount of micropores in the silica materials as a result of the synthesis temperature was further analyzed by the *V-t*-method according to BROEKHOFF and DE BOER;[184] the corresponding *t*-plots are depicted in Figure 12. For all silica samples linear fit results in a positive intercept, indicating the presence of micropores; this intercept is larger the higher the degree of microporosity is. In case of absent microporosity the *t*-method would yield the same results for determination of the specific surface area as the BET method and the linear curve fit (*t*-plot) could be extrapolated to the origin.[184] Comparing the *t*-plots of the four silica materials shows that the intercepts are shifted to larger values for the small-pore silica samples (with a synthesis temperature of 80 °C), suggesting a higher degree of microporosity. This is in accordance with results from GALARNEAU et al.[186] The contributions of the microporosity to the specific surface area and pore volume are included in Table 3.

The shape of the respective adsorption isotherms (see Figure 10) in the low *p/p₀* range also indicates the presence of micropores for the small-pore silica samples (synthesized at 80 °C),

which results in a steeper and stronger increase of the said isotherms in comparison to the large-pore silica materials (synthesized at 140 °C). This causes the additional small peak at *ca.* 2 nm as obtained in the corresponding pore size distribution (see Figure 11) for the silica samples synthesized at 80 °C.

The enlargement of the pore size as a result of an increased synthesis temperature is attributed to protonation and temperature-dependent hydrophilicity of the poly(ethylene oxide)block units (PEO) of the utilized triblock copolymer.[20] Under acidic conditions the more hydrophilic PEO blocks are stronger associated with the inorganic wall than the poly(propylene oxide)blocks (PPO). With increasing temperature the hydrophilic PEO segments become more hydrophobic, so that the volume of hydrophobic domains is increased while the lengths of PEO chains, which are associated to the silica wall, decreases. The increased volume of the hydrophobic domains (micelles) causes a decreased distance of adjacent micelles which goes along smaller pore walls. This enables a stronger intermicellar attraction from (PEO)-(PEO) interactions between adjacent micelles. As a result an increased pore size and a widening of the pores connecting two adjacent mesopores are obtained after removal of the triblock copolymer; the latter causes a better pore interconnectivity.[20,21,186,190] This has turned out to be a prerequisite for the following structure replication procedure by using silica phases as structural molds (see 4.2.2). The relation between synthesis temperature, pore size, pore wall thickness and pore interconnectivity is depicted in a simplified way in Scheme 1.
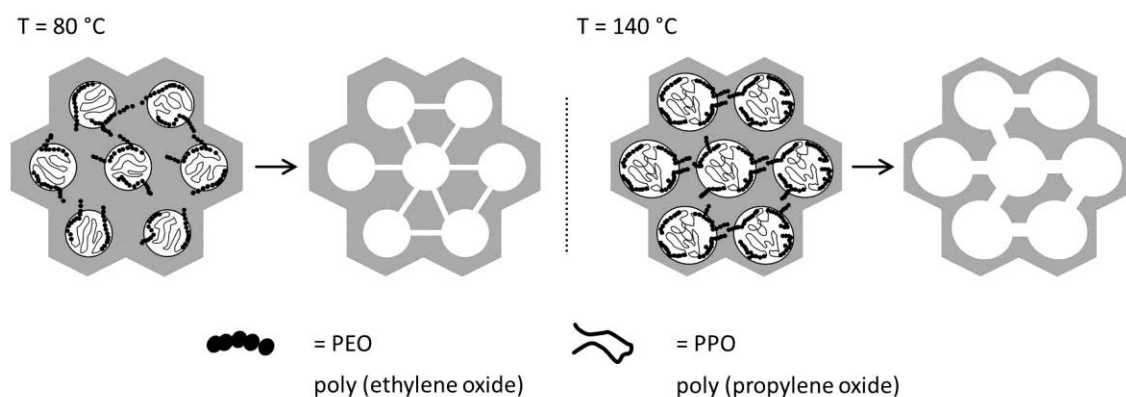


**Scheme 1.** Simplified schematic drawing of the relation between synthesis temperatures, pore size and interconnectivity of the silica materials (exemplified for the hexagonal pore system symmetry).

To summarize, ordered mesoporous silica materials were obtained with different pore system symmetries by a structure-directing synthesis process. Both silica phases, SBA-15 with a hexagonal ordered pore system as well as the cubic ordered KIT-6 silica, were synthesized with different pore sizes by varying the temperature for the hydrothermal treatment; the higher synthesis temperature also results in improved pore interconnectivity. Additionally, further structural parameters like pore wall thickness, specific BET surface area and pore volume were adjusted by variation of the synthesis temperature.

All structural data obtained from powder X-ray diffraction analysis and $N_2$ physisorption measurements of the hexagonal SBA-15 and the cubic KIT-6 silica synthesized at different temperatures for the hydrothermal treatment are listed in Table 3.

**Table 3.** Structural parameters from P-XRD and $N_2$ physisorption of SBA-15 and KIT-6 silica synthesized at 80 °C and 140 °C, respectively.

|  | $d$ [a] / nm | average pore diameter [b] / nm | average pore wall thickness / nm | specific BET surface area / $m^2g^{-1}$ | specific pore volume / $cm^3g^{-1}$ |
|---|---|---|---|---|---|
| SBA-15 (80°C) | 8.9 | 7.0 | 3.2 | 750 268 [c] | 0.91 0.14 [c] |
| SBA-15 (140°C) | 9.6 | 9.8 | 1.3 | 460 66 [c] | 1.16 0.03 [c] |
| KIT-6 (80°C) | 8.6 | 7.0 | 3.6 | 800 255 [c] | 0.95 0.13 [c] |
| KIT-6 (140 °C) | 10.0 | 9.8 | 2.4 | 580 70 [c] | 1.48 0.03 [c] |

[a] $d_{100}$ in case of the hexagonal SBA-15 silica; $d_{211}$ in case of the cubic KIT-6 silica; [b] average pore diameter was determined by NLDFT data-based evaluation; [c] micropore area and micropore volume determined by $t$-plot method according to BROEKHOFF and DE BOER

## 4.1.2 Structural Characterization of Mesoporous Carbon (CMK-3 and CMK-8)

Mesoporous carbon phases CMK-3 and CMK-8 were synthesized by a structure replication procedure from SBA-15 and KIT-6 silica, respectively (see 3.1.2).[22,192] The obtained carbon replica materials were employed as structure matrices for the synthesis of mesoporous aluminum oxide with both hexagonal (CMK-3) and cubic pore system symmetries (CMK-8).

Figure 13 shows the low-angle X-ray diffraction patterns of two mesoporous carbon materials obtained by structure replication from SBA-15 (CMK-3; left) and KIT-6 silica (CMK-8; right) compared to their structural molds. For both carbon materials the XRD patterns exhibit one pronounced peak. Further reflections at higher $2\theta$ values, as observed for the silica matrices, are not obtained for the replica materials. Another difference is the intensity of the reflections which is lower for the replica materials than that of their structural molds. This reduced intensity and the absence of additional peaks indicate a lower degree of mesoscopic order compared to their parental structure matrices; this is frequently observed in structure-replication procedures, as will be considered in the following sections (see 4.4.1).
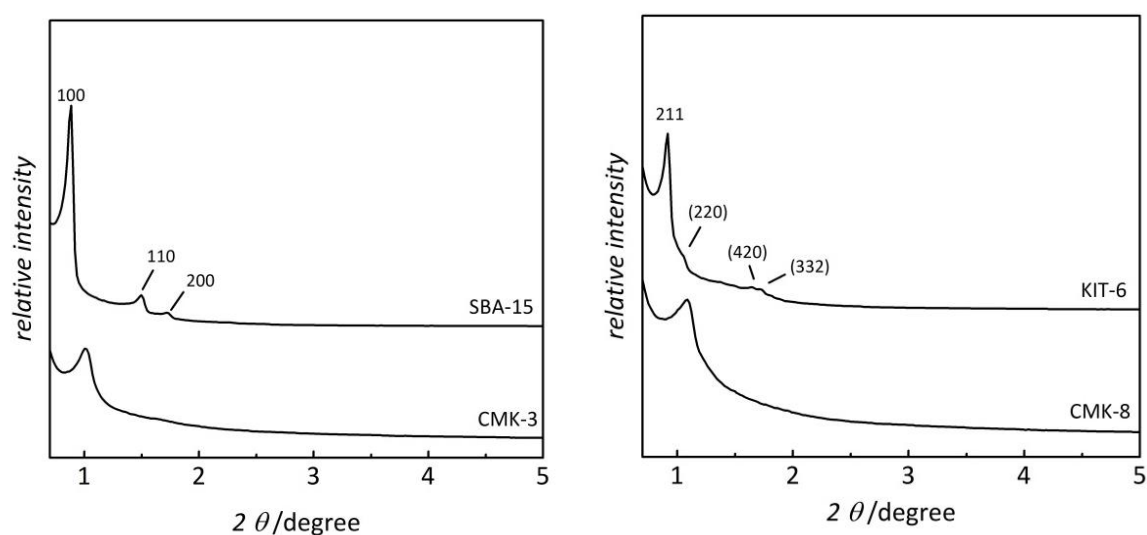


**Figure 13.** Low-angle X-ray diffraction patterns of mesoporous CMK-3 replicated from hexagonal SBA-15 silica (left) and mesoporous CMK-8 replicated from cubic KIT-6 silica (right) compared to the respective structure matrices. For reasons of clarity the diffractograms are vertically shifted.

The mesoscopic order was further analyzed by transmission electron microscopy. Figure 14 shows representative TEM images of the mesoporous CMK-3 (left) and CMK-8 (right) carbon materials, confirming the presence of long-range ordered regions.

Comparing the lattice plane distances (see Table 4) of the replica materials with those of their structure matrices ($d_{100}$ for the hexagonal, $d_{211}$ for the cubic system) reveals a decrease of the $d$-values for the carbon samples (8.8 and 8.2 nm) compared to those of the silica matrices (10.0 and 9.6 nm). This finding can be attributed to a structural shrinkage during the synthesis as a result of the high temperature required for the carbonization process as it was already reported by Jun et al.[192]
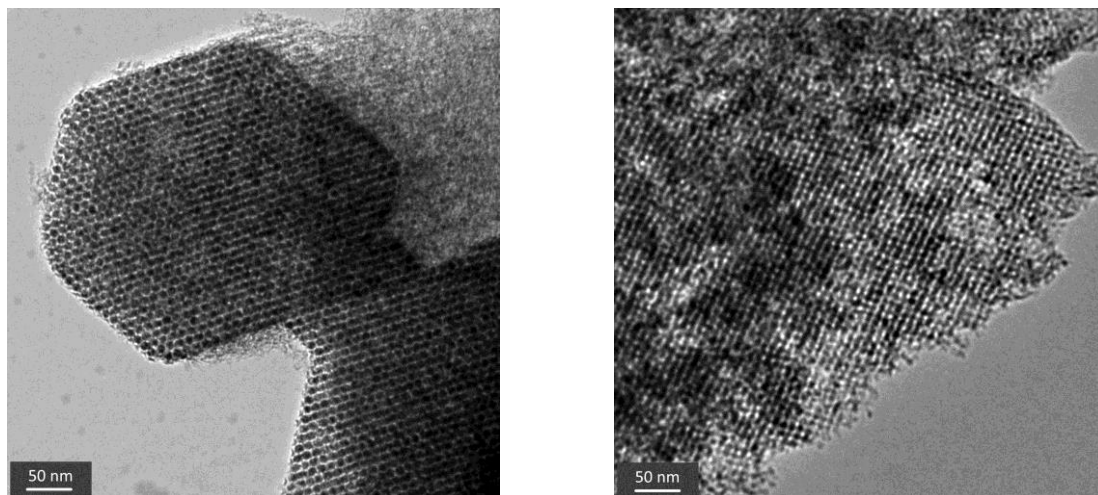
**Figure 14.** Representative TEM images of mesoporous carbon materials with hexagonal ordered pore system symmetry (CMK-3; left) and cubic (CMK-8; right).

Figure 15 shows the $N_2$ physisorption isotherms of both structure matrices and the resultant mesoporous CMK-3 (left) and CMK-8 carbon (right). The isotherms of the replicas show a type-IV behavior with pronounced hystereses (H1/H2) indicating the presence of regular mesopores with contribution of slit-like pores as expected for these replicas. The capillary condensation occurs for both carbon materials at a relative pressure $p/p_0$ of *ca.* 0.5.
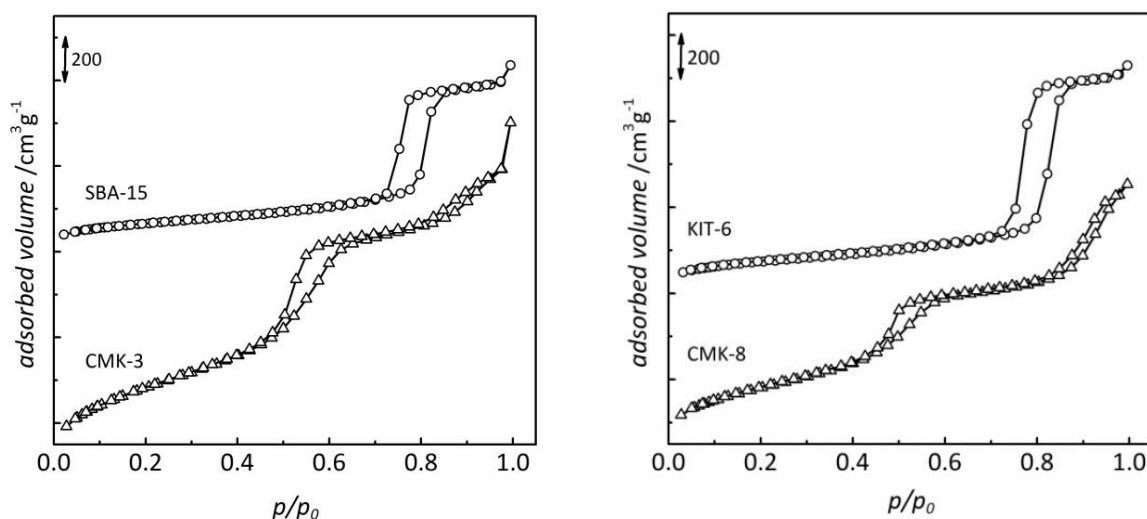


**Figure 15.** Nitrogen physisorption isotherms of hexagonal CMK-3 (left) and cubic CMK-8 carbon (right) compared to the utilized structure matrices. For reasons of clarity the isotherms are vertically shifted.

The corresponding pore size distributions obtained by NLDFT data-based evaluation (see Figure 16) exhibit a narrow peak with their maximum at 4.2 nm and 4.0 nm, for CMK-3 and CMK-8, respectively. Additionally, in both cases a small shoulder around 3 nm is observed, which might be caused by secondary mesoporosity, also observed by JUN et al.[192] The pore

wall thicknesses, *i.e.* the diameter of the carbon rods, were determined to about 6 nm for both samples, which is thinner than the pore diameter of the utilized structure matrix (*ca.* 11 nm). This can be explained by the already-mentioned shrinkage during the synthesis and, especially by an incomplete pore filling of the silica matrices with carbon.

Analysis of the isotherms by the BET method yields specific surface areas of about 1500 $m^2g^{-1}$ and total pore volumes of about 1.8 $cm^3g^{-1}$, both with minor contribution of microporosity and/or secondary mesoporosity. The presence of micropores becomes obvious by the shape of the respective adsorption isotherms in the low $p/p_0$ range (see 4.1.1); the contributions of the microporosity to the specific BET surface area and the pore volume are included in Table 4. This fraction of micropores is larger than that of the respective silica matrices, and consequently explains the significantly higher specific surface areas compared to that of their structural molds (*ca.* 500 $m^2g^{-1}$ with *ca.* 100 $m^2g^{-1}$ contribution of micropores). When interpreting BET values it also needs to be taken into account that the density of the materials is slightly different ($\rho_{silica}$= 2.2 g $cm^{-3}$ vs. $\rho_{carbon}$ = 2.1 g $cm^{-3}$).[193]

The amount of residual silica was gravimetrically determined to *ca.* 1 % for CMK-3 and to *ca.* 0.3 % for the CMK-8 sample, respectively.
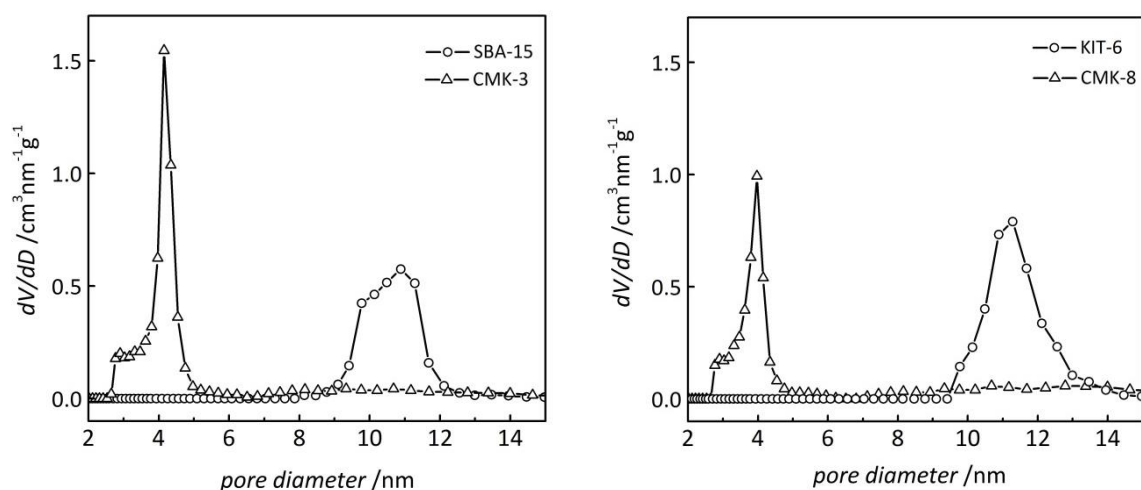


**Figure 16.** Pore size distributions determined by NLDFT data-based evaluation of hexagonal CMK-3 (left) and cubic CMK-8 carbon (right) compared to their structure matrices.

In summary, mesoporous carbon materials with different pore system symmetries were obtained by structure replication from mesoporous SBA-15 and KIT-6 with hexagonal and cubic ordered pore system, respectively. Both carbon phases, CMK-3 and CMK-8, possess well-ordered pore systems over large distances and large specific surface areas.

All structural data for the CMK-3 and CMK-8 carbon materials as well as those of the utilized structure matrices, obtained from powder X-ray diffraction analysis and from the $N_2$ physisorption measurements, are summarized in Table 4.

**Table 4.** Structural parameters from P-XRD and $N_2$ physisorption of CMK-3 and CMK-8 carbon compared to the respective structure matrix.

| | $d^{[a]}$ / nm | average pore diameter [b] / nm | average pore wall thickness / nm | specific BET surface area / $m^2g^{-1}$ | specific pore volume / $cm^3g^{-1}$ |
|---|---|---|---|---|---|
| (SBA-15) | 10.0 | 10.9 | 0.7 | 466 (78) [c] | 1.23 (0.04) [c] |
| CMK-3 | 8.8 | 4.2 | 6.0 | 1655 (288) [c] | 1.86 (0.14) [c] |
| (KIT-6) | 9.6 | 11.3 | 0.5 | 516 (107) [c] | 1.57 (0.05) [c] |
| CMK-8 | 8.2 | 4.0 | 6.1 | 1382 (293) [c] | 1.74 (0.15) [c] |

[a] $d_{100}$ in case of the hexagonal CMK-3 carbon; $d_{211}$ in case of the cubic CMK-8 carbon
[b] pore width was determined by NLDFT data-based evaluation; [c] micropore area and micropore volume determined by $t$-plot method according to BROEKHOFF and DE BOER

## 4.2  Mesoporous Cobalt Oxide

### 4.2.1  Structural Characterization of Mesoporous Cobalt Oxide

Mesoporous cobalt oxide ($Co_3O_4$) was synthesized by nanocasting (see 3.2.1) with SBA-15 and KIT-6 silica, each with small (synthesis at 80 °C) and large pores (synthesis at 140 °C), as structure matrices. Thus, for the replication procedure structure matrices with different pore system symmetries as well as varied pore sizes and pore wall thicknesses were applied. In the following, the cobalt oxide samples are termed '$Co_3O_4$ (respective structure matrix with its synthesis temperature)'; for example '$Co_3O_4$ (SBA-15 80 °C)' means that SBA-15 with a synthesis temperature of 80 °C was utilized as the structure matrix.

### 4.2.1.1   $Co_3O_4$ from Mesoporous SBA-15 Silica

Figure 17 shows the results of powder X-ray diffraction for the $Co_3O_4$ replicas obtained after three cycles of impregnation and subsequent oxide formation by using SBA-15 with different pore sizes as structure matrix.
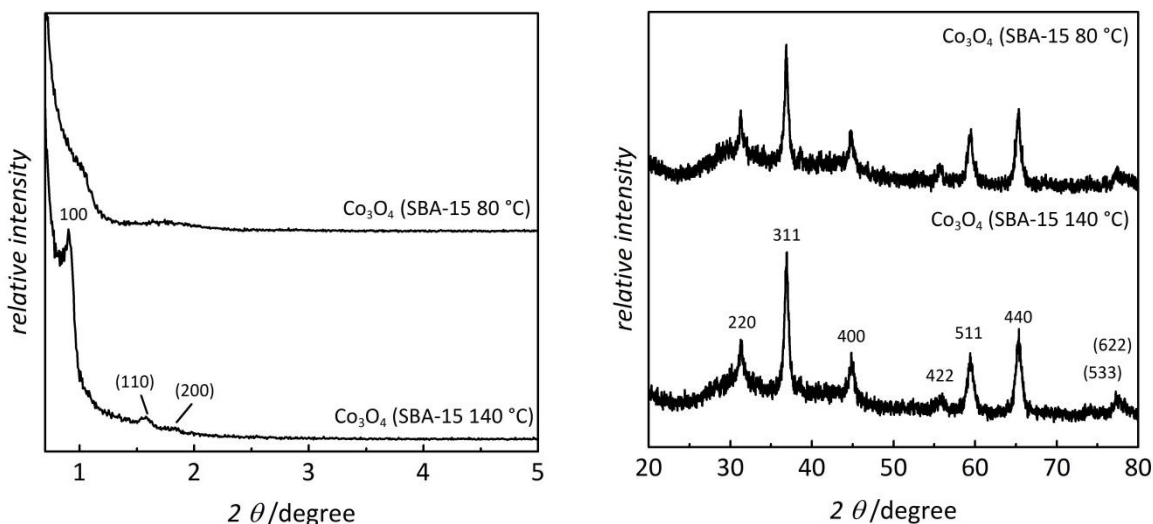


**Figure 17.** Low- and wide-angle X-ray diffraction patterns of $Co_3O_4$ obtained by nanocasting from SBA-15, which was synthesized at 80 °C and 140 °C, respectively. For reasons of clarity the diffractograms are vertically shifted.

The low-angle diffraction patterns (left) exhibit three peaks indicating long-range order for the replica of SBA-15 with a synthesis temperature of 140 °C. The peaks can be indexed to 100, 110 and 200 according to the hexagonal *p6mm* pore system symmetry of the utilized silica structure matrix. In contrast, the diffraction pattern of $Co_3O_4$ replicated from small-pore SBA-15 (synthesized at 80 °C) shows less well-resolved reflections; only weak shoulders are observed. This indicates a lower mesoscopic order compared to $Co_3O_4$ replicated from large-pore SBA-15 (synthesized at 140°C). The comparison of the low-angle X-ray diffraction patterns of the $Co_3O_4$ replica materials with those of their parental SBA-15 structure matrices (see Figure 8, left) reveals that the former ones are less well-resolved than those of the respective structure matrices. This can be attributed to structural loss in mesoscopic order caused by the replication procedure. Nevertheless, the calculated *d*-value of the $Co_3O_4$ replica from SBA-15 (140 °C) is in good accordance with that of the utilized silica matrix (9.7 nm vs. 9.6 nm). A slight deviation is observed for the replica from SBA-15 synthesized at 80 °C, where the *d*-value was determined to 8.5 nm compared to 8.8 nm of the parental structure matrix (SBA-15 80°C). However, this deviation can be explained by considering that

the determination of 2 $\theta$ is more afflicted with uncertainties for the $Co_3O_4$ replica from small-pore SBA-15 due to the only weak shoulder of the 100 reflection. To conclude, the *d*-value of $Co_3O_4$ replicated from large-pore SBA-15 corresponds slightly better to that of the parental silica matrix than for replication from small-pore SBA-15 silica. These findings, implying a more successful structure replication in case of $Co_3O_4$ (SBA-15 140°C), can be explained by the already mentioned better pore interconnectivity of the SBA 15 with larger pores (see 4.1.1 ).

Figure 17 (right) shows the corresponding wide-angle diffraction patterns of the same samples, exhibiting the typical signature of the cubic spinel phase (JCPDS 09-0418) for both $Co_3O_4$ replicas. By applying the SCHERRER equation (5) to the 311 peak the crystallite sizes are determined to 19 and 16 nm for $Co_3O_4$ (SBA-15 80°C) and $Co_3O_4$ (SBA-15 140°C), respectively (see Table 5), which means that the crystalline domains extend over various repetition distances of the mesopores, as also observed for few other systems, *e.g.* $In_2O_3$.[94] However, it should be mentioned that for porous materials the reliability of the SCHERRER method has to be regarded as limited.

$$s_{cryst} = \frac{k \cdot \lambda}{FWHM \cdot cos\theta} \qquad (5)$$

$k$ = SCHERRER constant (0.94)

$\lambda$ = wavelength of X-ray tube (0.154 nm)

$FWHM$ = full width at half maximum

$\theta$ = diffraction angle

In addition to powder X-ray diffraction, transmission electron microscopy combined with electron diffraction was carried out for further characterization of the pore system and the crystallinity of the $Co_3O_4$ materials. Figure 18 shows representative TEM images of $Co_3O_4$ replicated from SBA-15 with a synthesis temperature of 80°C (left) and $Co_3O_4$ from SBA-15 synthesized at 140°C (right). Both materials exhibit an ordered porous nanostructure; however some small differences concerning their mesoscopic structures become apparent. The structure replication of SBA-15 (80 °C) yield a fibrous $Co_3O_4$ material, but yet connected, whereas no fibers are obtained for $Co_3O_4$ (SBA-15 140 °C). The latter consists of more defined (connected) particles with larger ordered domains compared to the first mentioned

sample. This is in good agreement with the results of the low-angle XRD pattern (see Figure 17, left) and can again be explained by the different pore interconnectivity of the utilized structure matrix (see 4.1.1). Thus, the mesoscopic structure of the replica can be adjusted from nanowire shaped to a nanostructured network of $Co_3O_4$, also observed by RUMPLECKER et al.[89] The insets in Figure 18 show the corresponding selected area electron diffraction (SAED) patterns of both $Co_3O_4$ samples; distinct spots indicate crystalline domains in the pore wall, which is in conformity with the results obtained from the wide-angle XRD pattern (Figure 17, right). Energy-dispersive X-ray diffraction (EDX) analyses at a minimum of 5 spots for each sample reveal a silica amount of less than 2 % for both samples.
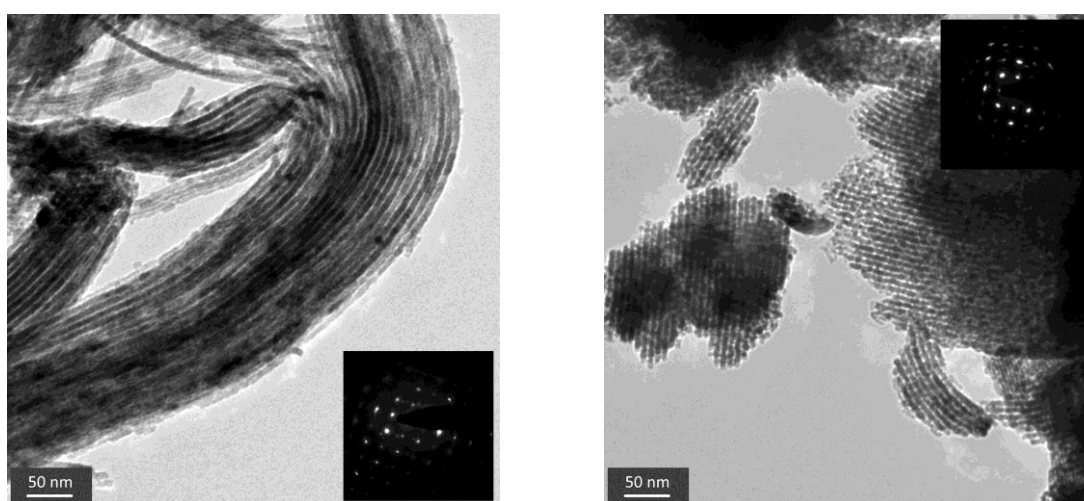


**Figure 18.** Representative TEM images of $Co_3O_4$ obtained by nanocasting from SBA-15, synthesized at 80 °C (left) and 140 °C (right), respectively. Insets show the corresponding SAED patterns.

For analyzing the porosity nitrogen physisorption isotherms were measured. Figure 19 (left) displays the isotherms of the two $Co_3O_4$ replicas with hexagonal pore system symmetry. In both cases the isotherms show a type-IV behavior with a weak hysteresis for the replica from SBA-15 (140 °C), which is less pronounced for the replica from SBA-15 (80 °C). The capillary condensation occurs at a relative pressure of $p/p_0$ = 0.5 in case of $Co_3O_4$ (SBA-15 140 °C), whereas this step could not be clearly determined for $Co_3O_4$ (SBA-15 80°C).

However, the corresponding pore size distributions obtained by NLDFT data-based evaluation (Figure 19, right) reveal mesoporous materials with average pore diameters of 4.2 nm for the replica from SBA-15 (80 °C) and 5.6 nm for the $Co_3O_4$ replicated from SBA-15 (140 °C), respectively.
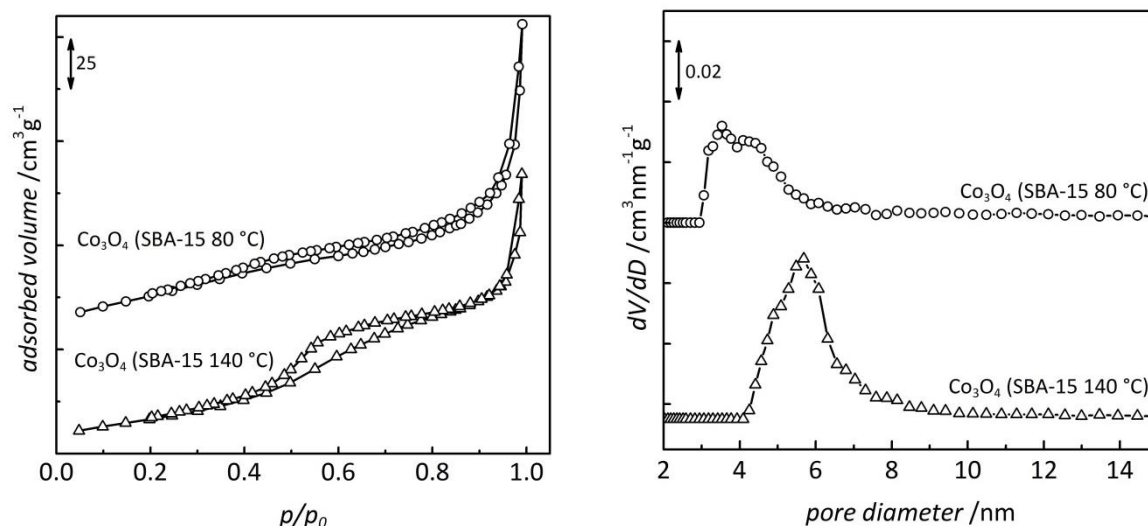
**Figure 19.** Nitrogen physisorption isotherms (left) and corresponding pore size distributions obtained by NLDFT data-based evaluation (right) of the same samples as in Figure 17. For reasons of clarity the isotherms and pore size distributions are vertically shifted.

The pore wall thicknesses were determined by equation (1) to 5.6 nm for both $Co_3O_4$ samples. Taking into account that small-pore SBA-15 silica has thicker pore walls than large-pore SBA-15, a structure replication from small-pore SBA-15 should result in $Co_3O_4$ replica of larger pores with thinner pore walls, whereas smaller pores with thicker pore walls would be expected for the replication from large-pore SBA-15. Contrary to this, here the pore wall thickness is the same for both materials and the pores are larger for the $Co_3O_4$ replica from large-pore SBA-15 than for the replica of small-pore SBA-15; hence, the opposite is the case. Since the $d$-values remain almost constant during the structure replication procedure these findings can be explained either by a volume shrinkage of the $Co_3O_4$ material in the pore during the oxide formation or by an incomplete pore filling of the silica pore with $Co_3O_4$ material, both resulting in thinner walls and larger pores, as observed for $Co_3O_4$ (SBA-15 140 °C). However, discrepancies between structural parameters of parental silica and the respective metal oxide replica are frequently observed in the structure replication process since the oxide formation procedure is typically associated with a densification.[194] For example, in case of the synthesis of $Co_3O_4$, the density of cobalt nitrate which is used as the precursor is substantially lower compared to that of the resultant $Co_3O_4$ after the oxide formation (2.49 g cm$^{-3}$ vs. 6.11 g cm$^{-3}$).[193]

By applying the BET model, significant differences in specific surface areas were obtained for the $Co_3O_4$ replicas from small- and large-pore SBA-15 (101 $m^2g^{-1}$ vs. 80 $m^2g^{-1}$). This difference is expected, since replication from smaller-pore structure matrices frequently results in higher specific surface areas than that from larger-pore matrices.[89] This can be explained by a higher porosity caused by thinner pore walls and a higher fraction of pores which are yielded by the replication from small-pore silica in comparison to the replica of large-pore silica. By comparing the specific surface areas of the replica with those of their parental structure matrices, it is conspicuous that the BET values are significantly smaller for the $Co_3O_4$ replicas (101 $m^2g^{-1}$ and 80 $m^2g^{-1}$) than those of the silica (750 $m^2g^{-1}$ and 460 $m^2g^{-1}$). This is attributable to several aspects. The first and probably the most relevant reason is the difference in the (bulk-) densities of amorphous silica ($\rho = 2.2$ g cm$^{-3}$)[186] and $Co_3O_4$ ($\rho = 6.11$ g cm$^{-3}$),[193] affecting the specific surface area. However, even when taking into account that the density of $Co_3O_4$ is nearly three times larger than that of silica, the specific surface areas of the replica materials are still lower in comparison to those of the silica. Another issue that should be considered is the crystallinity of $Co_3O_4$ associated with a lower surface roughness than for amorphous silica which will also contribute to a lower specific surface area. Furthermore, the already mentioned microporosity being present in SBA-15, especially for a synthesis temperature of 80 °C, causes a higher specific surface area, which is not the case for the replica material without microporosity. This was verified by the V-t method according to BROEKHOFF and DE BOER;[184] the contributions of micropores are listed in Table 5.

All structural parameters of the $Co_3O_4$ materials replicated from SBA-15 compared to those of the utilized structure matrices obtained from powder X-ray diffraction analysis and $N_2$ physisorption measurements are summarized in Table 5.

**Table 5.** Structural parameters from P-XRD and $N_2$ physisorption of $Co_3O_4$ obtained from SBA-15, synthesized at 80 °C and 140 °C, respectively.

| | $d_{100}$ / nm | average pore diameter [a] / nm | average pore wall thickness / nm | specific BET surface area / $m^2g^{-1}$ | specific pore volume / $cm^3g^{-1}$ | crystallite size [b] / nm |
|---|---|---|---|---|---|---|
| (SBA-15 80°C) | 8.8 | 7.0 | 3.2 | 750 (268) [c] | 0.91 (0.14) [c] | - |
| $Co_3O_4$ replica | 8.5 | 4.2 | 5.6 | 101 (-) [c] | 0.19 (-) [c] | 19 |
| (SBA-15 140°C) | 9.6 | 9.8 | 1.3 | 460 (66) [c] | 1.16 (0.03) [c] | - |
| $Co_3O_4$ replica | 9.7 | 5.6 | 5.6 | 80 (-) [c] | 0.17 (-)[c] | 16 |

[a] average pore diameter was determined by NLDFT data-based evaluation; [b] crystallite size was evaluated according to the SCHERRER equation; [c] micropore area and micropore volume determined by *t*-plot method according to BROEKHOFF and DE BOER

## 4.2.1.2  $Co_3O_4$ from Mesoporous KIT-6 Silica

In addition to the structure replication from hexagonal ordered SBA-15 silica, mesoporous $Co_3O_4$ samples with cubic pore system symmetry were synthesized. Figure 20 shows the powder X-ray diffraction patterns of the respective $Co_3O_4$ replicas after three cycles of impregnation and oxide formation with small- and large-pore KIT-6 silica as structure matrix. In both cases the intense 211 peak as well as weak reflections at higher 2 $\theta$ values are obtained, which can be indexed to 220, 420 and 332 associated to the cubic $Ia\bar{3}d$ symmetry of the respective KIT-6 silica. The *d*-values are determined to 8.5 nm and 10.0 nm for the $Co_3O_4$ replica from KIT-6 synthesized at 80 °C and 140 °C, respectively. By comparing these values with those of their parental silica matrices, it becomes obvious that the structure replication has occurred without significant change in the size of the unit cell as the *d*-values matches very well with those of the original silica (see Table 6). Only the intensities of the obtained diffraction patterns differ from those of their silica matrix, indicating a structural loss in mesoscopic order caused by the replication process, already observed for the above-described $Co_3O_4$ replicas from SBA-15.

The wide-angle X-ray diffraction patterns (right) exhibit the same signature as the replicas from SBA-15, indicating the presence of crystalline domains of spinel-type cobalt oxide ($Co_3O_4$; JCPDS 09-0418) with crystallite sizes of 13 nm and 15 nm for $Co_3O_4$ (KIT-6 80 °C) and $Co_3O_4$ (KIT-6 140°C), respectively (see Table 6). Thus, the sizes of the crystalline domains determined by the SCHERRER equation (5) to the 311 peak are comparable to those obtained for the $Co_3O_4$ samples with the hexagonal pore system (see Table 5).
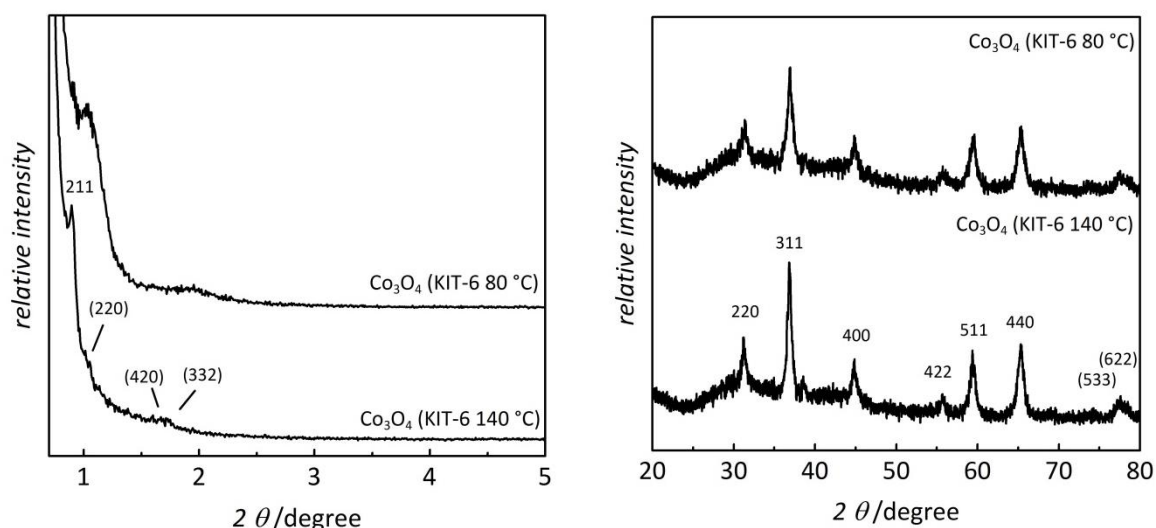


**Figure 20.** Low- and wide-angle X-ray diffraction patterns of $Co_3O_4$ obtained by nanocasting from KIT-6, synthesized at 80 °C and 140 °C, respectively. For reasons of clarity the diffractograms are vertically shifted.

The mesoscopic order is further confirmed by transmission electron microscopy. Figure 21 shows representative TEM images of the $Co_3O_4$ replicas from KIT-6 synthesized at 80 °C (left) and from KIT-6 with a synthesis temperature of 140 ° (right). Both samples possess a long-range ordered pore system, in case of $Co_3O_4$ (KIT-6 80 °C) the tortuosity of the pore system is visible. The insets show the corresponding SAED patterns of the same samples. Similar to hexagonal ordered $Co_3O_4$, distinct spots are obtained, indicating the presence of crystalline domains; this is in good accordance with the wide-angle diffraction pattern (Figure 20, right). Energy-dispersive X-ray diffraction (EDX) analyses at a minimum of 5 spots for each sample yield a silica amount of less than 2 % for both samples.
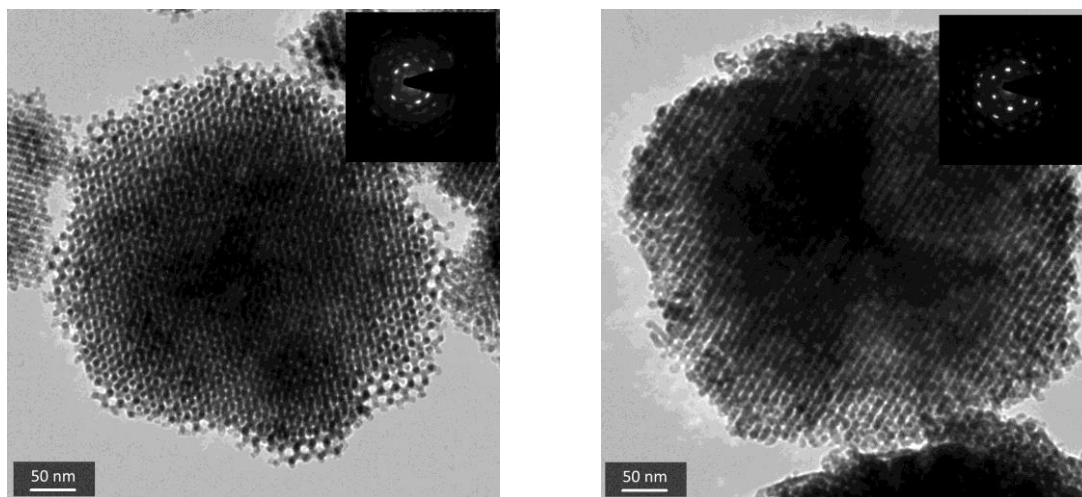
**Figure 21.** Representative TEM images of the same samples as in Figure 20. The insets show the corresponding SAED patterns.

Similar to the nitrogen physisorption measurements of the above-described hexagonal $Co_3O_4$ samples (see Figure 19), the isotherms depicted in Figure 22 (left) for the cubic analogues also show a type IV behavior with a weak hysteresis which is less pronounced for the $Co_3O_4$ replicated from small-pore KIT-6 silica. Capillary condensation occurs at a relative pressure of about $p/p_0$ = 0.5 in case of $Co_3O_4$ (KIT-6 140 °C) while determination of this step is more difficult to identify for $Co_3O_4$ (KIT-6 80 °C); this is similar to the results obtained for the hexagonal system.

The corresponding pore size distributions obtained by NLDFT data-based evaluation (Figure 22, right) show maxima at 4.6 nm and 5.5 nm for $Co_3O_4$ (KIT-6 80 °C) and $Co_3O_4$ (KIT-6 140 °C), respectively; the resulting wall thicknesses for these samples are determined to 5.9 nm and 6.7 nm by equation (4). Here again, by comparing the pore size of the utilized silica matrix with the pore wall thickness of the resulting replica, for both replicas a discrepancy is observed, which can be explained by an incomplete pore filling or a shrinkage (see Table 6). However, in this case, the KIT-6 silica with the smaller pore size (7.0 nm) yields the replica with the smaller walls (5.9 nm) compared to the KIT-6 with larger pores (9.8 nm) leading to a replica with thicker walls (6.7 nm). This was not the case for the hexagonal system, indicating that the replication is more successful for the cubic silica structure with the better interconnected pore system.
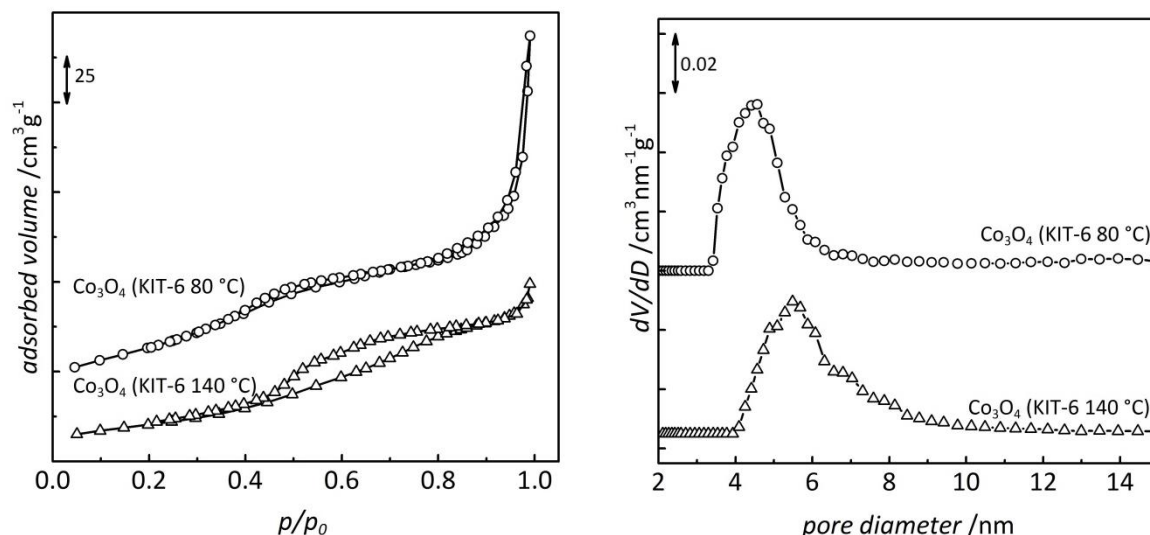
**Figure 22.** Nitrogen physisorption isotherms (left) and corresponding NLDFT-pore size distributions (right) of the same samples as in Figure 20. For reasons of clarity the isotherms and pore size distributions are vertically shifted.

The specific BET surface areas were calculated to 137 $m^2g^{-1}$ for the $Co_3O_4$ replica from KIT-6 synthesized at 80 °C and to 77 $m^2g^{-1}$ for the analogue from KIT-6 with the higher synthesis temperature of 140 °C. Thus again, both specific surface areas of the replica are substantially lower than those of their parental structure matrices, while the replica from the smaller-pore silica possesses the higher specific surface area; both findings are consistent with those already discussed above for the hexagonal pore system.

In summary, ordered mesoporous $Co_3O_4$ materials were successfully synthesized by structure replication utilizing silica matrices with different pore system symmetries as well as varied pore sizes. Hexagonal ordered SBA-15 and cubic KIT-6 silica with pore sizes of 7.0 nm and 9.8 nm were applied resulting in mesoporous ordered $Co_3O_4$ with varied structural parameter. It was observed that the pore interconnectivity has a substantial impact on the quality of the resulting replica, while replication of SBA-15 with low interconnectivity between the mesopores (by micropores) yield a replica with a lower structural order than $Co_3O_4$ replicas from a silica with a highly branched and more accessible pore channels being present in KIT-6.

All structural parameters of the $Co_3O_4$ materials replicated from KIT-6 and those of the respective structure matrices obtained from powder X-ray diffraction analysis and $N_2$ physisorption measurements are summarized in Table 6.

**Table 6.** Structural parameters from P-XRD and $N_2$ physisorption of $Co_3O_4$ obtained from KIT-6 synthesized at 80 °C and 140 °C, respectively.

| | $d_{211}$/ nm | average pore diameter [a] / nm | average pore wall thickness / nm | specific BET surface area / $m^2g^{-1}$ | specific pore volume / $cm^3g^{-1}$ | crystallite size [b] / nm |
|---|---|---|---|---|---|---|
| (KIT-6 80°C) | 8.4 | 7.0 | 3.2 | 733 (213) [c] | 0.88 (0.11) [c] | - |
| $Co_3O_4$ replica | 8.5 | 4.6 | 5.9 | 137 (-) [c] | 0.27 (-) [c] | 13 |
| (KIT-6 140°C) | 10.0 | 9.8 | 2.4 | 580 (70) [c] | 1.48 (0.03) [c] | - |
| $Co_3O_4$ replica | 10.0 | 5.5 | 6.7 | 77 (-) [c] | 0.14 (-) [c] | 15 |

[a] average pore diameter was determined by NLDFT data-based evaluation; [b] crystallite size was evaluated according to the SCHERRER equation; [c] micropore area and micropore volume determined by *t*-plot method according to BROEKHOFF and DE BOER

## 4.2.2 Synthesis Details: Morphology - Growth - Formation

The last section was focused on the relation between the structures of the mesoporous $Co_3O_4$ replicas and their respective matrices at the mesoscopic scale (porosity, mesoscopic order). For further elucidation of the nanocasting process the following part deals with the relation on the microscopic scale (morphology). This allows for some conclusions concerning the formation of mesoporous $Co_3O_4$ in the pores of the silica structure matrix. For this reason various mesoporous $Co_3O_4$ materials replicated from different silica structure matrices were investigated with respect to the particles' morphology and compared with those of their respective structure molds. Based on this the following study focuses on the formation of the $Co_3O_4$ replica inside the porous structure matrices. Therefore KIT-6/$Co_3O_4$ composite materials as well as the resulting silica-free $Co_3O_4$ replica particles after consecutive impregnation/oxide formation cycles were investigated.

## 4.2.2.1  Investigations on the Morphology of $Co_3O_4$

To study the morphology, various mesoporous $Co_3O_4$ materials replicated from small- and large-pore SBA-15 and small-pore KIT-6 silica were analyzed by scanning electron microscopy (SEM) and compared to that of their respective structural molds. To start with the morphology of the structure matrix for the hexagonal system, Figure 23 shows representative SEM images of mesoporous SBA-15 silica. Since the SEM images of SBA-15 with different pore sizes show no differences with respect to their morphology, only one overview (left) and one close-up view (right) are depicted, representative for both SBA-15 silica materials. A well-defined morphology of worm-like particles with an aspect ratio of *ca.* 1:4 is obtained for the SBA-15 silica. The particle size is about 1 μm in length and 0.5 μm in width. In the close-up view (right) the ordered porosity on the nanoscale can also be observed.
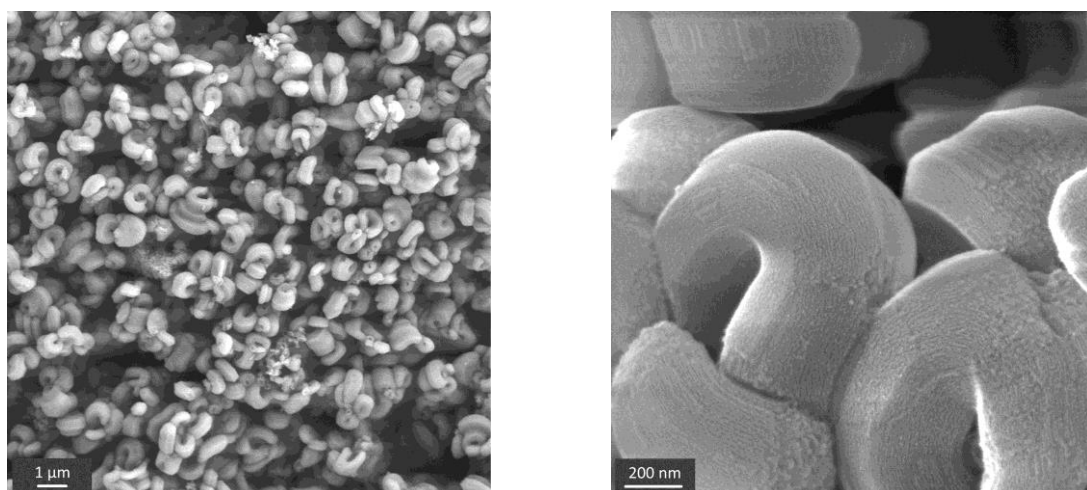


**Figure 23.** Representative SEM images of mesoporous SBA-15 silica,
an overview (left) and close-up view (right).[80]

Contrary to this, the $Co_3O_4$ replica particles from SBA-15 which was synthesized at 80 °C possess a visibly different morphology than the structure matrix. Figure 24 shows two representative SEM images of the respective $Co_3O_4$ sample.

The replica particles consist of bundled nanowires of different sizes and thicknesses (left); however the nanowires array are ordered to some degree, which is displayed in the close-up view (right). This is in good accordance with the results obtained from TEM (see Figure 18, left), already revealing this fibrous nanostructure and with the findings from low-angle XRD pattern (see Figure 17, left), indicating only a low mesoscopic order.
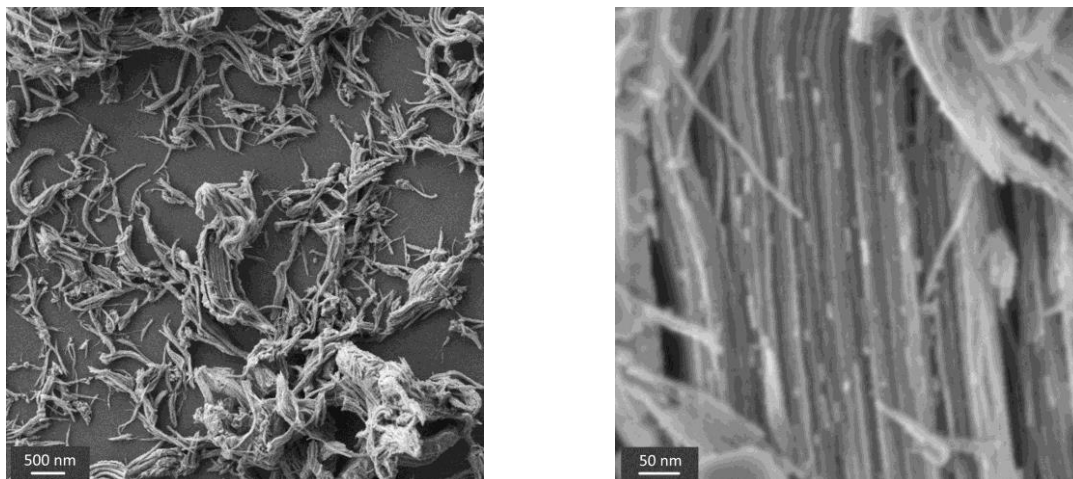
**Figure 24.** Representative SEM images of mesoporous $Co_3O_4$ replica from SBA-15 silica, synthesized at 80 °C. (Images were recorded on ZEISS NEON® 40 with CrossBeam®.)

$Co_3O_4$ replication from the larger-pore SBA-15 silica yields a more defined particle morphology; Figure 25 shows the respective SEM images. The particles reveal an ellipsoidal-like shape with considerably non-uniform particle sizes between 100 and 700 nm in length and 50 and 350 nm in width; however the aspect ratio is *ca.* 1:2 for nearly all particles. Due to a sufficient resolution of the SEM, also the porous nanostructure was observed, displayed in the close-up view (right). These findings of a more nanostructured network for $Co_3O_4$ (SBA-15 140 °C) compared to the bundles of nanowires obtained for $Co_3O_4$ (SBA-15 80 °C) are consistent with the results of the previously described TEM analysis. It can be assumed that again the pore interconnectivity of the matrices seems to play a significant role for the morphology of the resultant $Co_3O_4$ replica; detailed explanation approach of this observation will be given in the following section (see 4.2.2.2).
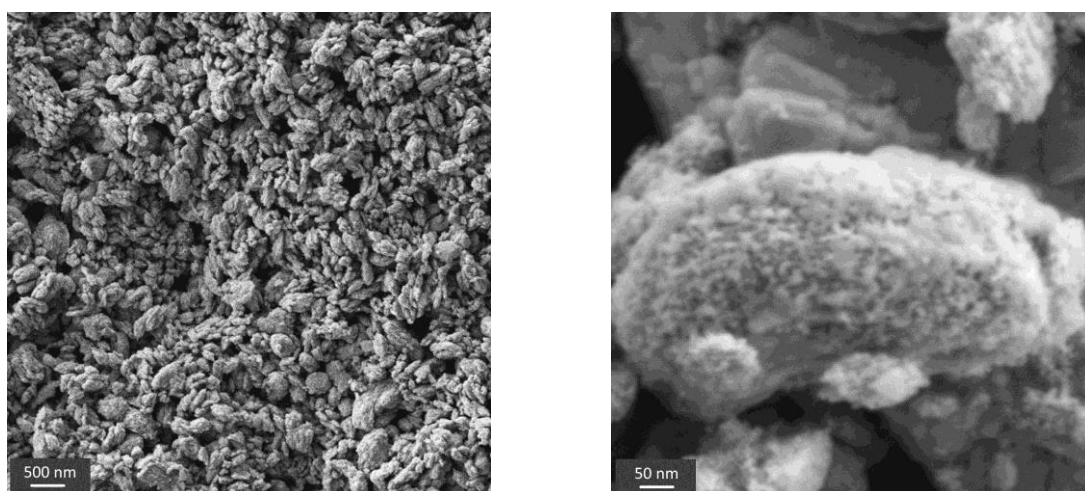


**Figure 25.** Representative SEM images of mesoporous $Co_3O_4$ replica from SBA-15 silica, synthesized at 140 °C. (Images were recorded on ZEISS NEON® 40 with CrossBeam®.)

Since, the pore interconnectivity of the structure matrices seems to contribute to the morphology of the resulting replica materials, KIT-6 with a highly branched pore network and the resulting $Co_3O_4$ replica were investigated next. To start again with the particle shape of the parental structure matrix, Figure 26 shows representative SEM images of mesoporous KIT-6 silica. The silica particles possess an irregular and ill-defined shape on the micrometer scale order.
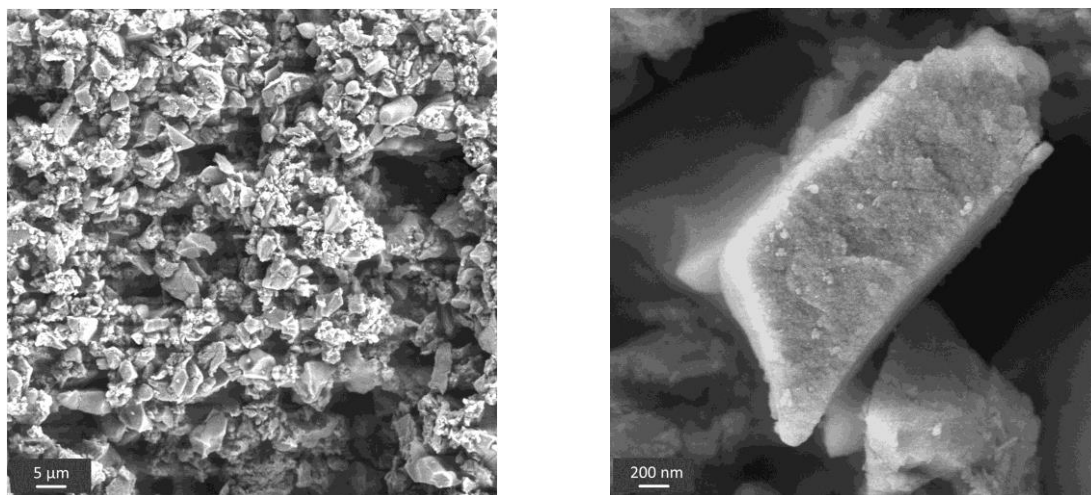


**Figure 26.** Representative SEM images of mesoporous KIT-6 silica,
an overview (left) and close-up view (right).[80]

In contrast to this, the morphology of the replica particles differs obviously; well-defined spherical particles of about 200 nm are obtained for the $Co_3O_4$ replica particles (see Figure 27). Due to a sufficient resolution the ordered nanoscale porosity is again visualized in the close-up view (right).
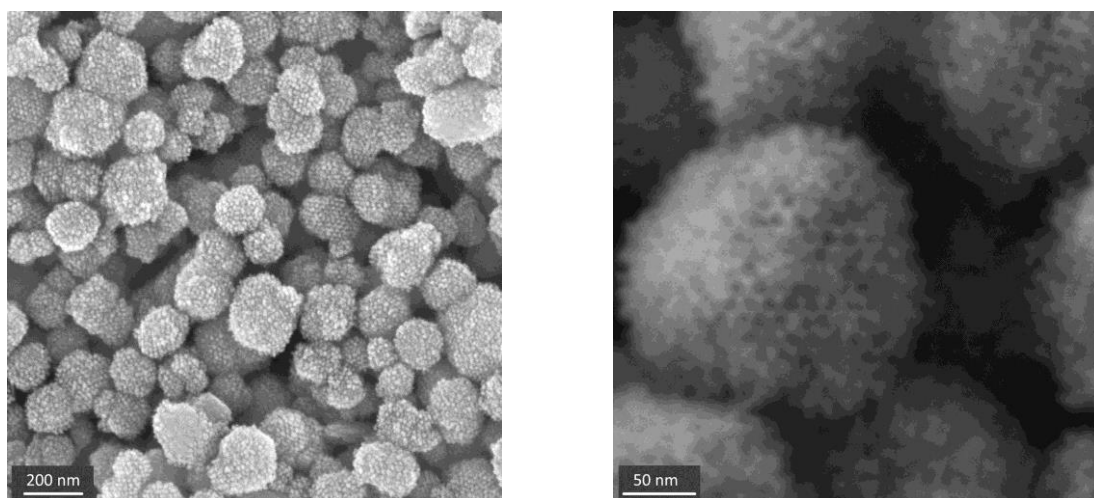


**Figure 27.** Representative SEM images of $Co_3O_4$ replica from KIT-6.

### 4.2.2.2 Investigations on the Growth of $Co_3O_4$ inside a Structure Matrix

In addition to the study on the morphology of mesoporous $Co_3O_4$ replica particles the formation of the replica particles inside a silica mold was also put into focus. In this context, a model has already been suggested for the growth of mesoporous $In_2O_3$.[80] This model is not universally applicable to all metal oxides; for example it has turned out not to work for $SnO_2$.[195] Hence, aim of this study was to elucidate the growth and formation of mesoporous $Co_3O_4$ inside the pores of a silica matrix. Therefore, aliquots of KIT-6/$Co_3O_4$composite materials as well as silica-free $Co_3O_4$ obtained after one, two and three impregnation/oxide formation cycles were characterized by powder X-ray diffraction and nitrogen physisorption analyses. The silica-free $Co_3O_4$ samples were additionally analyzed by SEM after one, two, and three cycles.

Figure 28 shows the low- and wide-angle XRD patterns of the KIT-6 silica and KIT-6/$Co_3O_4$ composite materials after consecutive impregnation/oxide formation cycles. The low-angle diffraction patterns (left) show the characteristic signature of cubic KIT-6 silica with the intense 211 reflection and the less-pronounced 220 while the further reflections 420 and 332 are only obtained for the KIT-6 as a small shoulder. For the composite materials the diffraction patterns are less pronounced, while the intensities of the reflections are reduced with increased number of impregnation/oxide formation cycles. However, these decreased intensities are consistent with a successive pore filling resulting in a decreased scattering contrast. The calculated $d$-values are constant for all samples (see Table 7) indicating that the replication occurs without any significant change in the size of the unit cell during the oxide formation.

The wide-angle diffraction patterns (right) of the KIT-6/$Co_3O_4$ composite materials show the same signature as described before for $Co_3O_4$ replication from KIT-6 (see Figure 20); already after one impregnation/oxide formation cycle crystalline $Co_3O_4$ spinel is obtained, while the size of crystalline domains slightly increases from 12 nm to 18 nm (see Table 7) determined by the SCHERRER equation (5) applied to the 311 peak.
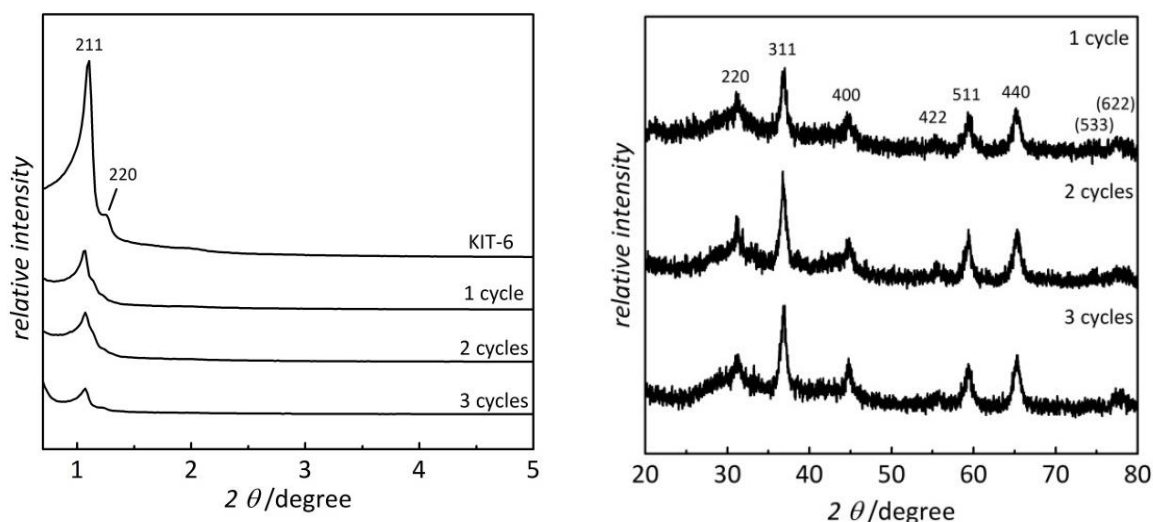
**Figure 28.** Low-angle X-ray diffraction patterns of KIT-6/Co$_3$O$_4$ composite materials before and after one, two and three impregnation/oxide formation cycles (left) as well as the corresponding wide-angle XRD patterns (right). For reasons of clarity the diffractograms are vertically shifted. (The low-angle XRD patterns were measured on a PANanalytical X'Pert Pro diffractometer.)

The successive pore filling from cycle to cycle is further confirmed by the nitrogen physisorption isotherms (Figure 29, left) for the KIT-6/Co$_3$O$_4$ materials. All isotherms exhibit a type-IV behavior with pronounced hysteresis indicating the presence of uniform mesopores while the amount of adsorbed nitrogen is reduced from impregnation/oxide formation cycle to cycle.
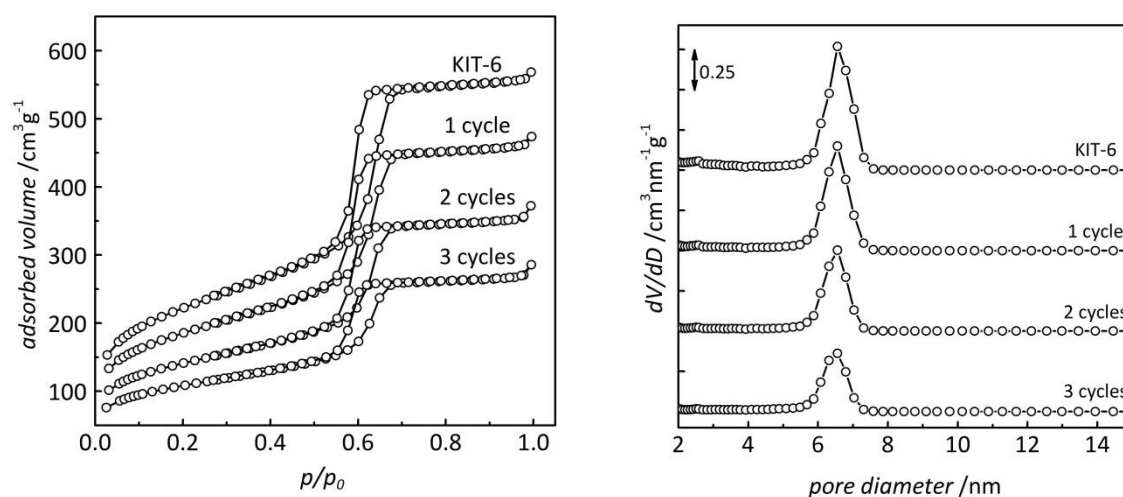


**Figure 29.** Nitrogen physisorption isotherms (left) and corresponding pore size distributions obtained by NLDFT data-based evaluation (right) of the same samples as in Figure 28. For reasons of clarity the pore size distributions are vertically shifted.

The corresponding pore size distribution, determined by the NLDFT data-based evaluation method (right), reveals that the peak maximum remains the same for all composite materials. Only the integral, which corresponds to the pore volume, decreases with an increased number of impregnation/oxide formation cycles.

Figure 30 shows the corresponding powder XRD patterns of the resulting $Co_3O_4$ samples after removal of the silica matrix. All three silica-free samples reveal the intense 211 and the weaker 220 reflections of the cubic $Ia\overline{3}d$ pore system symmetry of the parental KIT-6 silica matrix indicating a mesoscopic order already present for the $Co_3O_4$ replica obtained after only one impregnation/oxide formation cycle. Here, contrary to the before-described composite materials, the intensities of the reflections are increased with additional impregnation/oxide formation cycles and also becomes narrower, indicating larger coherent nanostructural scattering domains after each additional impregnation/oxide formation cycle. This means that an increased number of impregnation/oxide formation cycles yields a mesoporous material with higher structural order due to a more sufficient pore filling. The *d*-values remain constant, as already observed for the composite materials, indicating that the removal of the silica matrix also occurs without any change in unit cell (see Table 7).
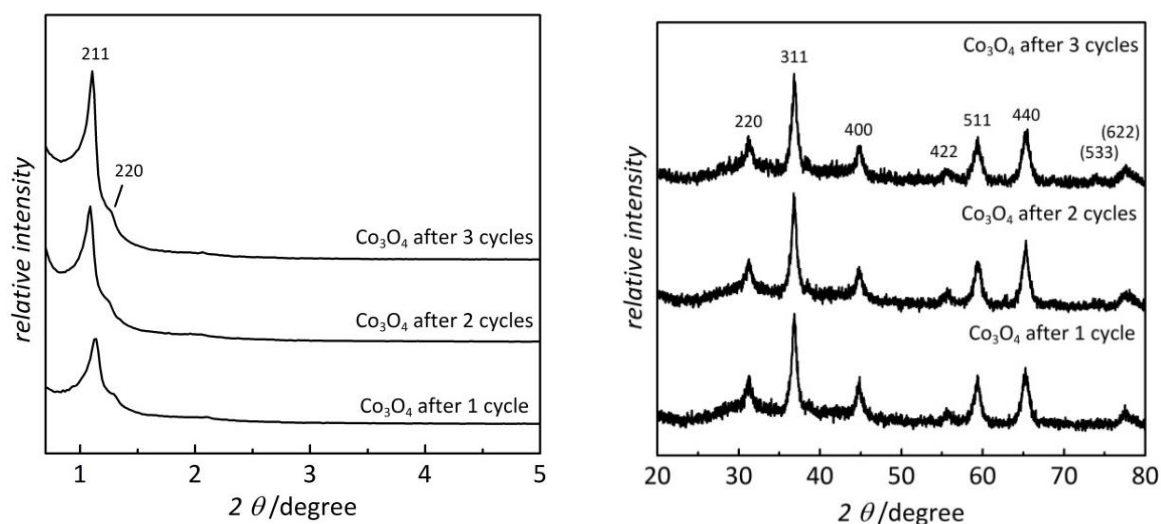


**Figure 30.** Low-angle X-ray diffraction patterns of the resulting silica-free $Co_3O_4$ replica materials after one, two and three impregnation/oxide formation cycles (left) and the corresponding wide-angle XRD patterns (right). For reasons of clarity the diffractograms are vertically shifted. (The low-angle XRD patterns were measured on a PANanalytical X'Pert Pro diffractometer.)

The wide-angle diffraction patterns (right) show a signature comparable to the composite materials (see Figure 28, right), with the reflections being more pronounced for the silica-free $Co_3O_4$ replica; however the crystallite sizes determined by the SCHERRER equation (5) are the same as those obtained for the composite materials (see Table 7), as expected.

Figure 31 shows the nitrogen physisorption isotherms (left) and the corresponding pore size distribution obtained by NLDFT data-based evaluation (right) of the silica-free $Co_3O_4$ samples. The isotherms of all three samples show a type-IV behavior with a weak hysteresis, which is consistent with the results described before for the replication of $Co_3O_4$ from KIT-6 silica (see Figure 22).

The corresponding pore size distributions obtained by the NLDFT data-based evaluation method for the silica-free $Co_3O_4$ samples do not differ significantly from each other; for all three samples the maximum is at 4.9 nm. Also the pore wall thickness was determined to 4.9 nm for each of three samples.
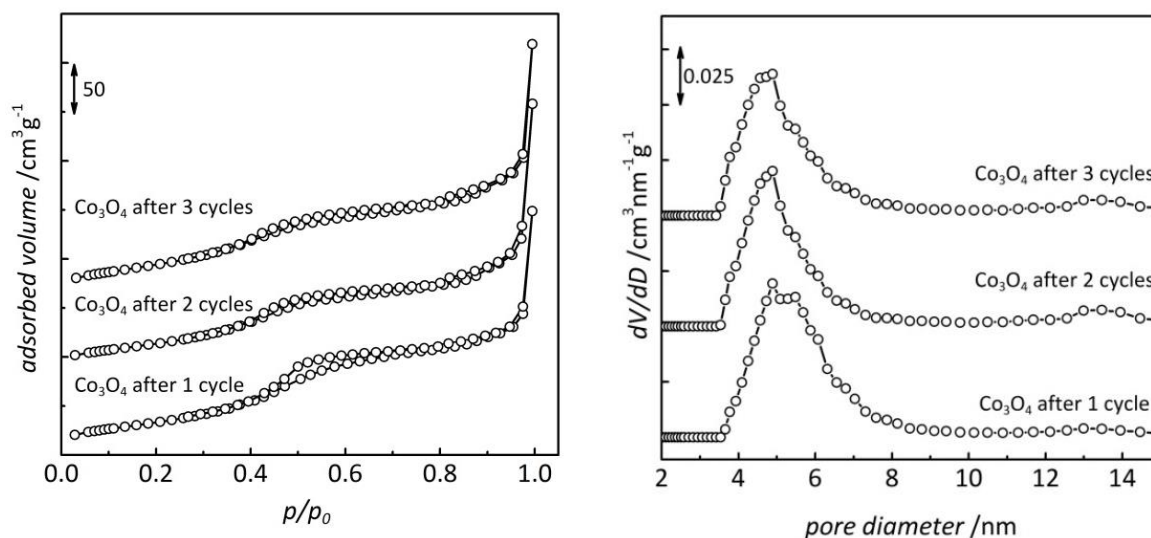


**Figure 31.** Nitrogen physisorption isotherms (left) and corresponding pore size distributions obtained by NLDFT data-based evaluation (right) of the same samples as in in Figure 30. For reasons of clarity the isotherms and the pore size distributions are vertically shifted.

Since the pore sizes and the pore wall thicknesses remain the same for the samples after one, two, and three consecutive impregnation/oxide formation cycles the evolution of $Co_3O_4$ seems to occur predominantly along the pore axis (Scheme 2, left). If the $Co_3O_4$ growth occurred perpendicular to the pore axis, either from the center to the pore wall (middle) or from the pore wall to the center (right), the pore size would shift with an increasing number of impregnation/oxide formation cycles, which is not observed. Based on these results it can

be assumed that the growth takes place in the same way as has been observed for $In_2O_3$ before.[80] Thus, the same model can be applied to describe the formation of mesoporous $Co_3O_4$ inside the pores of a structure matrix.



**Scheme 2.** Schematic drawing of potential growth directions of a mesoporous replica inside the pores of a silica structure matrix: along the pore axis (left), perpendicular to the pore axis starting from the center (middle) or from the pore walls (right).[80]

To describe the evolution of $Co_3O_4$ in more detail, the silica-free samples obtained after one, two and three impregnation/oxide formation cycles were further analyzed by scanning electron microscopy. Figure 32 shows the SEM images of the respective silica-free $Co_3O_4$ replica particles.
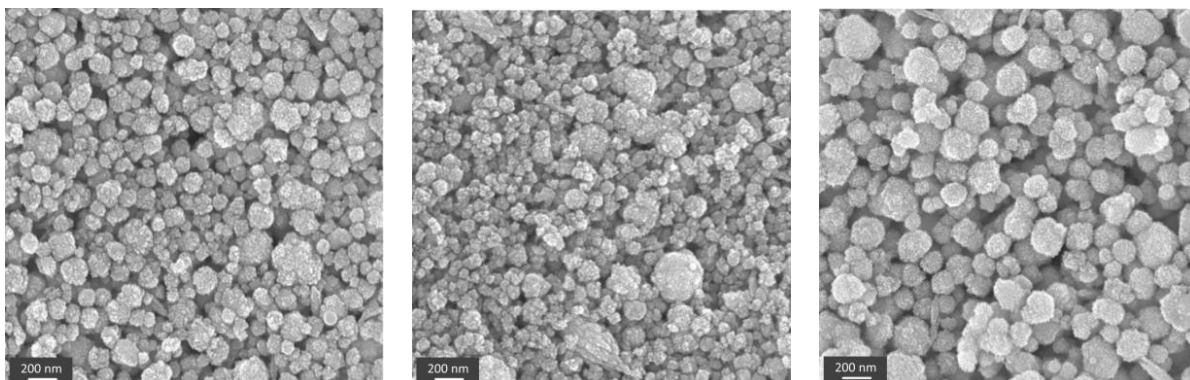


**Figure 32.** Representative SEM images of $Co_3O_4$ replica from mesoporous KIT-6 silica, obtained after one (left), two (middle) and three (right) cycles of impregnation and oxide formation.

All samples reveal almost spherical particle morphology and fairly uniform particle sizes, which increases with each additional cycle. The average particle size is determined to 180 (± 194) nm for the replica after one impregnation/oxide formation cycle, 202 (± 159) nm after two, and 233 (± 133) nm after three cycles; the values were obtained by measuring the diameter of about 500 particles in each sample. Based on these measured data for each sample the following particle size distribution of mesoporous $Co_3O_4$ replica particles after consecutive impregnation/oxide formation cycles was obtained (Figure 33; bars); the curves represent the log-normal distributions, fitted by a least-squares procedure.
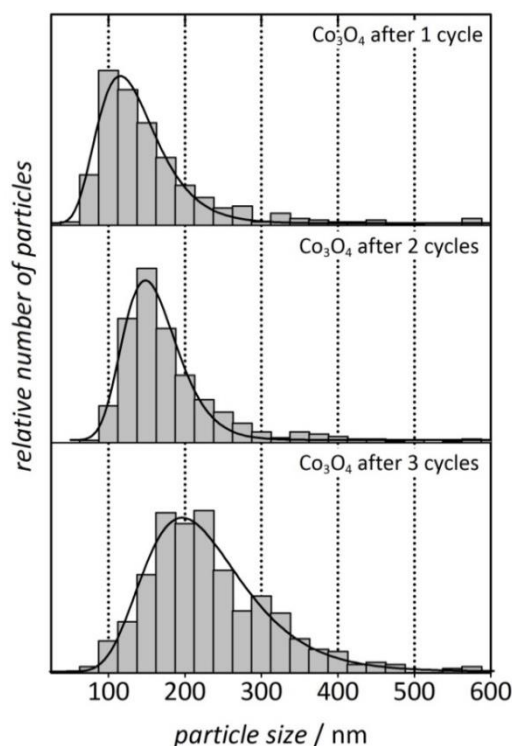
**Figure 33.** Particle size distributions of the mesoporous $Co_3O_4$ replica materials obtained from KIT-6 silica after one, two and three impregnation/oxide formation cycles.

It becomes obvious that not only the average particles size increases with every cycle, but also the onset of the curves shifts to larger sizes, which means that further impregnation/oxide formation cycles lead to growth of already existing particles rather than to nucleation of new (smaller) ones.

The observed findings are notable, particularly taking into account that the morphology of the parental KIT-6 structure matrix is irregular (see Figure 26) and significantly larger by about one order of magnitude (about 2 μm) than the resulting spherical mesoporous $Co_3O_4$ replica particles (about 200 nm).

The finding of spherical morphology of the replica particles which become larger with additional impregnation/oxide formation cycles but are considerably smaller than the KIT-6 particles suggests that the pores of the silica matrix get completely filled with $Co_3O_4$ only in some fractions whereas the pores in other regions seem to stay unfilled. Since similar findings were obtained for $In_2O_3$[80] the corresponding model can also be applied to describe the growth of $Co_3O_4$. Scheme 3 shows a schematic drawing of the evolution of $Co_3O_4$ particles inside a KIT-6 silica matrix from cycle to cycle.
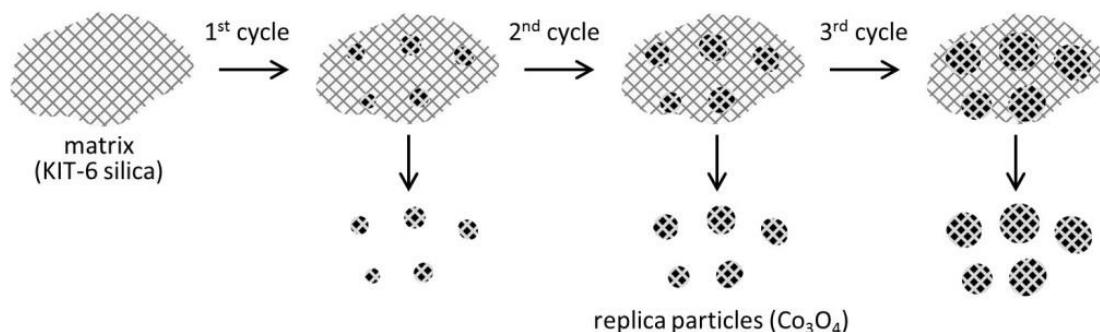
**Scheme 3.** Schematic drawing of the growth of $Co_3O_4$ particles inside the pores of KIT-6 silica matrix. Scheme is modified from reference.[80]

To explain the spherical morphology and the growth of the $Co_3O_4$ replica particles, formation of $Co_3O_4$ 'islands' within the pores of the silica matrix is assumed with $Co(NO_3)_2$ either in solution or in the molten phase forming droplets inside the pores. This formation of droplets is facilitated by the strongly branched pore channels of KIT-6 silica with high pore interconnectivity. Additional impregnation/oxide formation cycles result in an attachment of precursor species to the surface of already existing replica particles rather than to nucleation of new ones, which leads to larger spherical particles.

Apart from the increase of particle size with additional impregnation/oxide formation cycles, interestingly, the size of the crystalline domains also seems to grow slightly (see Table 7); this was observed for $In_2O_3$ as well and might indicate that $Co_3O_4$ particles grow with a certain degree of epitaxial attachment.

This model based on droplet formation strongly depends on the pore interconnectivity of the silica structure matrix. In case of a mesoporous silica matrix with lower pore interconnectivity, like in SBA-15, less well-defined spherical particle morphology can be expected. This is consistent with the above-presented SEM images of the $Co_3O_4$ samples replicated from SBA-15 with different pore interconnectivities (see Figure 24 and Figure 25). Mesoporous SBA-15 silica synthesized at 80 °C with only low pore interconnectivity yield ellipsoidal replica particles, whereas this morphology is less-pronounced in case of the SBA-15 material synthesized at 140 °C serving as structure matrix. Thus, the different morphologies that have been observed before (see 4.2.2.1) can be explained by this mechanism depending on the choice of the utilized structure matrix.

SBA-15-80

3 cycles

template removal

SBA-15-140

3 cycles

template removal
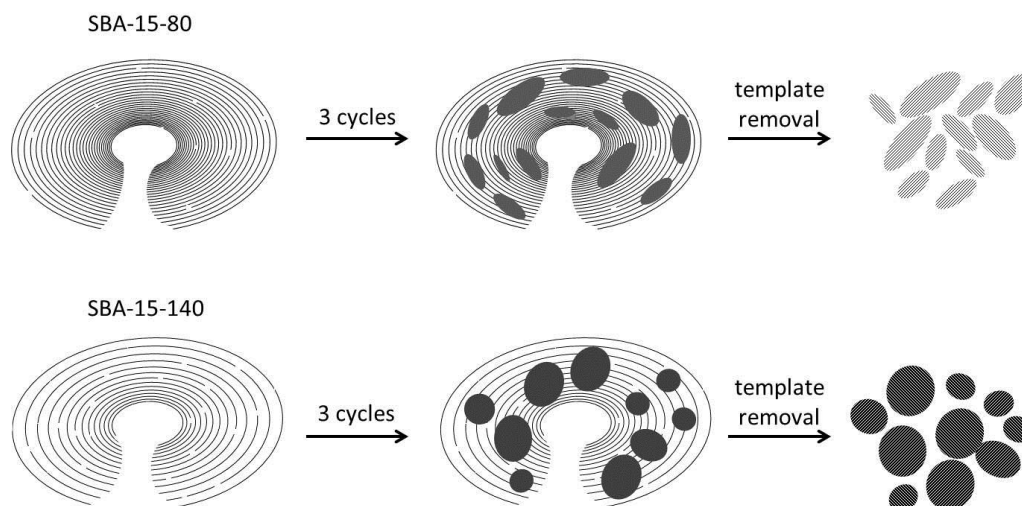
**Scheme 4.** Schematic drawing of the formation of $Co_3O_4$ particles inside the pores of SBA-15 silica matrices. Scheme is modified from reference.[80]

For illustration, Scheme 4 shows a schematic drawing for the formation of $Co_3O_4$ inside the pores of SBA-15 silica structure matrices with different pore interconnectivity. Contrary to the formation of spherical droplets inside the three-dimensionally interconnected pores of KIT-6, only droplets with a preferred orientation along the pore axes are possible in case of the $Co_3O_4$ replica from SBA-15, leading to ellipsoidal $Co_3O_4$ replica particles. The latter are less pronounced for the large-pore SBA-15 silica, since the pore interconnectivity is not as low as for the SBA-15 silica with small pores. These findings are consistent and confirm the before-described model for KIT-6.

In summary, it was shown that replication occurs at the nanometer (mesopores system) but not on the micrometer (morphology) scale. Mesoporous $Co_3O_4$ replica materials can be obtained with a well-defined morphology either from mesoporous silica materials with (SBA-15) or without (KIT-6) defined morphology of their own; hence the morphological properties of the replica particles are not associated with those of their structure molds. These findings can be explained by the assumption of droplet formation inside the pores of a silica matrix which is also reasonable for the growth of $Co_3O_4$ material in a silica matrix.

All structural data obtained from powder X-ray diffraction analysis and nitrogen physisorption measurements of the discussed samples, including the KIT-6/$Co_3O_4$ composite materials before, after one, two, and three impregnation/oxide formation cycles as well as those of the resulting silica-free samples, are listed in Table 7.

**Table 7.** Structural parameters from P-XRD and $N_2$ physisorption of the KIT-6/$Co_3O_4$ composite and the resulting silica-free $Co_3O_4$ replica materials.

| | $d_{211}$/ nm | average pore diameter [a] / nm | average pore wall thickness / nm | specific BET surface area / $m^2g^{-1}$ | specific pore volume / $cm^3g^{-1}$ | crystallite size [b] / nm |
|---|---|---|---|---|---|---|
| KIT-6 | 8.0 | 6.6 | 3.2 | 763 | 0.86 | - |
| 1 cycle | 8.0 | 6.6 | 3.2 | 633 | 0.69 | 12 |
| 2 cycles | 8.0 | 6.6 | 3.2 | 483 | 0.53 | 14 |
| 3 cycles | 8.0 | 6.6 | 3.2 | 368 | 0.40 | 18 |
| $Co_3O_4$, 1 cycle | 8.0 | 4.9 | 4.9 | 126 | 0.22 | 12 |
| $Co_3O_4$, 2 cycles | 8.0 | 4.9 | 4.9 | 126 | 0.22 | 14 |
| $Co_3O_4$, 3 cycles | 8.0 | 4.9 | 4.9 | 130 | 0.22 | 17 |

[a] average pore diameter was determined by NLDFT data-based evaluation; [b] crystallite size was evaluated according to the SCHERRER equation

### 4.2.3  Synthesis Details: Temperature Stability - Crystallinity

Two issues that are of particular interest when considering potential applications of mesoporous materials are crystallinity and thermal stability.[11] Thus, the following investigations focus on the temperature stability and the crystallinity of mesoporous $Co_3O_4$ replicated from KIT-6. Therefore, a post-synthetic thermally treatment at variable temperatures (300, 400, 500 and 600 °C; see 3.2.1) of a $Co_3O_4$ material was carried out and the thus-obtained samples were analyzed by powder X-ray diffraction and nitrogen physisorption measurements; the $Co_3O_4$ sample which was thermally treated at 600 °C was additionally characterized by electron microscopy. In a further study, the surrounding atmosphere during the oxide formation was varied (see 3.2.1), which was shown to have an impact on the crystallinity of the final product, as very recently reported by SUN et al.[59]

### 4.2.3.1 Investigations on Temperature Stability

Figure 34 shows the results from powder X-ray diffraction measurements of the mesoporous $Co_3O_4$ samples which were post-synthetically thermally treated at various temperatures; a non-tempered $Co_3O_4$ sample is shown for comparison. The low-angle diffraction patterns (left) reveal almost the same signature for the samples with a thermal treatment up to 500 °C as for the non-tempered reference sample, confirming that the mesostructural order is still persistent at 500 °C. In contrast, the sample which was thermal treated at 600 °C suffers from substantial loss in mesostructural order; only a weak shoulder in the low-angle diffraction pattern is observed for this $Co_3O_4$ sample.
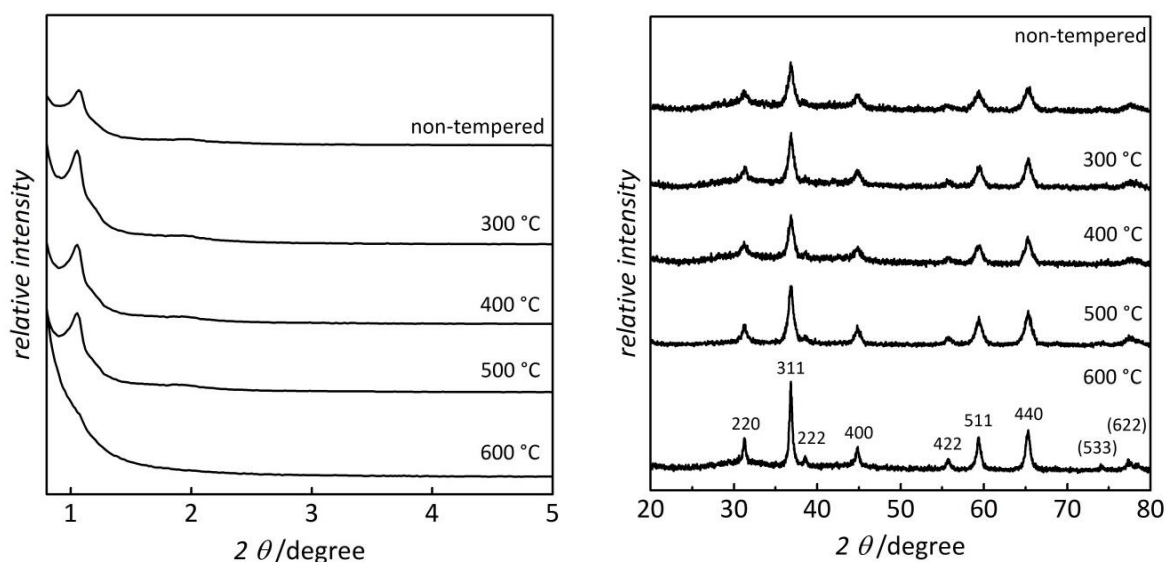


**Figure 34.** Low- and wide angle X-ray diffraction patterns of mesoporous $Co_3O_4$ after post-synthetic thermal treatment at various temperatures; a non-tempered sample is shown as reference. For reasons of clarity the diffractograms are vertically shifted. (The low-angle XRD patterns were measured on a PANanalytical X´Pert Pro diffractometer.)

The corresponding wide-angle diffraction patterns (right) exhibit the characteristic reflections of the cubic spinel phase for all samples, while the peaks are more pronounced for the sample thermal treated at 600 °C. The full width at half maximum (FWHM) for this sample is substantially smaller than that of the other four samples exhibiting almost the same FHWM for each sample. The crystallite sizes were determined by the SCHERRER equation (5) applied to the 311 peak to 13 and 15 nm for the samples treated at 300, 400 and 500 °C, while the crystallites of 26 nm are significantly larger for the sample treated at 600 °C (see Table 8). To conclude, thermal treatment at 600 °C is associated with a

significant loss in the mesoscopic order, while at the same time the crystallite size is increased.

The porosity of the samples was analyzed by nitrogen physisorption measurements; the results are shown in Figure 35. The isotherms (left) show the same behavior (type IV with weak hysteresis) as already described before for mesoporous $Co_3O_4$ (see 4.2.1.2) for the samples which were thermally treated up to 500 °C, whereas the isotherms of the sample treated at 600 °C reveal a different behavior; the hysteresis that is observed for the other four samples is missing for the sample thermally treated at 600 °C.

The corresponding pore size distributions obtained by NLDFT data-based evaluation (right) further confirms the loss of the mesoscopic pore system for the sample which was thermally treated at 600 °C as it was already indicated by powder X-ray diffraction analysis. The peak which slightly increases from 4.6 nm for the non-tempered $Co_3O_4$ sample to 4.9 nm for the sample treated at 500 °C (see Table 8) is completely absent for the sample thermally treated at 600 °C. The deviation in the pore size of the other four samples can be explained by a densification of the $Co_3O_4$ pore walls caused by the thermal treatment resulting in a slight widening of the pores.
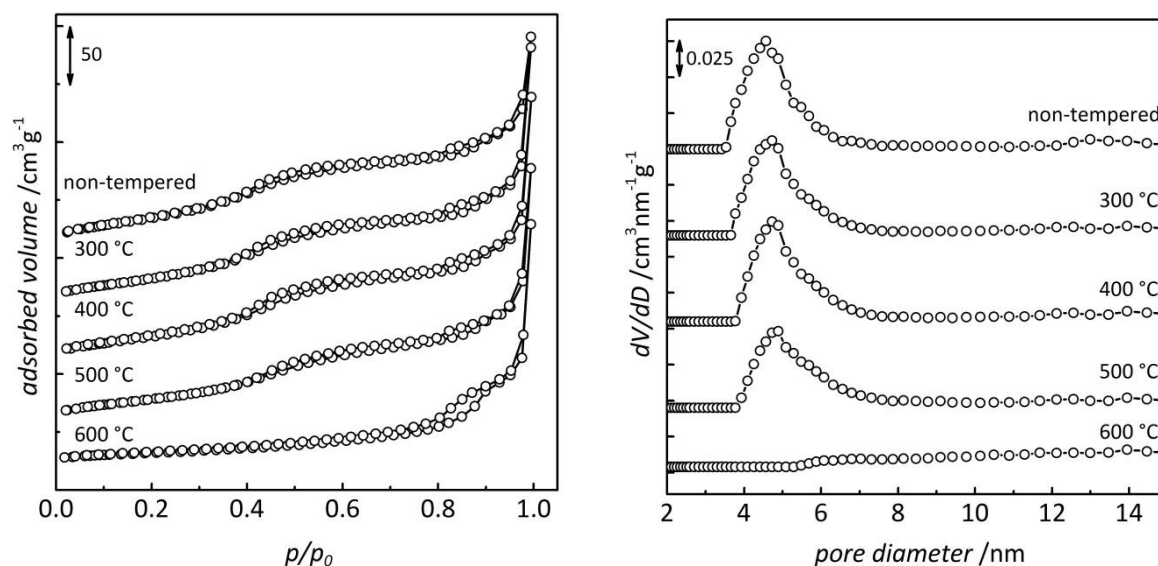


**Figure 35.** Nitrogen physisorption isotherms (left) and corresponding pore size distributions obtained by NLDFT data-based (right) of the same samples as in Figure 34. For reasons of clarity the isotherms and the pore size distributions are vertically shifted.

The specific BET surface areas decrease with increasing temperature during the thermal treatment. This is only less pronounced between the four mesoporous $Co_3O_4$ samples that

were thermal treated up to 500 °C, whereas the deviation is more significant by comparing the $Co_3O_4$ samples after thermal treatment at 500 ° C and 600 °C. The BET value is decreased to only 32 % of the initial surface area of the non-tempered sample. Similar findings concerning the relation between specific BET surface area and temperature of post-synthetic treatment were also observed for mesoporous $In_2O_3$ by WAITZ et al.[94]

The mesoscopic structure of the $Co_3O_4$ sample which was thermally treated at 600 °C was supplementary investigated by electron microscopy. The transmission electron microscopic image (Figure 36, left) reveals that the mesoscopic order of the particles still exists to some degree while also fractions of non-porous material are observed. The latter might explain the higher crystallinity detected in the wide-angle P-XRD (see Figure 34, right) and SAED (inset) patterns. The formation of non-porous material is also consistent with the substantial decrease in specific surface area. The corresponding scanning electron microscopic image (right) corroborates these findings; about the half of the particles visible in the image can be described as non-porous.
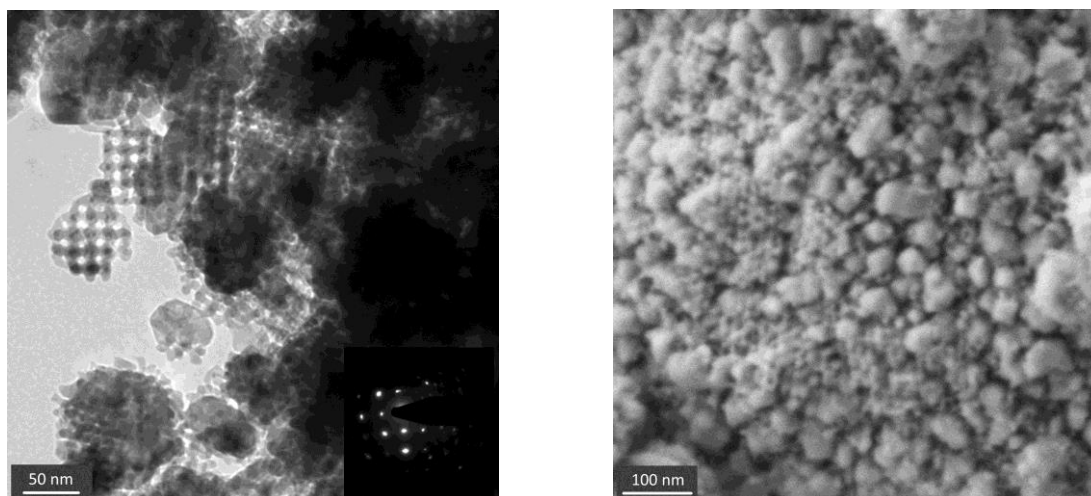


**Figure 36.** Representative transmission (left) and scanning (right) electron microscopic images of the (mesoporous) $Co_3O_4$ sample which was post-synthetic thermal treated at 600 °C. Inset of the TEM image shows the corresponding SAED pattern. (SEM image was recorded on ZEISS NEON® 40 with CrossBeam®.)

All structural data obtained from the powder X-ray diffraction analysis and $N_2$ physisorption measurements of the mesoporous $Co_3O_4$ samples with a post-synthetic thermal treatment at variable temperatures and those of the non-tempered sample for comparison are listed in Table 8.

**Table 8.** Structural parameters from P-XRD and $N_2$ physisorption of the $Co_3O_4$ materials after post-synthetic thermal treatment at 300, 400, 500, 600 °C compared to a non-tempered sample.

| | $d_{211}$ / nm | average pore diameter [a] / nm | average pore wall thickness / nm | specific BET surface area / $m^2g^{-1}$ | specific pore volume / $cm^3g^{-1}$ | crystallite size [b] / nm |
|---|---|---|---|---|---|---|
| non-tempered | 8.3 | 4.6 | 5.6 | 133 | 0.22 | 15 |
| 300 °C | 8.4 | 4.7 | 5.6 | 124 | 0.21 | 13 |
| 400 °C | 8.4 | 4.7 | 5.6 | 123 | 0.22 | 13 |
| 500 °C | 8.4 | 4.9 | 5.4 | 106 | 0.21 | 15 |
| 600 °C | - | - | - | 43 | 0.18 | 26 |

[a] average pore diameter was determined by NLDFT data-based evaluation; [b] crystallite size was evaluated according to the SCHERRER equation

## 4.2.3.2 Investigations on Crystallinity

A recently reported approach to control the crystallinity of replica particles involves a variation of the synthesis conditions during the oxide formation; the surrounding atmosphere was shown to have an impact on the final replication product.[59] Therefore one sample was prepared as usual while for another sample the oxide formation was carried out in a closed vessel instead of an open one (see 3.2.1); the respective samples are denoted as '$Co_3O_4$ (open vessel)' and '$Co_3O_4$ (closed vessel)'.

Figure 37 shows the powder X-ray diffraction patterns of the mesoporous $Co_3O_4$ samples which were obtained under varied surrounding atmospheres during the oxide formation; the low-angle diffraction patterns (left) exhibit one well-resolved peak indicating a mesoscopic order in both cases.

The corresponding wide-angle diffraction patterns (right), however, differ from each other; the reflections of mesoporous $Co_3O_4$ which was formed in a closed vessel are significantly sharper with smaller FHWMs. The crystallite sizes were determined by applying the SCHERRER equation (5) to the 311 peak to 49 nm compared to 14 nm for the 'closed vessel' and 'open vessel' $Co_3O_4$ samples. Thus, the crystallites are substantially larger in case of an oxide formation occurring under closed environment atmosphere compared to the usually applied conditions of an open environment during the synthesis.
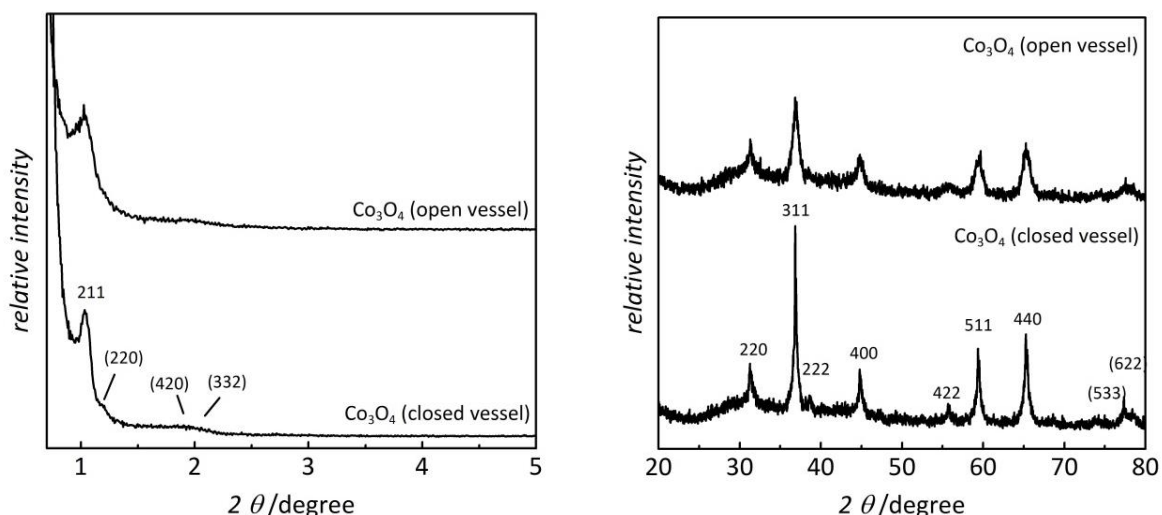
**Figure 37.** Low- and wide-angle X-ray diffraction patterns of mesoporous $Co_3O_4$ which was converted into the oxide in a 'closed vessel' compared to the synthesis in an 'open vessel'. For reasons of clarity the diffractograms are shifted.

The porosity was analyzed by $N_2$ physisorption measurements. The corresponding isotherms of both samples are shown in Figure 38 (left). Both samples show isotherms with weak hysteresis which is broader for the 'closed vessel' sample. This is also reflected in the corresponding pore size distributions determined by the NLDFT data-based evaluation method (right) which is slightly broader for this sample; however the maximum obtained at 4.9 nm is the same for both samples. The respective specific BET surface areas of the 'closed vessel' sample is 96 $m^2g^{-1}$, slightly lower as compared to 132 $m^2g^{-1}$ of the reference $Co_3O_4$ sample (see Table 9).
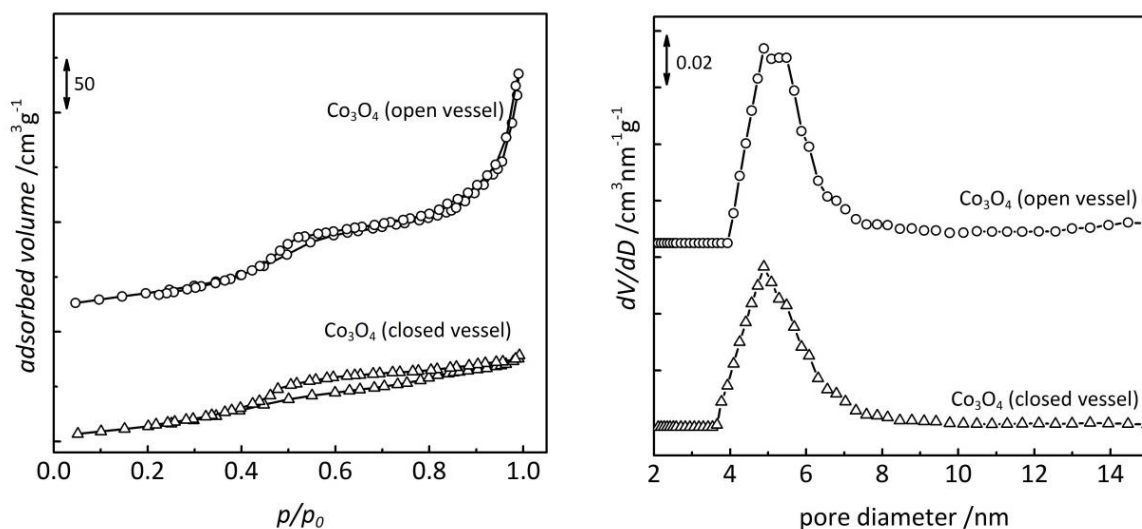


**Figure 38.** Nitrogen physisorption isotherms (left) and corresponding pore size distributions obtained by NLDFT data-based evaluation (right) of the same samples as in Figure 37. For reasons of clarity the isotherms and the pore size distributions are vertically shifted.

Thus, the synthesis in a 'closed vessel' instead of an 'open vessel' seems to yield $Co_3O_4$ with large crystalline domains of about 50 nm while mesoporosity is still obtained. However, upon closer inspection of the $Co_3O_4$ (closed vessel) sample by electron microscopy (Figure 39), these results have to be considered with caution. Both transmission (left) and scanning (right) electron microscopic images show that indeed a well-ordered mesostructured material is obtained, which is consistent with the low-angle P-XRD pattern and the $N_2$ physisorption analysis, but also formation of bulk-phase material is observed which may be responsible for the large crystalline domains, as it was also observed for the previously described samples (see 4.2.3.1). The presence of large crystalline domains is further confirmed by selected area electron diffraction pattern (inset), revealing a well-pronounced dot pattern. However, it is conspicuous that the bulk-phase material is particularly formed at the surface regions of the porous particles. Since such a formation of large fractions of bulk-phase material preferably attached to the mesoporous particles was not obtained for all the previously presented mesoporous $Co_3O_4$ samples synthesized in an 'open vessel' (see Figure 21, left and Figure 27) the surrounding atmosphere seems to be the origin for these findings.
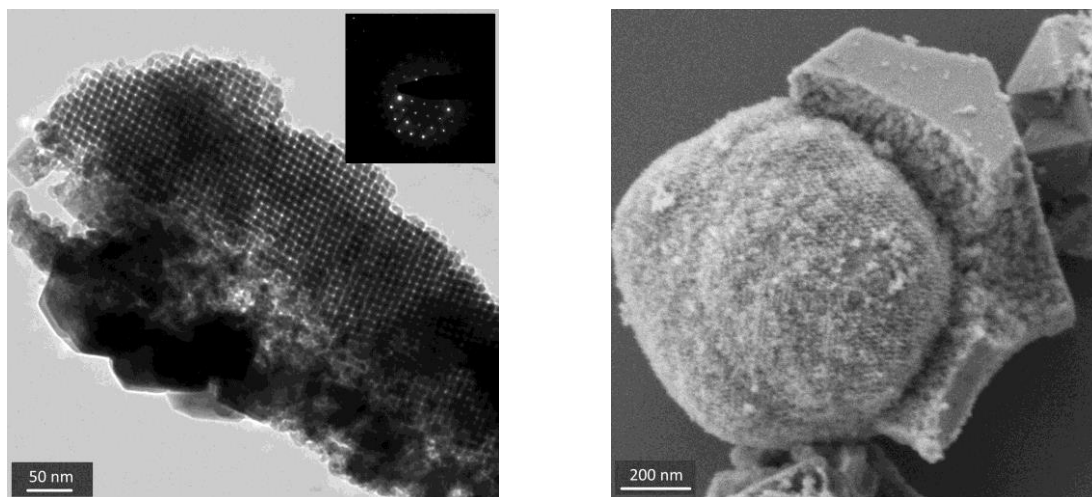


**Figure 39.** Representative transmission (left) and scanning (right) electron microscopic images of the (mesoporous) $Co_3O_4$ sample which was converted into the oxide in a 'closed vessel'. Inset of the TEM image shows the corresponding SAED pattern. (SEM Image was recorded on ZEISS NEON® 40 with CrossBeam®.)

To sum up, it was shown that mesoporous $Co_3O_4$ is thermally stable up to ca. 500 °C; at higher temperatures the specific BET surface area substantially decreases to only 32 % of the initial value. At the same time the crystallinity is significantly increased for the sample thermally treated at 600 °C while the differences in the crystallite sizes for the temperature

treatment in the range between 300 and 500 °C are only slight. However, the substantially larger crystallites after thermal treatment at 600 °C seem to be a result of bulk-phase formation associated with a loss in structural mesoscopic order. A similar situation is obtained by variation of the surrounding atmosphere during the conversion into the oxide; employing a closed vessel for the oxide formation instead of an open one yields $Co_3O_4$ with an increased degree of crystallinity while mesoscopic order is still obtained contrary to the before-mentioned study. However, again the higher crystallinity seems to be a result of formation of bulk-phase material and not only caused by actual, larger crystalline domains of the mesoporous material itself. These results show that further investigations concerning the direct impact of the two approaches on the pore wall's crystallinity needs to be carried out.

The structural data obtained from powder X-ray diffraction analysis and $N_2$ physisorption measurements of the two mesoporous $Co_3O_4$ samples synthesized under different environmental conditions during the oxide formation are listed in Table 9.

**Table 9.** Structural parameters from P-XRD and $N_2$ physisorption of $Co_3O_4$ converted into the oxide in a closed vessel compared to a synthesis in an open vessel.

| | $d_{211}$ / nm | average pore diameter [a] / nm | average pore wall thickness / nm | specific BET surface area / $m^2g^{-1}$ | specific pore volume / $cm^3g^{-1}$ | crystallite size [b] / nm |
|---|---|---|---|---|---|---|
| $Co_3O_4$ (open vessel) | 8.4 | 4.9 | 5.4 | 132 | 0.33 | 14 |
| $Co_3O_4$ (closed vessel) | 8.4 | 4.9 | 5.4 | 96 | 0.13 | 49 |

[a] average pore diameter was determined by NLDFT data-based evaluation; [b] crystallite size was evaluated according to the SCHERRER equation

### 4.2.4  Nanostructure-Related Magnetic Properties

As described in 1.2.1 bulk-phase $Co_3O_4$ exhibits antiferromagnetic behavior; however nanoscale materials have been shown to reveal different magnetic behavior compared to bulk-phase.[91,92,180,181] Therefore the following part initially concerns the structure-related magnetic behavior of nanostructured mesoporous $Co_3O_4$ obtained by nanocasting (see 4.2.1). Additionally the magnetic behavior of various mesoporous $Co_3O_4$ samples,

different in their nanostructural properties, was investigated particularly with respect to the impact of 'surface area' and 'size'. The different $Co_3O_4$ materials were prepared by varying the synthesis conditions, as it was described in more detail in the previous sections (see 3.2.1 and 4.2.2).

### 4.2.4.1  Magnetic Behavior of Mesoporous $Co_3O_4$

Figure 40 (left) shows the field-dependent magnetization of one representative mesoporous $Co_3O_4$ sample (replicated from KIT-6 synthesized at 80 °C) measured at 10 K and 300 K as well as the temperature-dependent molar susceptibility (right) measured under zero-field-cooled (ZFC) and field-cooled (FC) conditions. For the zero-field-cooled measurement the sample was cooled from room temperature down to 10 K without an external field applied, and then the sample was warmed up from 10 K to 300 K, now at an applied field of 5 kOe, while the magnetization was measured in dependence of the temperature. Next, the sample is cooled down again to 10 K in the same applied field while the magnetization is measured (FC). The temperature-dependent magnetization curve shows the characteristic behavior of an antiferromagnetic material.[181] The curve exhibits a peak with a maximum at 30 K, which corresponds to the Néel temperature ($T_{Néel}$), the temperature where an antiferromagnetic material becomes paramagnetic. This Néel temperature of 30 K for the mesoporous $Co_3O_4$ is lower than that for bulk-phase $Co_3O_4$ where the transition occurs at 40 K.[128]
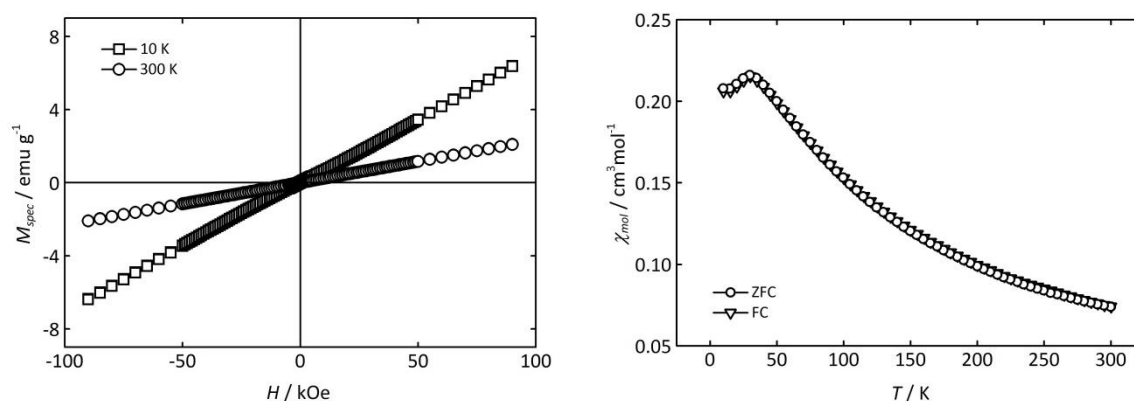


**Figure 40.** Field-dependent magnetization (left) and temperature-dependent molar susceptibility (right) of mesoporous $Co_3O_4$.

However, some authors reported lower values for $T_{Néel}$ of bulk-phase $Co_3O_4$, such as 30 K observed by DUTTA et al.[181] This Néel temperature was obtained by a slightly different way, namely as the peak maximum in the temperature derivative of the susceptibility ($d(\chi_{mol}T)/dT$

versus T plot). The thus-obtained peak occurs at a slightly lower temperature than the peak in the temperature-dependent susceptibility curve ($\chi_{mol}$ versus $T$ plot), this means that $T_{N\acute{e}el}$ is slightly lower than the maximum of the peak in the temperature-dependent susceptibility curve. Applying this method here to determine the Néel temperature, Figure 41 shows the respective temperature derivative curve of the susceptibility. Here, the maximum is at 25 K, which is lower than 30 K obtained before from Figure 40 (right); however this deviation is consistent with the results from DUTTA et al.[181] The field-dependent magnetization shows the typical behavior of an antiferromagnet increasing linearly with the applied field.
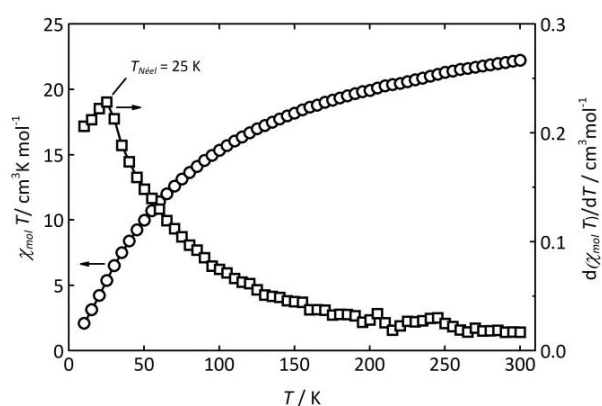


**Figure 41.** *($\chi_{mol}$ T)* and d*($\chi_{mol}$ T)*/d*T* versus *T* plot for determination of the Néel temperature.

### 4.2.4.2  Impact of the Nanostructure on the Magnetic Behavior

The influence of structural properties like BET surface area and crystallite sizes on the magnetic behavior was investigated in more detail; therefore a systematic variation of the nanostructural parameters by controlling the synthesis conditions was carried out. To start with mesoporous $Co_3O_4$ samples which were replicated from various structural molds, Figure 42 (left) shows the field-dependent specific magnetization measured at 10 K of four mesoporous $Co_3O_4$ materials and bulk-phase $Co_3O_4$; the mesoporous samples were replicated from different silica matrices, namely SBA-15 and KIT-6, both synthesized at 80 °C and 140 °C, resulting in 7.0 nm and 9.8 nm pores, respectively (see Table 12).
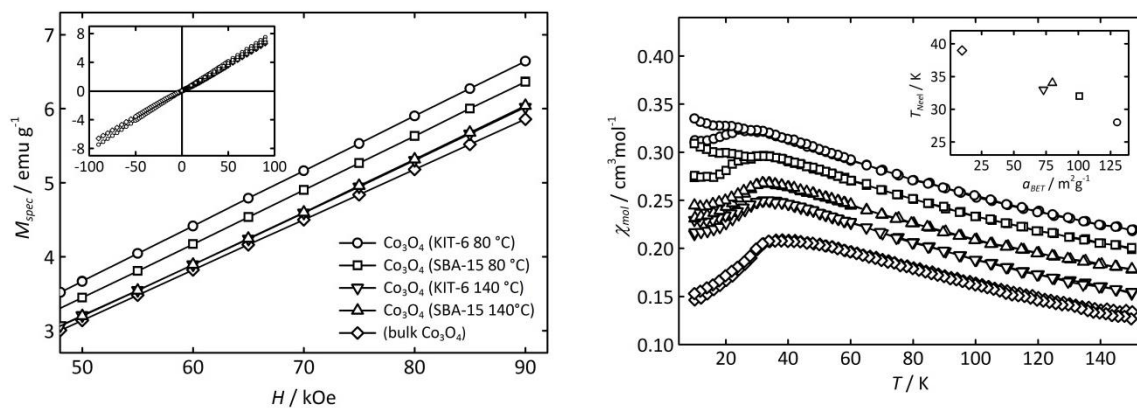
**Figure 42.** Field-dependent magnetization (left) and temperature-dependent molar susceptibility (right; same legend as left) of mesoporous $Co_3O_4$ replicated from various silica matrices (SBA-15 and KIT-6, both with varied pore sizes). Insets show overall measurement range (left) and the correlation of the Néel temperature with the BET surface area (right). For reasons of clarity the curves of the temperature-dependent measurements are vertically shifted.

The magnetic behavior is different for the four samples; slight differences in the slope of the magnetization curves are visible (left). This can be attributed to the respective BET surface areas (see Table 10); the larger the BET surface area, the steeper is the slope in the magnetization curve which corresponds to higher magnetic moments. By comparing the mesoporous samples with the bulk-phase $Co_3O_4$ this trend is confirmed, since the bulk-phase sample with the smallest BET surface area shows the lowest slope. This correlation stands to reason since a disruption of the antiferromagnetic ordering is to be expected in the surface-near regions; this has been subjected for nanostructured $Co_3O_4$ materials,[181] as well as mesoporous ones.[92,180] An antiferromagnet can be described by two sublattices with opposed spins resulting in a complete magnetic compensation. However, this antiferromagnetic compensation remains incomplete at the surface, where the neighbors with opposite spins are missing. This effect becomes increasingly significant in materials with high surface-to-volume ratios. The uncompensated remaining spins at the surface result in a paramagnetic moment or even in weak ferromagnetism.[88,196,197] In fact, upon closer inspection, the mesoporous $Co_3O_4$ samples show small hysteresis loops; the coercivity fields are between 188 and 329 Oe as a result of a weak ferromagnetic ordering at the surface. Contrary to this, the bulk-phase $Co_3O_4$ sample exhibits a coercivity of only 70 Oe. The hystereses caused by the weak ferromagnetism are depicted in Figure 43, which is a blow-up of the field-dependent magnetization (see Figure 42, left) of two $Co_3O_4$ samples, exemplarily of mesoporous $Co_3O_4$ replicated from KIT-6 with a synthesis temperature of 80 °C and of the

bulk-phase sample. The formation of small hysteresis was also found in nanoscale $Co_3O_4$.[197,198]
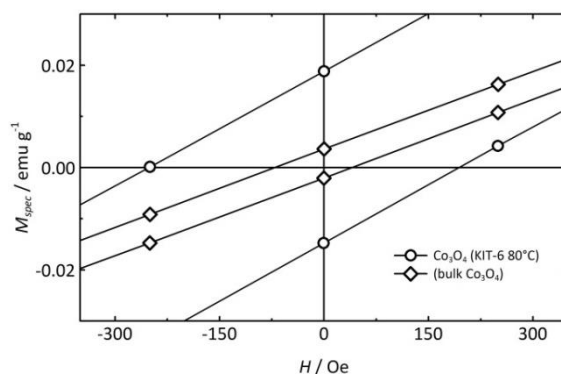


**Figure 43.** Blow-up of the field-dependent magnetization of two $Co_3O_4$ samples, exemplarily of the mesoporous $Co_3O_4$ sample replicated from KIT-6 synthesized at 80 °C and of the bulk-phase $Co_3O_4$ to show the weak ferromagnetism.

It was found that the degree of deviation from bulk-like behavior is indeed directly correlated to the surface-to-volume ratio of the respective samples (see Table 10). The same obvious trend is obtained for the Néel temperatures of the same samples.

Figure 42 (right) depicts the temperature-dependent molar susceptibility, measured under zero-field-cooled (ZFC) and under field-cooled (FC) conditions in an applied field of $H$ = 500 Oe. The curves of the mesoporous samples partly differ from that of bulk-phase $Co_3O_4$; a bifurcation of the ZFC and FC curve is observed for two mesoporous samples. This was also observed by Dutta et al. for $Co_3O_4$ nanoparticles, explained by superparamagnetic blocking.[181]

The temperature-dependent curves exhibit for each sample a relative maximum that corresponds to the Néel temperature of the respective samples. Since here only the trend of the Néel temperature was of interest, the temperature derivative plot of the susceptibility for a more precise determination of $T_{Néel}$ as it has been depicted in Figure 42 is not shown for these samples. The values for $T_{Néel}$ obtained as the relative maximum of the temperature-dependent curves are plotted as a function of the BET surface areas (inset of Figure 42, right). A clear correlation is observed again: the larger the surface-to-volume ratio, the lower is the Néel temperature; this is in good accordance with what has been described qualitatively before.[88]

**Table 10.** BET surface areas and crystallite sizes for the mesoporous $Co_3O_4$ materials replicated from various silica matrices and for bulk-phase $Co_3O_4$.

|  | specific BET surface area / $m^2 g^{-1}$ | crystallite size / nm |
|---|---|---|
| $Co_3O_4$ (KIT-6 80 °C) | 130 | 17 |
| $Co_3O_4$ (SBA-15 80 °C) | 101 | 19 |
| $Co_3O_4$ (KIT-6 140 °C) | 73 | 15 |
| $Co_3O_4$ (SBA-15 140 °C) | 80 | 16 |
| (bulk-phase $Co_3O_4$) | < 50 | 57 |

Upon closer inspection, the BET surface area is not the only difference in the nanostructural properties between the respective samples; also the crystallite sizes determined by the SCHERRER equation (5) reveal slight differences ranging from 15 nm to 19 nm for the mesoporous ones and 57 nm for the bulk-phase material (see Table 10).This means that the samples are also different from each other with respect to the interface between adjacent crystallites (solid-solid interfaces); this will make a contribution to the before-mentioned disruption in antiferromagnetic ordering just as much as the BET surface areas (solid-gas interfaces).

Indeed, the solid-solid interfaces were approximately calculated by a simple geometric model assuming a spherical shape of non-porous crystallites with a bulk density of 6.1 $gcm^{-3}$ according to equation (6); the thus-obtained values are in the same order of magnitude as the BET surface areas.

$$A_{cryst} = \frac{6}{s_{cryst} \cdot \rho} \qquad (6)$$

| $A_{cryst}$ | = | solid-solid interfaces |
|---|---|---|
| $s_{cryst}$ | = | crystallite sizes |
| $\rho$ | = | bulk-phase density (6.1 g $cm^{-3}$) |

Obviously, these differences may have an impact on the magnetic behavior additionally to the BET surface areas, although the latter one seems to be the more dominating factor for these measurements. However, the contribution of this solid-solid interface needs to be investigated in more detail.

Therefore, further mesoporous $Co_3O_4$ samples were prepared from the same silica matrix (KIT-6 80 °C) by the procedure described in the previous section (see 4.2.2). The thus-obtained materials after one, two and three impregnation/oxide formation cycles possess almost the same BET surface area but are different from each other with respect to their crystallite sizes resulting in different solid-solid interfaces (see Table 11).

**Table 11.** BET surface areas and crystallite sizes for the $Co_3O_4$ replica materials obtained by one, two and three impregnation/oxide formation cycles and for bulk-phase $Co_3O_4$.

|  | specific BET surface area / $m^2 g^{-1}$ | crystallite size / nm |
|---|---|---|
| $Co_3O_4$ after 1 cycle | 126 | 12 |
| $Co_3O_4$ after 2 cycles | 126 | 14 |
| $Co_3O_4$ after 3 cycles | 130 | 17 |
| (bulk-phase $Co_3O_4$) | < 50 | 57 |

Figure 44 shows the magnetization curves of the respective samples as well as the bulk-phase sample for comparison. Again, differences in the slope of the field-dependent magnetization curves (left) are observed. Contrary to the samples discussed before, these differences cannot be attributed to the BET surface areas since they are almost the same for these samples within the limit of accuracy of the BET measurements; here, the crystallite sizes seem to be the more relevant factor instead. As already discussed, smaller crystallite sizes result in larger solid-solid interfaces (see equation (6)) and will contribute to the disruption of antiferromagnetic ordering just as much as the solid-gas interface. This is explicitly confirmed by the observations in Figure 44; the slope becomes steeper for smaller crystallites, *i.e.* larger solid-solid interfaces.
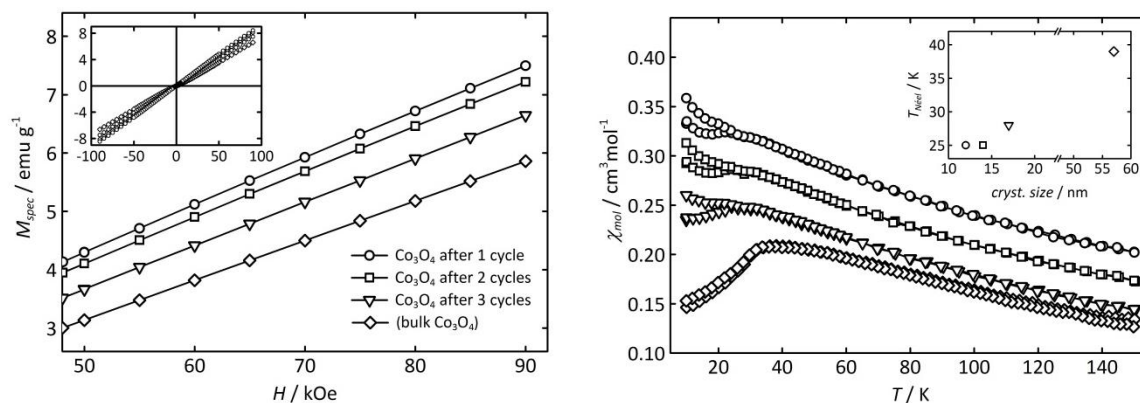
**Figure 44.** Field-dependent magnetization (left) and temperature-dependent molar susceptibility (right, same legend as left) of mesoporous $Co_3O_4$ replicated from KIT-6 silica obtained after one, two and three impregnation/ oxide formation cycles. Insets show overall measurement range (left) and the correlation of the Néel temperature with the crystallite size (right). For reasons of clarity the curves of the temperature-dependent measurements are vertically shifted

Figure 44 (right) shows the corresponding temperature-dependent susceptibility of these samples and reveals the same trend; the smaller the crystallite sizes (larger solid-solid interface), the lower is the Néel temperature. This variation of the Néel-temperature is consistent with the considerations described before. The correlation of the crystallite sizes and the Néel temperature is plotted as well (inset).

In summary, by a systematic variation of the nanostructural parameters it was confirmed that the magnetic behavior of nanostructured $Co_3O_4$ is different from that of bulk-phase $Co_3O_4$. Particularly the slope of the field-dependent magnetization curve is steeper, indicating stronger magnetic moments, the Néel temperature is shifted to lower values, and a small ferromagnetic contribution evolves. These findings can be explained by disruptions in the antiferromagnetic ordering due to nanostructural size confinement, as has been described by some authors.[88,92,181] Moreover, it turns out to be mandatory to distinguish clearly between several aspects of 'nanostructure'. It becomes apparent that the terms 'surface area' and 'size' need to be differentiated with caution, since the 'solid-gas interface' (BET surface area) and the 'solid-solid interface' (between adjacent single-crystalline domains) play important individual roles. Both need to be taken into account when the magnetic behavior is assessed since both interfaces have an impact on the disruptions of antiferromagnetic ordering. Likewise, the terms 'crystallite size' and 'particle size' may not necessarily be the same; an entire particle could also exist of more than one individual single-crystalline domains. These two differentiations ('solid-solid interface' vs. 'solid-gas interface' and 'particle size' vs. 'crystallite size') which have to be accounted for when

interpreting the magnetic behavior of nanostructured materials are schematically illustrated in Scheme 5.
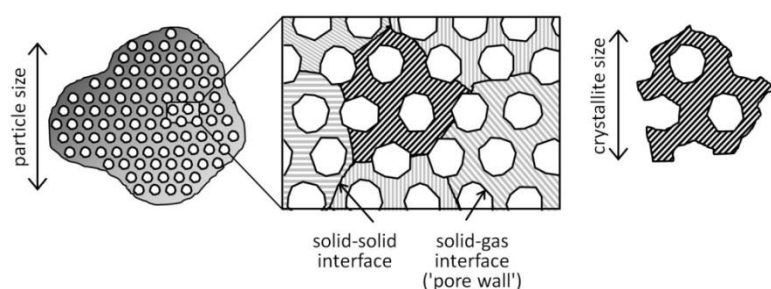


**Scheme 5.** Schematic drawing to illustrate the differentiation of 'solid-solid interface' vs. 'solid-gas interface' and 'particle size' vs. 'crystallite size'.

All structural data obtained from powder X-ray diffraction analysis and $N_2$ physisorption measurements of the various $Co_3O_4$ samples and those of the utilized structure matrices are listed in Table 12 and Table 13.

**Table 12.** Structural parameters from P-XRD and $N_2$ physisorption of the mesoporous $Co_3O_4$ materials replicated from four different silica matrices, SBA-15 and KIT-6, both with two different pore sizes, respectively.

| | $d^{[a]}$ / nm | average pore diameter [b] / nm | average pore wall thickness / nm | specific BET surface area / $m^2g^{-1}$ | specific pore volume / $cm^3g^{-1}$ | crystallite size [c] / nm |
|---|---|---|---|---|---|---|
| SBA-15 (80 °C) | 8.8 | 7.0 | 3.2 | 750 | 0.91 | - |
| $Co_3O_4$ replica | 8.5 | 4.2 | 5.6 | 101 | 0.19 | 19 |
| SBA-15 (140 °C) | 9.6 | 9.8 | 1.3 | 460 | 1.16 | - |
| $Co_3O_4$ replica | 9.7 | 5.6 | 5.6 | 80 | 0.17 | 16 |
| KIT-6 (80 °C) | 8.4 | 7.0 | 3.2 | 733 | 0.88 | - |
| $Co_3O_4$ replica | 8.5 | 4.6 | 5.9 | 130 | 0.23 | 17 |
| KIT-6 (140 °C) | 10.0 | 9.8 | 2.4 | 580 | 1.48 | - |
| $Co_3O_4$ replica | 10.0 | 5.5 | 6.7 | 73 | 0.18 | 15 |

[a] $d_{100}$ in case of the hexagonal pore system, $d_{211}$ for the cubic pore system; [b] average pore diameter was determined by NLDFT data-based evaluation; [c] crystallite size was evaluated according to the SCHERRER equation

**Table 13.** Structural parameters from P-XRD and $N_2$ physisorption of the $Co_3O_4$ replica materials obtained after one, two and three impregnation/oxide formation cycles.

| | $d_{211}$ / nm | average pore diameter [a] / nm | average pore wall thickness / nm | specific BET surface area / $m^2g^{-1}$ | specific pore volume / $cm^3g^{-1}$ | crystallite size [b] / nm |
|---|---|---|---|---|---|---|
| KIT-6 (80 °C) | 8.0 | 6.6 | 3.2 | 763 | 0.86 | - |
| $Co_3O_4$, 1 cycle | 8.0 | 4.9 | 4.9 | 126 | 0.22 | 12 |
| $Co_3O_4$, 2 cycles | 8.0 | 4.9 | 4.9 | 126 | 0.22 | 14 |
| $Co_3O_4$, 3 cycles | 8.0 | 4.9 | 4.9 | 130 | 0.22 | 17 |

[a] average pore diameter was determined by NLDFT data-based evaluation; [b] crystallite size was evaluated according to the SCHERRER equation

## 4.3    Mesoporous Cobalt Iron Oxide

### 4.3.1   Structural Characterization of Mesoporous Cobalt Iron Oxide

Mesoporous cobalt iron oxide ($CoFe_2O_4$) was obtained by structure replication in a similar way as described for $Co_3O_4$ before (see 4.2.1). However, the synthesis of ternary metal oxides by nanocasting is not that straightforward as in case of the binary analogues that are accessible in a large variety. Particularly a well-balanced mixture of the metal salts serving as reactants, which is prerequisite for the desired stoichiometry of the product, often bears a challenge. For example, differences in the solubility of the two precursors may result in phase separation, so that after the conversion into the oxide a mixture of the two binary metal oxides is formed instead of the desired ternary phase. Thus the first part of this section focuses on the structural characterization of successfully obtained mesoporous cobalt ferrite replicated from KIT-6 silica (see 3.2.2).

Figure 45 shows the results from powder X-ray diffraction analyses: the low-angle diffraction pattern (left) exhibits one well-resolved reflection and three less pronounced peaks. Those are indexable to 211 and 220, 420 and 332 according to the cubic $Ia\bar{3}d$ symmetry of KIT-6 silica utilized as the structural mold. This result reveals that the mesoscopic order has been retained during the structure replication process. The $d$-value is determined to 8.8 nm for

cobalt ferrite, which is slightly larger than that of the structure matrix, determined to 8.4 nm (see Table 14), so that the replication has occurred with only slight change in the periodic size of the mesoscopic structure.

The corresponding wide-angle diffraction pattern (right) reveals the signature of cobalt ferrite with a cubic spinel structure (JCPDS 22-1086). The crystallite size was determined by the SCHERRER equation (5) applied to the 311 peak to 11 nm (see Table 14) which is slightly smaller than the crystallites (13 nm) obtained for the binary cobalt oxide replicated from KIT-6 (see 4.2.1, Table 6).
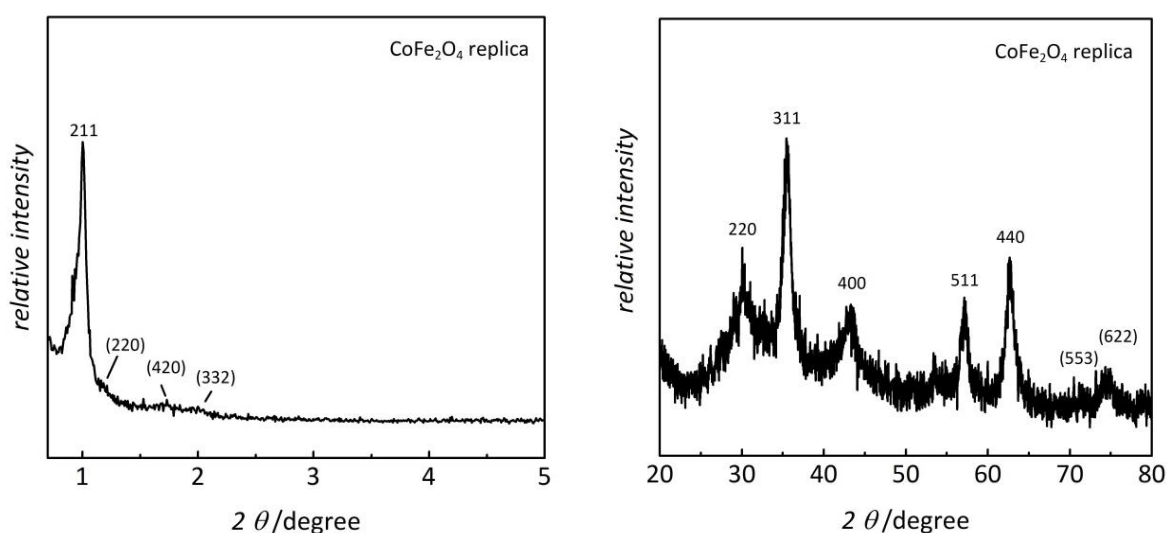


**Figure 45.** Low- and wide-angle X-ray diffraction patterns of mesoporous $CoFe_2O_4$ obtained by nanocasting from KIT-6 (80 °C).

The mesostructural order was further confirmed by transmission electron microscopy (Figure 46); the image also shows the tortuosity (left) of the pore system replicated from KIT-6. The inset depicts the corresponding SAED pattern with spots and concentric diffraction rings to some degree. This corroborates the presence of only small crystalline domains, which is consistent with the results from the wide-angle diffraction pattern (see Figure 45, right). Energy-dispersive X-ray diffraction (EDX) analysis at 6 different spots yields a silica amount of less than 5 % and a Co:Fe ratio of 1:2. This confirms the desired stoichiometry and the presence of ternary cobalt iron oxide instead of a mixture of the binary oxides ($Co_3O_4$ and $Fe_2O_3$).
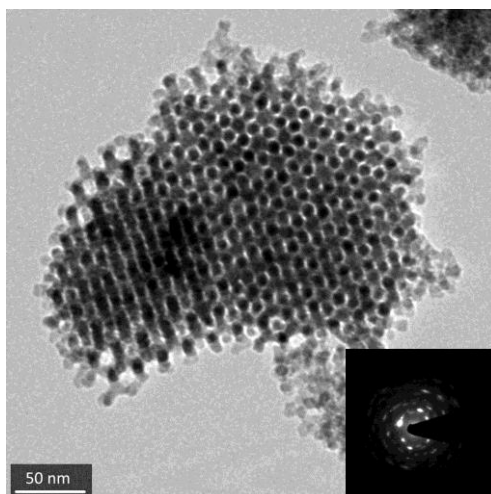
**Figure 46.** Representative TEM image of mesoporous $CoFe_2O_4$ obtained by nanocasting from KIT-6, synthesized at 80 °C and corresponding SAED pattern (inset).

Nitrogen physisorption measurements are depicted in Figure 47; the isotherms (left) show a type-IV behavior with weak hysteresis indicating the presence of uniform mesopores. The capillary condensation occurs at a relative pressure of about $p/p_0$ = 0.4.
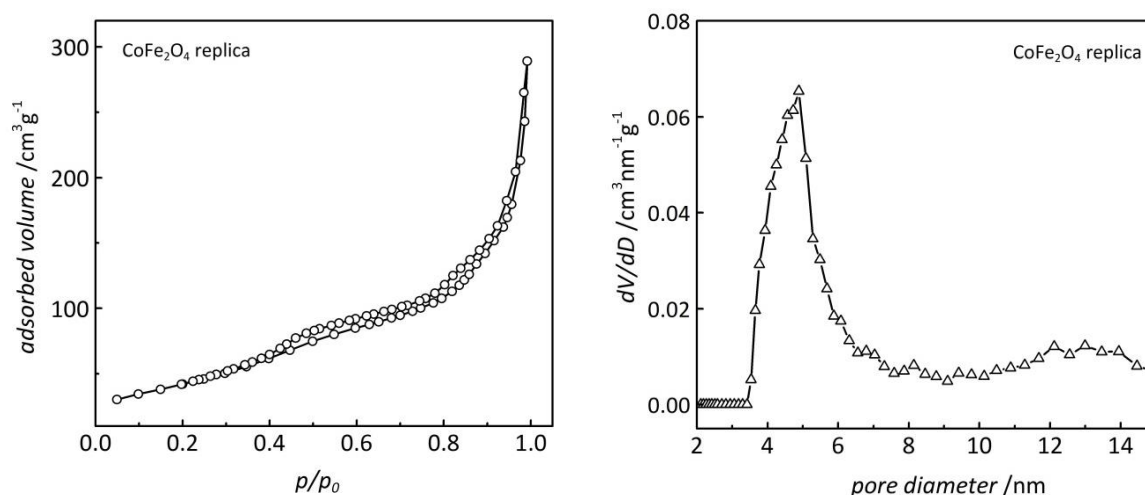


**Figure 47.** Nitrogen physisorption isotherms (left) and corresponding pore size distribution obtained by NLDFT data-based evaluation (right) of mesoporous $CoFe_2O_4$ replicated from KIT-6, synthesized at 80 °C.

The corresponding pore size distribution obtained by NLDFT data-based evaluation (right) reveals one pronounced peak with a maximum at 4.9 nm and an additional broad (less pronounced) peak at about 13 nm. The presence of the latter one may be attributed to interparticle porosity which causes the second capillary condensation step that is observed in the physisorption isotherms at a relative pressure of about $p/p_0$ = 0.8. The pore wall thickness was determined to 5.9 nm which is smaller than the pore size (7.0 nm) of the

utilized silica structure matrix (see Table 14). The same deviation was also observed for $Co_3O_4$ and can be explained by an incomplete pore filling and/or by the volume shrinkage that is frequently associated with the oxide formation due to densification from the nitrate precursor to the respective oxide. This aspect has already been discussed in more detail for the binary cobalt oxide (see 4.2.1 and Table 12).

The specific surface area as well as the total pore volume is 160 $m^2g^{-1}$ and 0.38 $cm^3g^{-1}$, respectively, which are in the range of the values obtained for the analogous binary cobalt oxide replicated from KIT-6 (Table 12). However, the specific BET surface area of the cobalt iron oxide is slightly larger; this may be attributed to the difference in their (bulk-) densities ($\rho$ = 5.3 g $cm^{-3}$ of $CoFe_2O_4$ vs. $\rho$ = 6.11 g $cm^{-3}$ of $Co_3O_4$).[193,199] Overall, the specific surface areas are lower than that of the utilized KIT-6 structure matrix, as already discussed in more detail in previous sections, including the differences in densities, the absence of microporosity (see Table 14) as well as the surface roughness.

Additionally, analysis by scanning electron microscopy was carried out. Figure 48 shows two representative SEM images of the mesoporous $CoFe_2O_4$ sample replicated from KIT-6. The replica particles exhibit an almost spherical morphology, especially for the larger ones, whereas also small fractions of particles with irregular morphology are observed (left). The particles are about 200 nm in size which is comparable to the particle size obtained for binary cobalt oxides (see 4.2.2.2). Thus, similar to binary cobalt oxide materials, the formation of a spherical morphology of the $CoFe_2O_4$ replica particles also seems to be preferred in case of replication from KIT-6 silica with cubic ordered pore system symmetry. However, it needs to be investigated in further studies analogous to the above-described investigation (see 4.2.2) if the same growth mechanism as has been proposed for the binary $Co_3O_4$ (see Scheme 3) could also be applied for the ternary $CoFe_2O_4$. Due to sufficient resolution of the SEM the close-up view displays the (ordered) porous nanostructure (right).

In summary, the structure replication process was shown to be also successful in the synthesis of a ternary metal oxide; mesoporous cobalt iron oxide with a cubic spinel structure was obtained by replication from KIT-6 silica. The thus-obtained replica possesses a well-ordered pore system and high specific surface area of about 160 $m^2g^{-1}$.
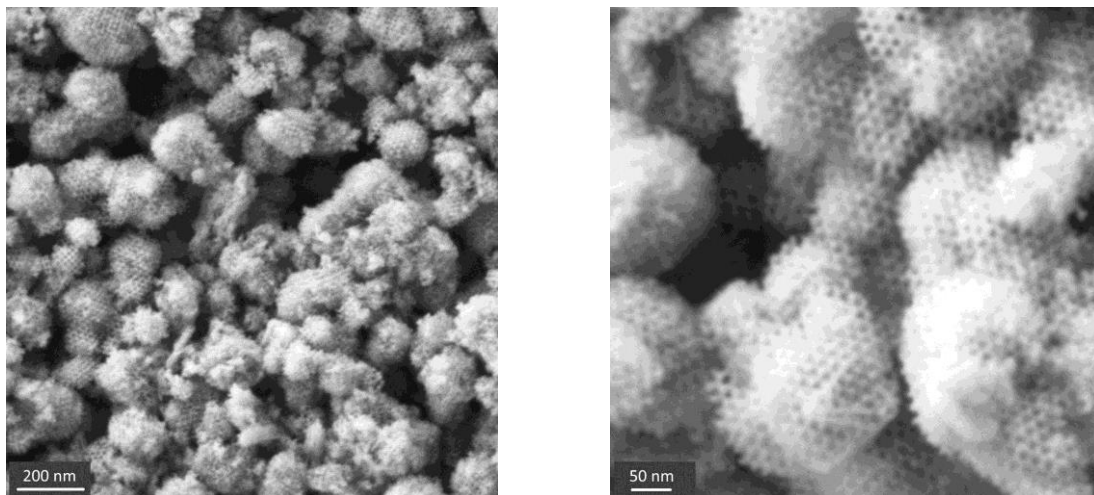
**Figure 48.** Representative SEM images of mesoporous $CoFe_2O_4$ obtained by nanocasting from KIT-6, synthesized at 80 °C. (Images were recorded on ZEISS NEON® 40 with CrossBeam®.)

All structural data of the mesoporous $CoFe_2O_4$ replica compared to those of the parental silica matrix obtained from powder X-ray diffraction analysis and $N_2$ physisorption measurements are listed in Table 14.

**Table 14.** Structural parameters from P-XRD and $N_2$ physisorption of $CoFe_2O_4$ obtained from KIT-6, synthesized at 80 °C.

| | $d_{211}$/ nm | average pore diameter [a] / nm | average pore wall thickness / nm | specific BET surface area / $m^2g^{-1}$ | specific pore volume / $cm^3g^{-1}$ | crystallite size [b] / nm |
|---|---|---|---|---|---|---|
| (KIT-6 80 °C) | 8.4 | 7.0 | 3.3 | 733 (213) [c] | 0.88 (0.1) [c] | - |
| $CoFe_2O_4$ replica | 8.8 | 4.9 | 5.9 | 160 (-) [c] | 0.38 (-) [c] | 11 |

[a] average pore diameter was determined by NLDFT data-based evaluation; [b] crystallite size was evaluated according to the SCHERRER equation; [c] micropore area and micropore volume determined by $t$-plot method according to BROEKHOFF and DE BOER

## 4.3.2 Nanostructure-Related Magnetic Properties

### 4.3.2.1 Impact of the Nanostructure on the Magnetic Behavior

Similar to the binary cobalt oxide system, the magnetic behavior of mesoporous $CoFe_2O_4$ was analyzed. In contrast to the before-described $Co_3O_4$ with antiferromagnetic and weak ferromagnetic properties, bulk-phase $CoFe_2O_4$ is a ferrimagnetic material.[147] To investigate the influence of the nanostructural parameters on the magnetic behavior, analogous to the

above-described study of mesoporous $Co_3O_4$, two mesoporous $CoFe_2O_4$ samples were prepared, different with respect to their structural properties, such as surface areas and crystallite sizes (see Table 14 and Table 15). The various $CoFe_2O_4$ samples were obtained by structure replication from two different KIT-6 silica matrices synthesized at 80 °C and 140 °C; this has been described in detail in former sections (see 4.2.4.2). The two different samples are denoted as '$CoFe_2O_4$ (utilized structure matrix)', analogous to the description of the $Co_3O_4$ samples (see 4.2.1).

Figure 49 (left) shows the field-dependent magnetization curves, measured at 10 K, of the respective mesoporous cobalt ferrite materials as well as a bulk-phase $CoFe_2O_4$ sample for comparison; pronounced and symmetric hysteresis is obtained for all three samples.

The presence of hysteresis further confirms the successful synthesis of the ternary cobalt oxide. If, instead, substantial amounts of by-phases had formed, then these would have affected the magnetic behavior, as is shown in Figure 49 (right). This curve depicts the magnetization of a sample with significant contribution of non-ferrimagnetic phase(s), which becomes apparent from a weaker hysteresis and particularly from the absence of saturation. Most likely the by-product is the binary cobalt oxide ($Co_3O_4$) which is difficult to distinguish from $CoFe_2O_4$ by X-ray diffraction analysis.
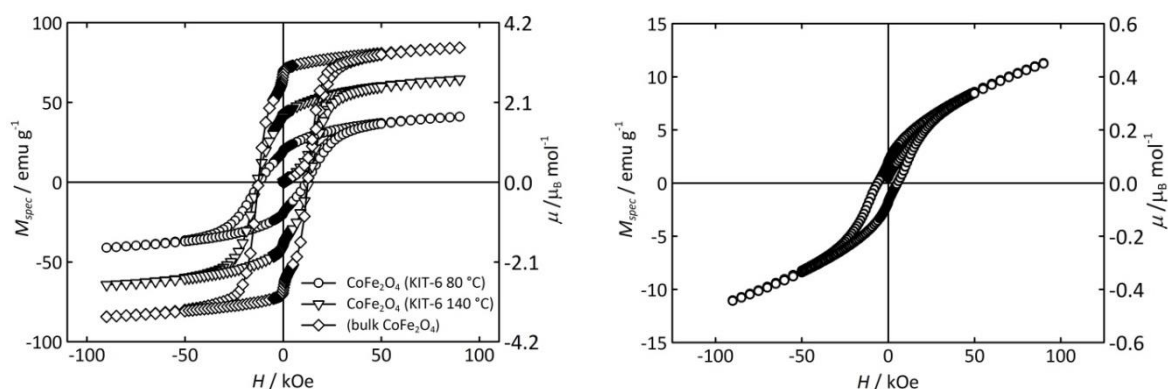


**Figure 49.** Field-dependent magnetization ($T$ = 10 K) of two mesoporous $CoFe_2O_4$ samples replicated from KIT-6 silica matrices, synthesized at 80 °C and 140 °C, respectively, as well as bulk-phase $CoFe_2O_4$ (left); magnetization measurement ($T$ = 10 K) of mesoporous $CoFe_2O_4$ with non-ferrimagnetic impurities (right).

The coercivity fields $H_C$ of the three samples differ only slightly, in the range from *ca.* 12.0 kOe to *ca.* 13.5 kOe for the mesoporous $CoFe_2O_4$ samples replicated from small- and large-pore KIT-6; for the bulk-phase material an intermediate value of *ca.* 12.3 kOe is obtained (see Table 15). Contrary to this, clear differences are observed for the saturation

magnetization $M_S$ and the remanence $M_R$ (see Table 15). The saturation magnetization values $M_S$ were determined by a linear fit of $M$ vs. $1/H$ in the high-field regions (+ 50 to + 90 kOe and - 50 to - 90 kOe), extrapolation to $1/H = 0$ (*i.e.* H = ∞), and averaging.[200] The bulk-phase sample exhibits the highest saturation of 3.78 $\mu_B$ mol$^{-1}$ (89.9 emu g$^{-1}$). Based on the antiferromagnetic coupling of the two magnetic sublattices corresponding to $^T(Co^{2+})$ and $^O(Fe^{3+})$ a saturation magnetization of 3 $\mu_B$ mol$^{-1}$ (71.4 emu g$^{-1}$) is expected, while T and O represent the tetrahedral and octahedral sites, respectively; slightly larger values for saturation magnetization are explained by assuming an incomplete inverse spinel structure for $CoFe_2O_4$.[201] Comparing the values for remanence and saturation magnetization of the bulk-phase sample with the mesoporous ones, a clear trend is observed; both values are obviously reduced for the $CoFe_2O_4$ replicated from KIT-6 (140 °C), whereas the $CoFe_2O_4$ sample from KIT-6 (80 °C) exhibit the lowest values (see Table 15). This corresponds to the respective surface-to-volume ratio. With the results from the before-described study on the magnetic behavior of $Co_3O_4$ in mind, it would be desirable to distinguish between solid-gas and solid-solid interfaces, respectively (see 4.2.4.2 and Scheme 5). However such a differentiation is not possible in a straightforward way for the three $CoFe_2O_4$ samples, since both the specific BET surface area (*i.e.* solid-gas interface) and the crystallite size (which is related to the solid-solid interface) clearly increase in the order of bulk $CoFe_2O_4$ < $CoFe_2O_4$ (KIT-6 140 °C) < $CoFe_2O_4$ (KIT-6 80 °C).

**Table 15.** BET surface areas, crystallite sizes and magnetic parameters of the $CoFe_2O_4$ replica materials from KIT-6 synthesized at 80 °C and 140 °C as well as for bulk-phase $CoFe_2O_4$.

|  | specific BET surface area / m$^2$g$^{-1}$ | crystallite size / nm | coercivity / kOe | saturation magnetization / $\mu_B$ mol$^{-1}$ | remanence / $\mu_B$ mol$^{-1}$ |
|---|---|---|---|---|---|
| $CoFe_2O_4$ (KIT-6 80°C) | 161 | 9 | 12.0 | 1.94 | 0.82 |
| $CoFe_2O_4$ (KIT-6 140°C) | 112 | 12 | 13.5 | 2.92 | 1.73 |
| (bulk $CoFe_2O_4$) | < 50 | 27 | 12.3 | 3.78 | 2.85 |

The pronounced correlation between magnetic behavior and surface-to-volume ratio can again be attributed to disruption of magnetic ordering in the surface-near regions. For $CoFe_2O_4$ the reduced magnetic ordering results in lower saturation magnetization. This effect

cannot be explained in a straightforward way since for a certain ion at the surface (*e.g.* $Fe^{3+}$) both the ferromagnetically arranged moment (spin of another $Fe^{3+}$-ion) and the antiferromagnetically arranged moment (spin of a $Co^{2+}$-ion) are missing. Indeed, it is not the lack but rather the orientation of magnetic moments near the surface that affects the magnetization. A non-collinear spin orientation near the surface of $CoFe_2O_4$ particles was reported in the literature.[202] This spin-canting causes a progressive reduction of the saturation magnetization with increasing specific surface area.

In summary, in a similar study as described for $Co_3O_4$ the impact of nanostructural parameters on the magnetic behavior was also investigated for $CoFe_2O_4$. An increasing distortion of the magnetic ordering near the surface with decreasing crystallite sizes and larger BET surface areas leads to distinct modifications of the magnetic properties. Here, this distortion leads to a reduced magnetic moment, while an enhancement of the magnetic moments has been observed for $Co_3O_4$; this depends on the characteristics of the magnetic sublattices.

The structural data obtained from powder X-ray diffraction analysis and $N_2$ physisorption measurements of the two different mesoporous $CoFe_2O_4$ samples which were replicated from KIT-6 synthesized at 80 °C and 140 °C are listed in Table 16; the table also includes the data of the utilized KIT-6 matrices.

**Table 16.** Structural parameters from P-XRD and $N_2$ physisorption of $CoFe_2O_4$ obtained from different KIT-6, synthesized at 80 °C and 140 °C, respectively.

| | $d_{211}$/ nm | average pore diameter [a] / nm | average pore wall thickness / nm | specific BET surface area / $m^2g^{-1}$ | specific pore volume / $cm^3g^{-1}$ | crystallite size [b] / nm |
|---|---|---|---|---|---|---|
| KIT-6 (80 °C) | 8.6 | 6.8 | 3.1 | 608 | 0.73 | - |
| $CoFe_2O_4$ replica | [c] | 6.1 | [c] | 161 | 0.39 | 9 |
| KIT-6 (140 °C) | 10.0 | 10.5 | 1.7 | 447 | 1.32 | - |
| $CoFe_2O_4$ replica | [c] | 4.9 | [c] | 112 | 0.31 | 12 |

[a] average pore diameter was determined by NLDFT data-based evaluation; [b] crystallite size was evaluated according to the SCHERRER equation; [c] low-angle peak to weak resolved

### 4.3.3  Mesostructured CoFe$_2$O$_4$/BaTiO$_3$ Composite Material

As already described in the introductory section (see 1.3) multiferroics are increasingly of interest in current research. However the synthesis of such materials combining at least two types of ferroic ordering with an enhanced coupling between their dual ferroic order parameter poses a major challenge. In the following one approach for preparing a composite material with both ferrimagnetic and ferroelectric properties is presented; combining both phases with a nanometer-sized structuring associated with a large contact area seems to be a promising system for a multiferroic material with strong coupling.

The composite was obtained in a two-step synthesis; first cobalt ferrite (CoFe$_2$O$_4$) with ferrimagnetic properties was prepared according to the before-described procedure by structure replication (see 3.2.2 and 4.3.1). Then in a second step barium titanate (BaTiO$_3$) as one of the prominent perovskite-type materials with ferroelectric properties (see 1.2.4) was created inside the pores of the CoFe$_2$O$_4$ phase. This was accomplished by combining a matrix-assisted synthesis with the citrate route[203-205] to obtain the ternary metal oxide with the desired stoichiometry (see 3.2.3).

The synthesis concept employed for obtaining the mesostructured CoFe$_2$O$_4$/BaTiO$_3$ composite material is visualized in Scheme 6.
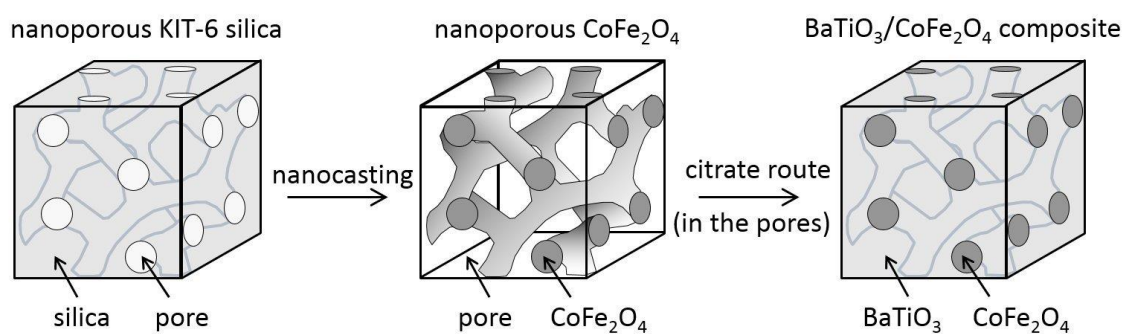


**Scheme 6.** Scheme to illustrate the synthesis approach for a mesostructured CoFe$_2$O$_4$/BaTiO$_3$ composite material.

### 4.3.3.1 Structural Characterization of the $CoFe_2O_4/BaTiO_3$ Composite

The resulting composite material obtained by the above-described synthesis approach is characterized by powder X-ray diffraction analysis, transmission electron microscopy and nitrogen physisorption analysis. Figure 50 shows the resulting X-ray diffraction patterns for the $CoFe_2O_4/BaTiO_3$ composite compared to mesoporous $CoFe_2O_4$ matrix. The low-angle diffraction patterns (left) show that the characteristic signature that is obtained for mesoporous $CoFe_2O_4$ is significantly weaker for the composite material. This reduced intensity indicates that the pores of $CoFe_2O_4$ are filled with $BaTiO_3$ to a large extent; the pore filling results in a reduced scattering contrast between the $CoFe_2O_4$ pore walls and the pore.

The corresponding wide-angle diffraction patterns of the composite and of the $CoFe_2O_4$ matrix (right) further confirm the occurrence of both phases in the composite sample. All peaks observed for the pure $CoFe_2O_4$ (*) that can be assigned to the cubic spinel phase are also obtained for the composite sample, whereas additional reflections are visible all of which are assignable to the perovskite phase of $BaTiO_3$ ($\downarrow$).
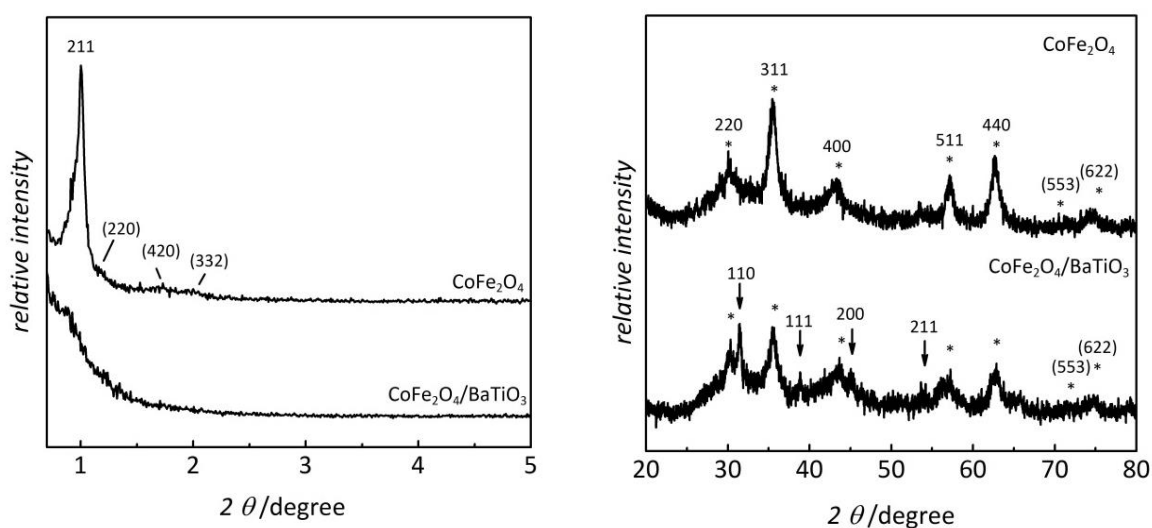


**Figure 50.** Low- and wide-angle X-ray diffraction patterns of a $CoFe_2O_4/BaTiO_3$ composite material compared to mesoporous $CoFe_2O_4$ alone. For reasons of clarity the diffractograms are vertically shifted.

Successful pore filling of the mesoporous $CoFe_2O_4$ is also corroborated by the results obtained from nitrogen physisorption analysis. Figure 51 (left) shows the physisorption isotherms for the $CoFe_2O_4/BaTiO_3$ composite material compared to the mesoporous $CoFe_2O_4$ matrix. The type-IV behavior with a weak hysteresis observed for the pure $CoFe_2O_4$ indicating uniform mesopores is much less pronounced for the composite material. The BET

surface area and the pore volume are decreased from 160 $m^2g^{-1}$ and 0.38 $cm^3g^{-1}$ to 36 $m^2g^{-1}$ and 0.14 $cm^3g^{-1}$, respectively.
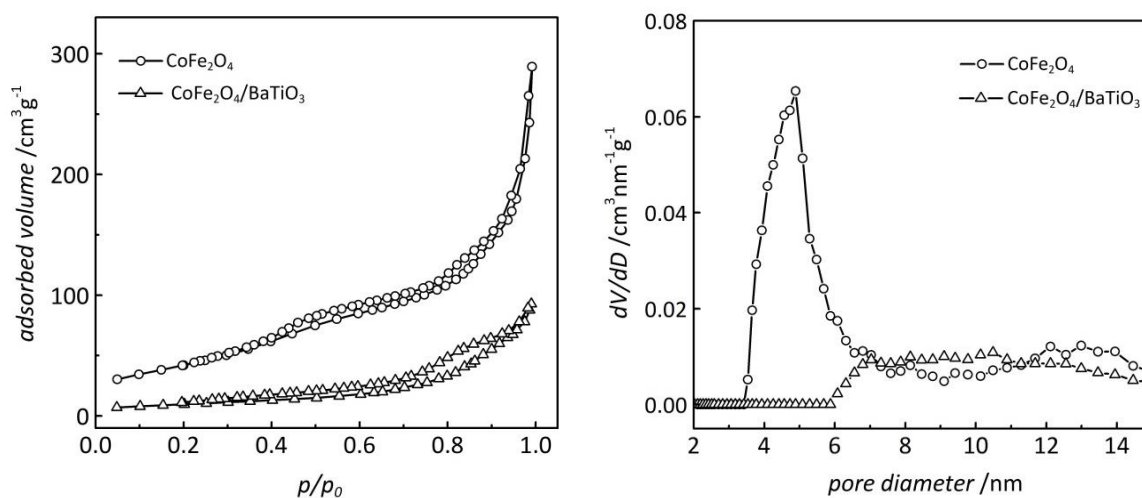


**Figure 51.** Nitrogen physisorption isotherms (left) and corresponding pore size distributions obtained by NLDFT data-based evaluation (right) of the $CoFe_2O_4/BaTiO_3$ composite and of mesoporous $CoFe_2O_4$ matrix.

The corresponding pore size distribution determined by NLDFT (right) reveals a pronounced peak at 4.9 nm for the mesoporous $CoFe_2O_4$ which is no longer observed for the composite material suggesting that the mesopores of the cobalt ferrite phase are more or less entirely filled with the barium titanate phase.

Additionally, transmission electron microscopy analysis was carried out to investigate the pore filling and particularly the resulting influence of the $BaTiO_3$ incorporation on the mesoscopic structural order. Figure 52 shows representative TEM images of the $CoFe_2O_4/BaTiO_3$ composite material (left) and, for comparison, the pure mesoporous $CoFe_2O_4$ phase (right). The regular well-ordered pore system over large distances for the mesoporous $CoFe_2O_4$ sample cannot be observed in the composite, indicating a pore filling to a substantial degree. However, some fractions of the pores, particularly at the outer regions of the porous particles, are still unfilled; this is consistent with the residual pore volume of 0.14 $cm^3g^{-1}$ as mentioned above.

The relative amounts of the two phases, *i.e.* $CoFe_2O_4$ and $BaTiO_3$, in the composite material were quantitatively determined by photometric analysis of iron to a molar ratio of $BaTiO_3$:$CoFe_2O_4$ = 0.48:0.52, assuming the absence of any phases other than $CoFe_2O_4$ or $BaTiO_3$. Thus both phases are almost equimolar in the composite, although this ratio slightly

differs from the theoretical value that has been derived from the relative amounts of Ba and Ti precursors used per weighed amount of $CoFe_2O_4$ ($BaTiO_3$:$CoFe_2O_4$ = 0.38:0.62). This deviation, *i.e.* the larger quantity of $CoFe_2O_4$ for the theoretical value, may be attributed to physisorbed water or other impurities which may have been contained in the porous $CoFe_2O_4$ sample.
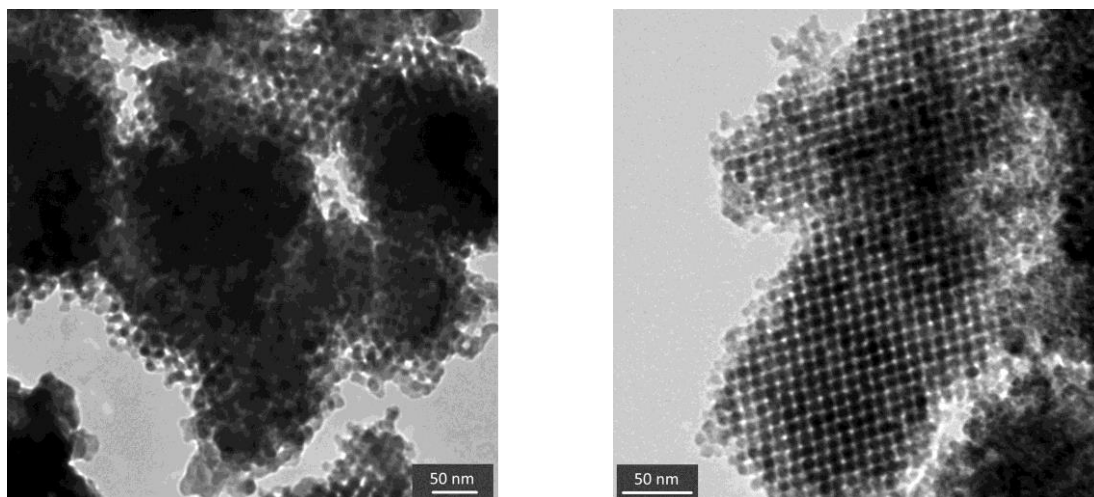


**Figure 52.** Representative TEM images of the $CoFe_2O_4$/$BaTiO_3$ composite (left) compared to mesoporous $CoFe_2O_4$ (right) alone.

The structural parameters obtained from powder X-ray diffraction analysis and $N_2$ physisorption measurements of the mesoporous $CoFe_2O_4$ matrix as well as those of the resulting $CoFe_2O_4$/$BaTiO_3$ composite are listed in Table 17.

**Table 17.** Structural parameters from P-XRD and $N_2$ physisorption of mesoporous $CoFe_2O_4$ and the resulting $CoFe_2O_4$/$BaTiO_3$ composite material.

| | $d_{211}$ / nm | average pore diameter [a] / nm | average pore wall thickness / nm | specific BET surface area / $m^2g^{-1}$ | specific pore volume / $cm^3g^{-1}$ | crystallite size [b] / nm |
|---|---|---|---|---|---|---|
| $CoFe_2O_4$ | 8.8 | 4.9 | 5.9 | 160 | 0.38 | 11 |
| $CoFe_2O_4$/ $BaTiO_3$ | - | - | - | 38 | 0.14 | - |

[a] average pore diameter was determined by NLDFT data-based evaluation; [b] crystallite size was evaluated according to the SCHERRER equation

## 4.3.3.2  Magnetic Behavior of the CoFe$_2$O$_4$/BaTiO$_3$ Composite

Since the mesostructured composite of CoFe$_2$O$_4$ as a ferrimagnetic material and BaTiO$_3$ with ferroelectric properties is promising for multiferroics, the ferroic properties need to be investigated. Thus first measurements of the magnetic behavior were carried out.

Figure 53 shows the field-dependent magnetization of the CoFe$_2$O$_4$/BaTiO$_3$ composite material compared to the pure CoFe$_2$O$_4$ measured at 10 K. In case of the composite the magnetization is normalized with respect to the amount of CoFe$_2$O$_4$ based on the above-mentioned quantitative composition (see 4.3.3.1).
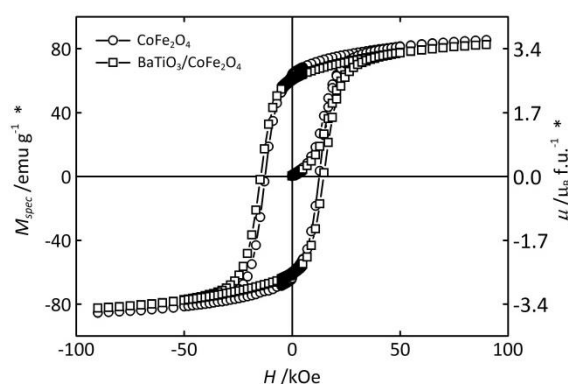


**Figure 53.** Field-dependent magnetization ($T$ = 10 K) of the CoFe$_2$O$_4$/BaTiO$_3$ composite material compared to mesoporous CoFe$_2$O$_4$ alone. The specific magnetization is normalized to the amount of CoFe$_2$O$_4$ in case of the composite (*).

Both materials reveal almost identical magnetization curves; hysteresis with coercivities $H_c$ of 14.3 kOe, saturation magnetization $M_s$ of 3.44 $\mu_B$ mol$^{-1}$ and a remanence $M_R$ of 2.52 $\mu_B$ mol$^{-1}$ are obtained for the composite (see Table 18). The coercivity field is slightly larger for the composite compared to the pure CoFe$_2$O$_4$, while the other two values differ only slightly from each other. By comparing these values with those discussed in the previous section (see 4.3.2.1) the coercivity is in good accordance with that obtained for the above described CoFe$_2$O$_4$ sample (11.9 kOe vs. 12.0 kOe), whereas the deviation in saturation magnetization and remanence for the mesoporous CoFe$_2$O$_4$ samples is more pronounced (see Table 15). Both values are still lower than those measured for the bulk-phase sample, so that these findings are consistent with the before presented study.

**Table 18.** Magnetic parameters of the pure mesoporous $CoFe_2O_4$ and of the resulting $CoFe_2O_4/BaTiO_3$ composite material.

|  | coercivity / kOe | saturation magnetization / $\mu_B$ f.u.$^{-1}$ | remanence / $\mu_B$ f.u.$^{-1}$ |
|---|---|---|---|
| $CoFe_2O_4$ | 11.9 | 3.53 | 2.64 |
| $CoFe_2O_4/BaTiO_3$ | 14.3 | 3.44 | 2.52 |

To sum up, the synthesis of a mesostructured composite material of $CoFe_2O_4/BaTiO_3$ was shown to be successful with an approximately equimolar ratio of both components. First measurements show that the magnetic behavior of the ferrimagnetic $CoFe_2O_4$ remains almost unaffected by the incorporation of the ferrielectric phase; however this has to be investigated in more details. Furthermore, the composite material has to be examined with respect to the ferroelectric behavior and, particularly, potential coupling between the two phases need to be focused in further studies.

## 4.4   Mesoporous Aluminum Oxide

### 4.4.1   Structural Characterization of Mesoporous Aluminum Oxide

Mesoporous aluminum oxide ($Al_2O_3$) was also synthesized by structure replication. However, in this case, contrary to the before-described metal oxides, mesoporous carbon was utilized as structural mold instead of silica, since aluminum oxide is not resistant against either sodium hydroxide or hydrofluoric acid used for the removal of silica templates. Therefore mesoporous CMK-3 and CMK-8 carbon served as structure matrices, which in turn have been obtained by nanocasting from SBA-15 and KIT-6 in a preceding step. Hence, two consecutive structure replication procedures were carried out for the synthesis of mesoporous aluminum oxide. In the following part the characterization of mesoporous alumina is presented by using CMK-8 carbon as structure matrix, including the characterization of the composite materials as well. Since this synthesis procedure, which involves several impregnation steps, is rather elaborate, a varied synthesis approach was employed. For infiltration of the precursor in the pores of the carbon matrix (CMK-3 and CMK-8) a melt of aluminum nitrate

was applied instead of a saturated solution, resulting in only one impregnation step required. In the following the samples are analogously termed as described for $Co_3O_4$ (see 4.2.1), *i.e.* '$Al_2O_3$ (respective structure matrix)'.

### 4.4.1.1  Impregnation with a Precursor Solution

To start with the synthesis of mesoporous aluminum oxide by impregnation with a precursor solution ($Al(NO_3)_3$ in THF) and CMK-8 as structure matrix (see 3.2.4), initially the characterization of the CMK-8/$Al_2O_3$ composite materials by powder X-ray diffraction and nitrogen physisorption is shown. The respective composite materials are termed 'number of cycles'; for example '2 cycles' means the CMK-8/$Al_2O_3$ composite material after two consecutive impregnation/oxide formation cycles.

Figure 54 depicts the X-ray diffraction patterns of both the CMK-8 carbon matrix and the resultant CMK-8/$Al_2O_3$ composite materials after each impregnation/oxide formation cycle. The low-angle diffraction patterns (left) show the characteristics of mesoporous cubic CMK-8 carbon with the intense 211 and 220 reflections; for the CMK-8/$Al_2O_3$ composite materials the patterns are less pronounced and only one reflection is observed while the intensity is decreased with increasing number of impregnation/oxide formation cycles. After four cycles only a very weak shoulder is obtained; this indicates a successful pore filling due to a reduced scattering contrast between the pore walls and the filled pores. The *d*-values are almost constant for all samples (see Table 19) suggesting that the structure replication has been occurred without significant change in the size of the unit cell.

The wide-angle diffraction patterns (right) of the CMK-8/ $Al_2O_3$ composite materials show for all samples the two most intense reflections of aluminum oxide in the gamma modification ($\gamma$-$Al_2O_3$; JCPDS 75-0921) with the intensity of the 440 peak substantially increasing upon each cycle of impregnation/oxide formation. This indicates that the crystallites grow with additional impregnation/oxide formation cycles.
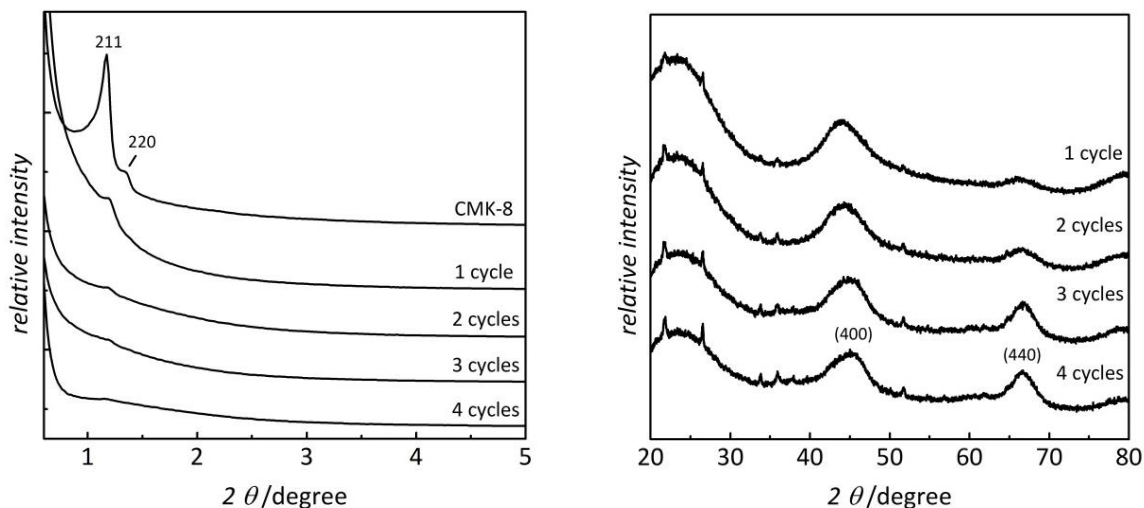
**Figure 54.** Low- and wide angle X-ray diffraction patterns of CMK-8/Al$_2$O$_3$ composite materials before and after consecutive impregnation/oxide formation cycles. For reasons of clarity the diffractograms are vertically shifted. (Measurements were carried out on a PANanalytical X'Pert Pro diffractometer.)

The nitrogen physisorption isotherms (left) and the corresponding pore size distribution plots (right) as depicted in Figure 55 further confirm the successive pore filling with increasing number of impregnation/oxide formation cycles. The adsorbed volume of nitrogen in the isotherms is reduced from cycle to cycle and so is the area below the pore size distribution which corresponds to the pore volume.
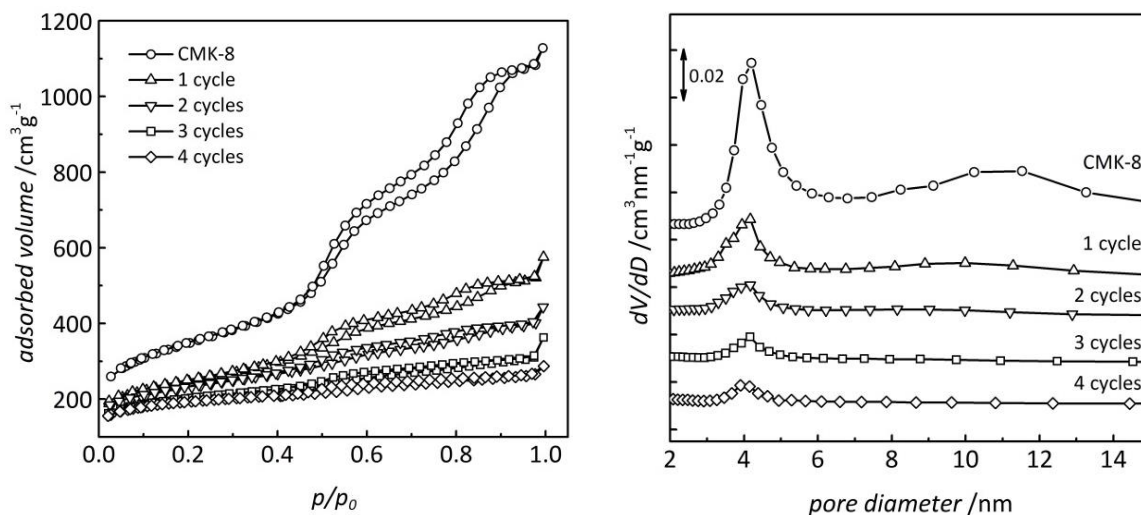


**Figure 55.** Nitrogen physisorption isotherms (left) and corresponding BJH-pore size distributions (right) of the same samples as in Figure 54. For reasons of clarity the pore size distributions are vertically shifted.

The pore size remains almost constant for each impregnation/oxide formation cycles (see Table 19); the same trend was already observed for the silica/$Co_3O_4$ composite materials described in 4.2.2. However, in contrast to the before described samples, here, the pore size distributions were obtained by applying the BJH method; pore size determination by NLDFT data-based evaluation was prohibitive for aluminum oxide due to lack of an appropriate data kernel. Keeping in mind that evaluation of the pore diameter by using the BJH method underestimates the real pore size to an ill-defined extent, the corresponding pore wall thicknesses were not calculated for the $Al_2O_3$ samples.

Removal of the carbon matrix by combustion yields mesoporous $Al_2O_3$. Figure 56 shows the results of the powder X-ray diffraction measurements of the carbon-free $Al_2O_3$ replica material. The low-angle diffraction pattern (left) exhibits one broad reflection, less resolved and of lower intensity compared to the original CMK-8 carbon matrix (see Figure 54, left). This indicates a lower degree in mesostructural order. Such structural loss is frequently observed in structure replication, especially when more than one replication steps are necessary, including the preparation of the carbon matrix in a previous step as in case of the here described synthesis of $Al_2O_3$ or MgO for instance.[119] Comparison of the *d*-value of the replica with that of the utilized carbon matrix shows that the lattice planes are different (Table 19) which is attributable to the quality of the resultant carbon-free sample consisting of weakly ordered and non-ordered domains (see Figure 57).
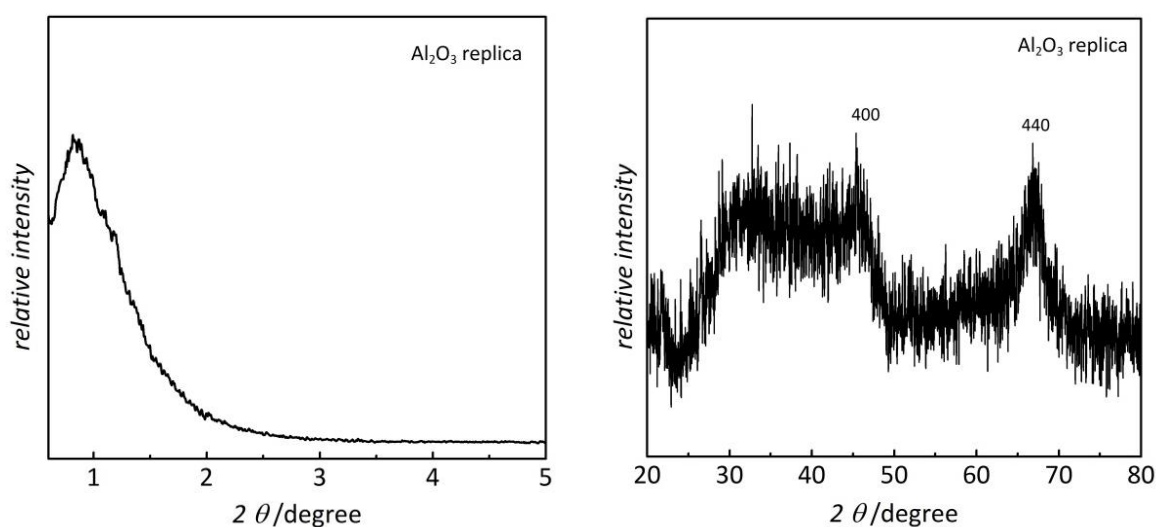


**Figure 56.** Low- and wide-angle X-ray diffraction patterns of the resultant carbon-free mesoporous $Al_2O_3$ replicated from cubic CMK-8 carbon.

The corresponding wide-angle P-XRD pattern (right) shows two reflections indexable for 400 and 440 of $\gamma$-$Al_2O_3$ (JCPDS 75-0921); only a low degree of crystallinity is obtained. Applying the SCHERRER equation (5) to the 440 peak a crystallites with a size of about 6 nm are yielded.

The lower degree in mesostructural order as it was observed in the low-angle XRD pattern is confirmed by transmission electron microscopy (Figure 57, left), whereas larger domains of an ordered pore system are also obtained in fractions of the same sample (right). This may be the result of an inhomogeneous precipitation of $Al(OH)_3$/$AlOOH$ as it was described in the experimental section (3.2.4). The regions of the sample that were close to the vapor interface may be better ordered than other parts without or with only weak contact area to the ammonia vapor. However, this impact of ammonia vapor treatment on the mesoscopic order will be focused in the following section (4.4.2.2). The inset shows the results of selected area electron diffraction (SAED); a concentric diffraction ring pattern is obtained indicating the presence of a polycrystalline material. This is consistent with the wide-angle diffraction pattern and in good accordance with results from LIU et al.[117] Energy-dispersive X-ray diffraction (EDX) analysis, carried out at 5 different spots, suggests a silica amount of less than 1 %.
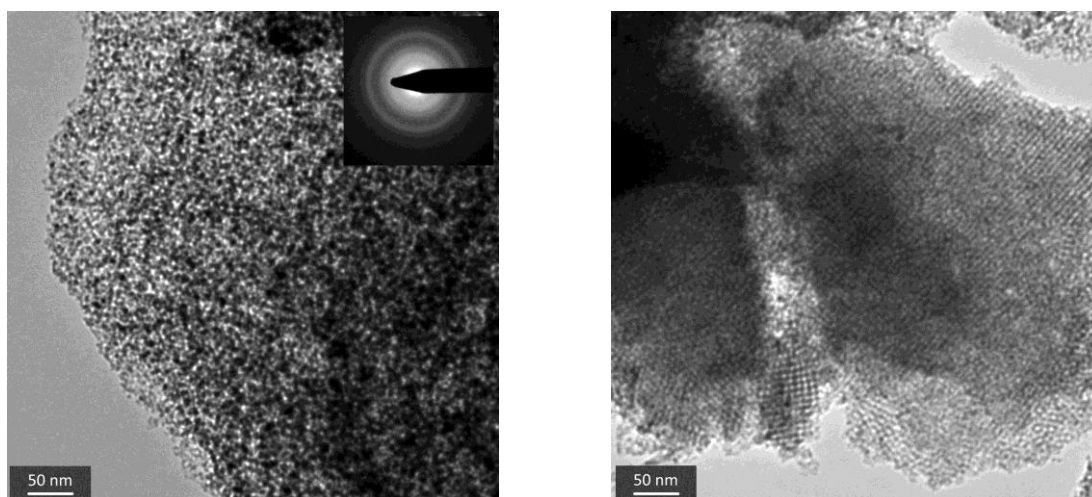


**Figure 57.** Representative TEM images of the same sample as in Figure 56. Inset shows the corresponding SAED pattern.

Figure 58 displays the results of nitrogen physisorption analysis; the isotherms (left) exhibit a type-IV shape with hysteresis indicating the presence of regular mesopores. The specific surface area is determined to 261 $m^2g^{-1}$ and the total pore volume to 0.69 $cm^3g^{-1}$. These values are significantly lower than that of the respective carbon structure matrix. This was already discussed for mesoporous $Co_3O_4$ before; here again, particularly the different

densities have to be accounted for, which is 3.97 g cm$^{-3}$ for $Al_2O_3$,[193] approximately twice as much as the carbon density ($\rho_{carbon}$ = 2.1 g cm$^{-3}$). Furthermore the contribution of microporosity has to be considered, similar as for $Co_3O_4$; for mesoporous carbon utilized as structure matrix a substantial amount of microporosity is obtained; this contribution of micropores determined by BROEKHOFF and DE BOER[184] are included in Table 19. Also, different surface roughness has to be mentioned again as a potential factor affecting the specific surface area which is for crystalline materials lower than for amorphous materials like silica or carbon.
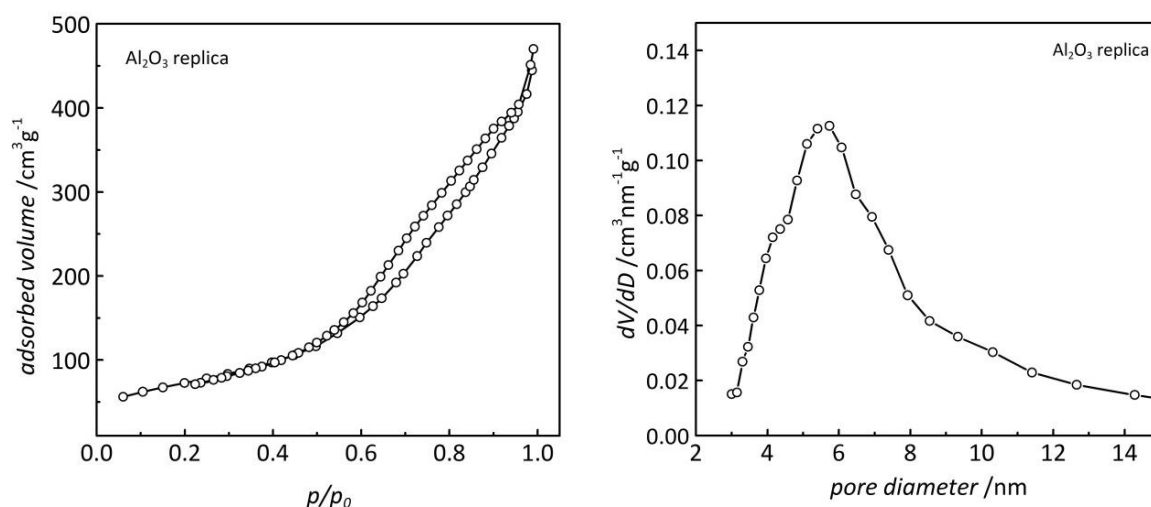


**Figure 58.** Nitrogen physisorption isotherm (left) and corresponding BJH-pore size distribution of the same samples as in Figure 56.

The respective pore size distribution obtained by BJH method shows a broad peak, consistent with the low degree in mesostructural order as it was already concluded from the low-angle X-ray diffraction pattern (Figure 56); the maximum of the pore size distribution is 5.7 nm. Since the BJH method has been applied due to lack of an appropriate kernel for a NLDFT data-based evaluation, a relation between the pore size of the structure matrix and the pore wall of the replica and vice versa was not reasonable.

All structural data obtained from powder X-ray diffraction analysis and $N_2$ physisorption measurements of the utilized CMK-8 carbon matrix, the CMK-8/$Al_2O_3$ composite materials after each impregnation/ oxide formation cycle and of the resultant carbon-free $Al_2O_3$ replica material are listed in Table 19.

**Table 19**. Structural parameters from P-XRD and $N_2$ physisorption of the CMK-8/$Al_2O_3$ composites and of the resulting carbon-free $Al_2O_3$ replica material.

| | $d_{211}$ / nm | average pore diameter [b] / nm | specific BET surface area / $m^2g^{-1}$ | specific pore volume / $cm^3g^{-1}$ | crystallite size [c] / nm |
|---|---|---|---|---|---|
| CMK-8 | 7.5 | 4.2 | 1180 (261) [c] | 1.68 (0.13) [c] | - |
| 1 cycle | 7.4 | 4.2 | 824 | 0.81 | 3 |
| 2 cycles | 7.5 | 4.2 | 764 | 0.63 | 3 |
| 3 cycles | - [a] | 4.2 | 649 | 0.49 | 4 |
| 4 cycles | - [a] | 3.9 | 613 | 0.41 | 4 |
| $Al_2O_3$ replica | 10.5 | 5.7 | 261 (-) [c] | 0.69 (-) [c] | 6 |

[a] low-angle XRD peak to weakly resolved; [b] average pore diameter was determined by BJH method; [c] crystallite size was evaluated according to the SCHERRER equation; [c] micropore area and micropore volume determined by $t$-plot method according to BROEKHOFF and DE BOER

## 4.4.1.2  Impregnation with a Precursor Melt

With respect to the results of the previous section, it needs to be stressed that for the above-described synthesis several impregnation cycles are required. Therefore another synthesis approach was employed for preparing mesoporous aluminum oxide (see 3.2.4). A melt of aluminum nitrate was utilized as precursor instead of an aqueous solution, resulting in only one single impregnation/oxide formation cycle being required (instead of four). In the following the aluminum oxide samples are termed '$Al_2O_3$ (respective structure matrix)'; for example '$Al_2O_3$ (CMK-3)' means that CMK-3 was applied as structure matrix for the respective $Al_2O_3$ sample.

Figure 59 shows the results of X-ray diffraction analysis of two thus-synthesized mesoporous $Al_2O_3$ samples using both CMK-3 and CMK-8 as structure matrices. The low-angle diffraction patterns (left) show one broad reflection for both samples, similar to the XRD pattern described above for the $Al_2O_3$ using a solution for impregnation; however the peak is substantially more pronounced for the replica from CMK-8. Again, the reflections are weaker

than those of the utilized carbon matrices (see also 4.1.2) indicating a lower degree of mesostructural order, a result of the structure replication procedure as already described before.

The corresponding wide-angle diffraction patterns (right) show that both materials are crystalline and the reflections are indexable for the most intense 400 and 440 reflections of γ-Al$_2$O$_3$, however with only low degree of crystallinity; applying the SCHERRER equation (5) to the same peak yields crystallites of about 5 nm, similar to the results before.
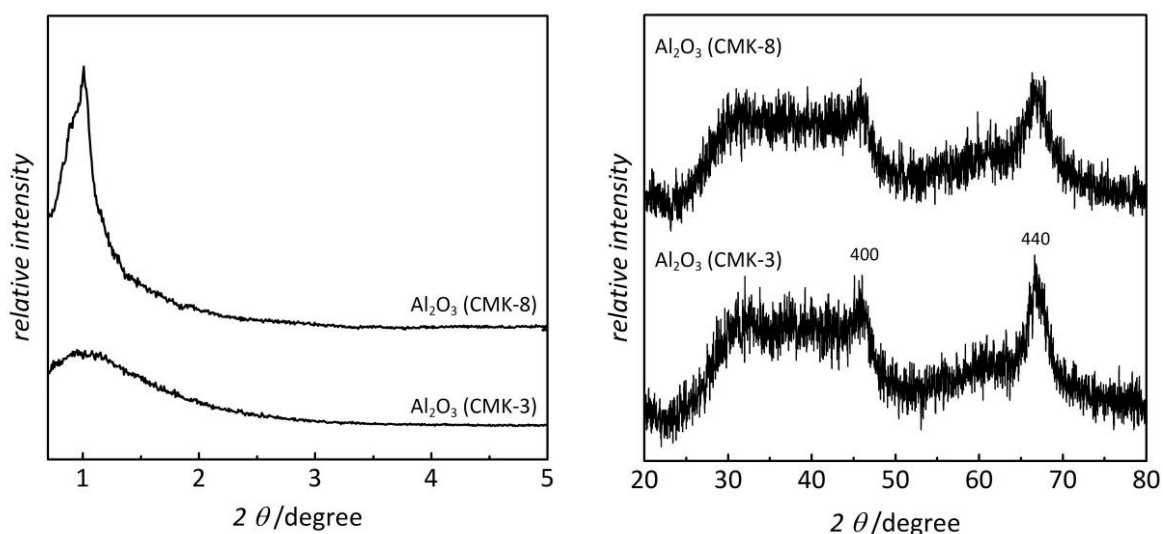


**Figure 59.** Low- and wide-angle X-ray diffraction patterns of mesoporous Al$_2$O$_3$ replicated from mesoporous CMK-3 and CMK-8 carbon with aluminum nitrate in the molten state as precursor. For reasons of clarity the diffractograms are vertically shifted.

The structural order was further analyzed by transmission electron microscopy. Figure 60 (left) shows a representative TEM image of mesoporous Al$_2$O$_3$ replicated from CMK-3; only a low degree of mesostructural order is observed, while the ordered domains are significantly larger for the Al$_2$O$_3$ sample replicated from CMK-8 (right). The more pronounced ordered pore system in case of the latter sample was already reflected in the low-angle X-ray diffraction patterns by the more intense reflection for the Al$_2$O$_3$ replicated from CMK-8. This might be a result of the different pore systems being present in the two mesoporous carbons, similar to the situation of replication from SBA-15 and KIT-6 with different pore interconnectivity as it has been described in more details before (see 4.1.1). The insets show the corresponding SAED patterns; the concentric diffraction rings with additional spots indicate to some degree the presence of small single-crystalline domains in

addition to the otherwise polycrystalline nature of the material; this corroborates the results obtained from wide-angle X-ray diffraction patterns (see Figure 59).
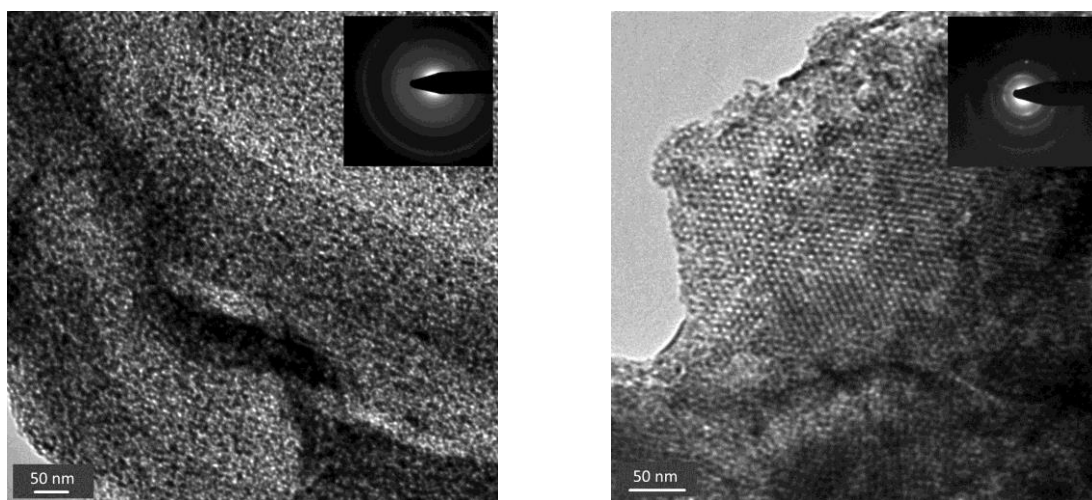


**Figure 60.** Representative TEM images of the mesoporous $Al_2O_3$ samples replicated from hexagonal CMK-3 (left) and cubic CMK-8 (right), respectively. Insets show the corresponding SAED patterns.

These findings are consistent with the results from nitrogen physisorption analysis (Figure 61). The isotherms (left) also show type-IV shape with a hysteresis indicating the presence of regular mesopores as it was obtained for the previously described $Al_2O_3$ sample. The corresponding BJH pore size distributions (right) exhibit broad peaks, corroborating the lower mesostructural order as observed by the low-angle XRD patterns (see Figure 59). The pore diameters of the $Al_2O_3$ replica from CMK-3 and CMK-8 are slightly different from each other, but this stands to reason taking into account the structural parameters of the respective carbon structure matrices; those are also different from each other with respect to the pore size and the lattice plane (see Table 20). The resulting BET surface areas are 447 $m^2g^{-1}$ and 303 $m^2g^{-1}$ for the replica from CMK-3 and CMK-8, respectively.

By comparing the surface area of the before-described $Al_2O_3$ replica from CMK-8 by applying a precursor solution with the analog replica obtained by melt impregnation, the latter one exhibits contribution of small fractions of micropores which may be an explanation for the slightly larger specific surface area (see Table 20).
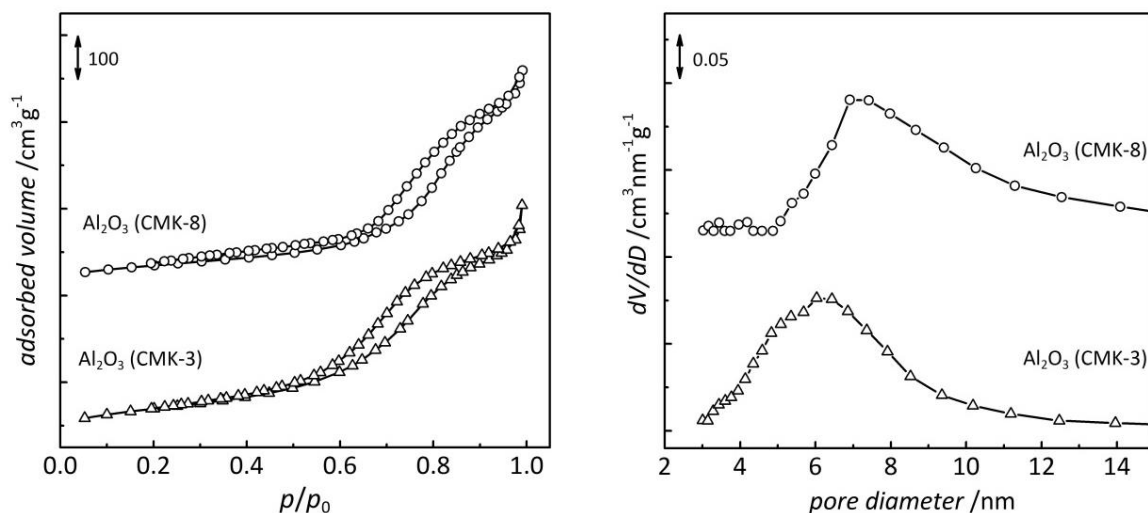
**Figure 61.** Nitrogen physisorption isotherms (left) and corresponding BJH-pore size distributions (right) of the same samples as in Figure 59. For reasons of clarity the isotherms and the pore size distributions are vertically shifted.

In summary, mesoporous $Al_2O_3$ was successfully synthesized by nanocasting using mesoporous carbon phases (CMK-3 and CMK-8) as structure matrices. In addition to impregnation with an aqueous precursor ($Al(NO_3)_3$) solution a melt was employed instead. This modified solvent-free method yields mesoporous $Al_2O_3$ with nanostructural properties comparable to the before-described $Al_2O_3$ sample obtained by impregnation with a solution while only one single impregnation/oxide formation step is required, thus rendering the synthesis more economical and less elaborate.

All structural data obtained from powder X-ray diffraction analysis and $N_2$ physisorption measurements of the mesoporous $Al_2O_3$ samples replicated from CMK-3 and CMK-8 carbon, respectively, are listed in Table 20. The table also includes the data of the respective structure matrices, both the utilized silica molds for the mesoporous carbons as well as the carbon matrices.

**Table 20.** Structural parameters from P-XRD and $N_2$ physisorption of mesoporous $Al_2O_3$ materials replicated from hexagonal CMK-3 and cubic CMK-8 carbon compared to their structure matrices including the SBA-15 and KIT-6 silica materials.

| | $d^{[a]}$ / nm | average pore diameter [b] / nm | specific BET surface area / $m^2g^{-1}$ | specific pore volume / $cm^3g^{-1}$ | crystallite size [c] / nm |
|---|---|---|---|---|---|
| SBA-15 | 9.7 | 8.7 | 616 (76) [c] | 1.39 (0.04) [c] | - |
| CMK-3 | 9.0 | 4.5 | 850 (176) [c] | 1.97 (0.09) [c] | - |
| $Al_2O_3$ replica | 8.9 | 6.0 | 447 (-) [c] | 0.91 (-) [c] | 5 |
| KIT-6 | 9.6 | 9.1 | 724 (104) [c] | 1.68 (0.04) [c] | - |
| CMK-8 | 7.5 | 3.8 | 837 (110) [c] | 1.06 (0.06) [c] | - |
| $Al_2O_3$ replica | 10.6 | 6.9 | 303 (30) [c] | 0.81 (0.02) [c] | 5 |

[a] $d_{100}$ in case of the hexagonal pore system, $d_{211}$ for the cubic pore system; [b] average pore diameter was determined by BJH method; [c] crystallite size was evaluated according to the SCHERRER equation; [c] micropore area and micropore volume determined by $t$-plot method according to BROEKHOFF and DE BOER

## 4.4.2 Relation between Crystallinity and Mesoscopic Order

As already mentioned, the crystallinity frequently plays an important role with respect to various applications such as catalysis. Thus the crystallinity of mesoporous aluminum oxide was investigated in more details. On the one hand the impact of the 'calcination' temperature was considered by varying the temperature accomplished for the oxide formation; on the other hand the ammonia vapor treatment (see 3.2.4) was examined in some details since this step has turned out to be essential for the crystallinity. Additionally, the influence of the crystallinity on the mesoscopic order was analyzed.

### 4.4.2.1 Impact of the Calcination Temperature

First the influence of the calcination temperature (*i.e.* the temperature for the conversion of aluminum hydroxide into aluminum oxide) was investigated. Therefore, the calcination temperature was varied between 500 and 900 °C (see 3.2.4), while the impact on the

crystallinity was analyzed by X-ray diffraction analysis. Figure 62 displays the respective wide-angle XRD pattern of different mesoporous $Al_2O_3$ samples calcined at 500, 700 and 900 °C, respectively. For all samples the patterns exhibit the characteristic reflections of $\gamma$-$Al_2O_3$ as observed for the before-described samples (see Figure 59).
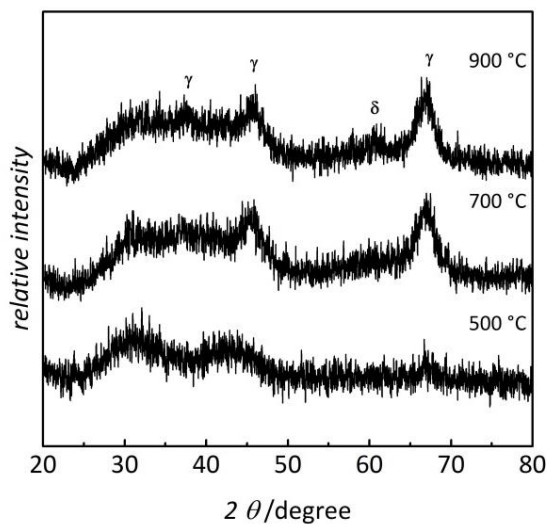


**Figure 62.** Wide-angle X-ray diffraction patterns of mesoporous $Al_2O_3$ with CMK-8 as structure matrix at variable temperatures for calcination (500, 700 and 900 °C). For reasons of clarity the diffractograms are vertically shifted.

The crystallinity is substantially increased with higher temperatures for calcination which becomes obvious by a significant peak narrowing. This difference is particularly pronounced between 500 °C and 700 °C, while the sample calcined at 900 °C seems to contain fractions of $\delta$-$Al_2O_3$, similar as observed by LIU et al.[117] For the samples with a calcination temperature of 700 °C and 900 °C the crystallites are in the region of about 5 nm determined by the SCHERRER equation (5); differences between both samples are within the accuracy of this method. Thus, by increasing the temperature only slight growth of the crystallites is observed while at 900 °C an additional $Al_2O_3$ phase is formed.

## 4.4.2.2 Impact of the Ammonia Vapor Treatment

Since the ammonia vapor exposure (see 3.2.4) has turned out to be crucial for yielding $Al_2O_3$ with a sufficient degree of crystallinity,[117,118,206] the impact of this treatment was studied in some detail. After impregnation of the carbon matrix with the precursor ($Al(NO_3)_3$, either solution or melt), an ammonia vapor treatment is carried out to convert aluminum nitrate into amorphous aluminum hydroxide or -oxyhydroxide ($Al(OH)_3$/AlO(OH)), respectively; this step is referred to as 'precipitation' in the following. The aluminum hydroxide is

subsequently converted into $Al_2O_3$ by thermal treatment at 700 °C. To elucidate the role of the ammonia vapor treatment during the synthesis, the duration of the exposure was varied between 1 and 48 hours (see 3.2.4); additionally a sample without ammonia vapor treatment was prepared. The various thus-obtained $Al_2O_3$ samples were characterized with respect to both crystallinity and their mesoscopic order by powder X-ray diffraction, nitrogen physisorption and transmission electron microscopy.

Figure 63 (left) shows the low-angle P-XRD patterns of the respective $Al_2O_3$ replica samples with different duration of ammonia exposure. The characteristic peak becomes broader and weaker with increasing duration; after 24 hours the peak is entirely vanished. However, without any ammonia vapor treatment the structural order seems to be lower than after 3 to 7 hours of treatment. Thus, the mesoscopic order seems to decrease with longer duration of ammonia exposure while the crystallinity increases.
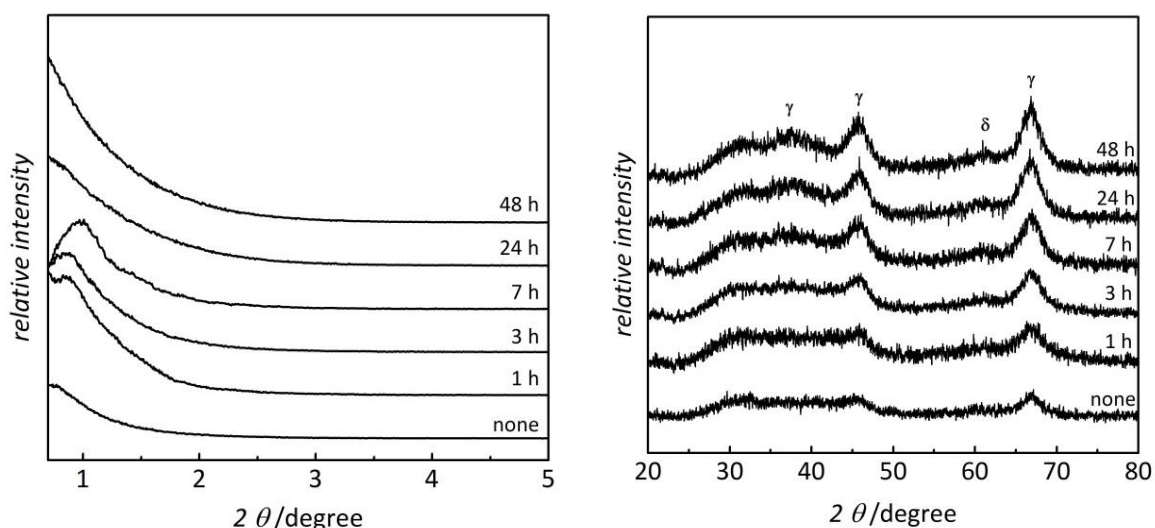


**Figure 63.** Low- and wide-angle X-ray diffraction patterns of various mesoporous $Al_2O_3$ materials with different duration of ammonia vapor treatment. For reasons of clarity the diffractograms are vertically shifted.

Figure 63 (right) shows the corresponding wide-angle diffraction patterns. A clear trend is observed concerning the peak width; the longer the ammonia vapor exposure the narrower the peak becomes. This means, that a longer precipitation time results in a higher degree of crystallinity. Conspicuously, the crystallinity after 1 hour seems to be slightly lower than without ammonia exposure; however the mesoscopic order is higher for the sample with such a treatment as described before. Comparing these results with those obtained by the investigation concerning the influence of calcination temperature on the crystallinity (see

Figure 62) it is concluded that prolonged ammonia treatment increases the crystallinity in almost the same way as higher calcination temperatures (900 °C instead of 700 °C) have affected the crystallinity.

To analyze the impact of the precipitation time on the mesoscopic order Figure 64 shows the nitrogen physisorption isotherms (left) with the corresponding BJH pore size distributions (right). A clear shift in the maxima of the pore size distributions towards larger pore sizes is observed with increasing precipitation time while at the same time the peak width also increases. This means that the longer the precipitation time the less uniform and wider are the pores of the final $Al_2O_3$ material. This is consistent with the results from low-angle X-ray diffraction patterns (Figure 63, left). Thus the ammonia vapor exposure is beneficial for the crystallinity of the final $Al_2O_3$ product; however at the same time the mesoscopic order and porosity suffer from prolonged vapor treatment.
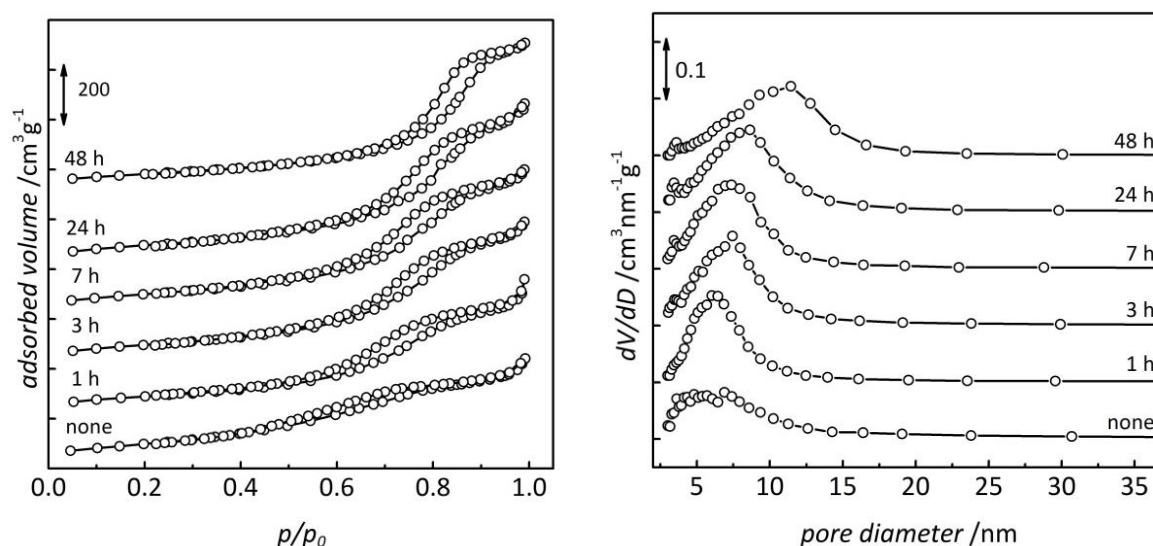


**Figure 64.** Nitrogen physisorption isotherms (left) and corresponding BJH-pore size distributions (right) of various mesoporous $Al_2O_3$ materials with different duration of ammonia vapor treatment. For reasons of clarity the isotherms and pore size distributions are vertically shifted.

Figure 65 shows two representative TEM images of $Al_2O_3$ products without (left) and with an ammonia vapor exposure of 48 hours (right). Both images reflect the results from low-angle X-ray diffraction analysis that on the one hand prolonged ammonia exposure leads to a loss in mesostructural order but on the other hand completely without such an exposure the structural order is just as low as well.
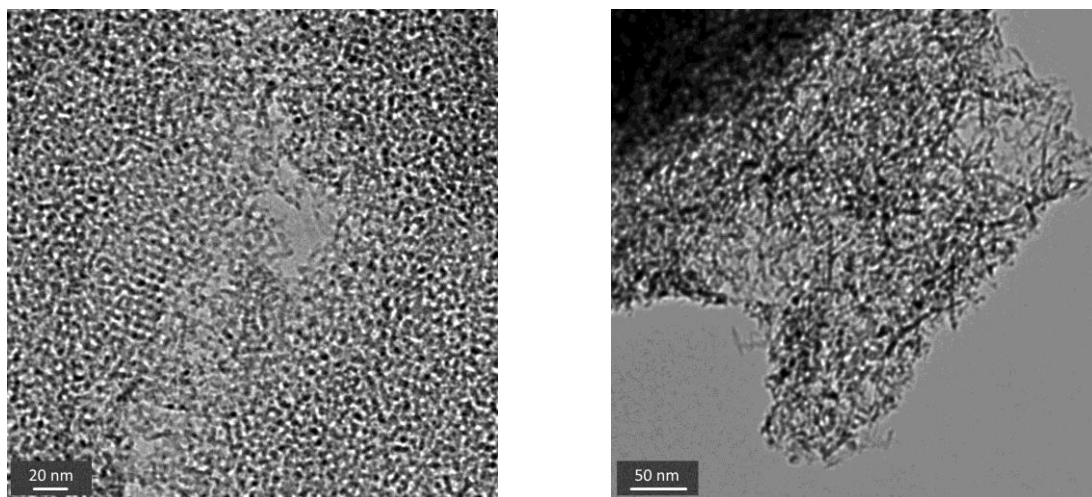
**Figure 65.** Representative TEM images of mesoporous $Al_2O_3$ materials without an ammonia vapor exposure (left) and with an exposure of 48 hours (right).

To explain these findings a simplified model is proposed, which is depicted in Scheme 7. It is assumed, that before precipitation by ammonia treatment the aluminum nitrate is homogeneously distributed over the entire pore system of the carbon matrix and that the pore volume is almost completely filled (a). The subsequent precipitation leads to densification of the material inside the carbon pores resulting in a less homogeneously distribution since part of the pore volume will be void afterwards (b). An accumulation of aluminum hydroxide or -oxyhydroxide in single, distinct regions occurs as a result of the ammonia exposure, while longer duration causes growth of these domains (c). After calcination these domains correspond to individual crystallites of $Al_2O_3$ that are larger in case of a longer duration since growth has occurred (d).

The broader pore size distribution and the increase in the average pore size is a direct consequence of the described mechanism. The porosity in the final product is no longer only a result from the structure replication but also from formation of voids between adjacent domains of aluminum hydroxide - or oxyhydroxide during the ammonia-induced precipitation. A more pronounced growth of the domains during longer ammonia treatment results in a lower degree of interconnectivity of these domains as corroborated by the TEM image of the $Al_2O_3$ sample with an ammonia exposure of 48 hours (see Figure 65, right). This is the reason for the lower mesostructural order in the final $Al_2O_3$ product when ammonia treatment is prolonged.

As a result, regular mesopores that originate from the structure replication mechanism on the one hand and interparticle voids between individual $Al_2O_3$ crystallites on the other hand are less and less distinguishable after prolonged ammonia vapor exposure. This is consistent with the generally broader pore size distribution.
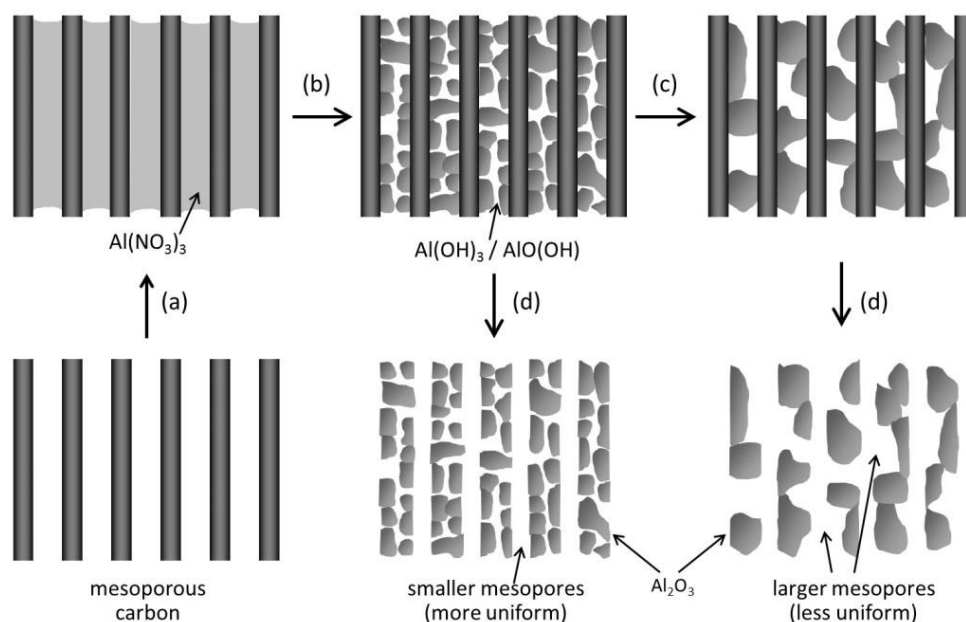


**Scheme 7.** Simplified mechanism of $Al_2O_3$ formation inside the pores of mesoporous carbon: after homogeneously filled carbon pores with $Al(NO_3)_3$ (a), subsequent ammonia vapor treatment leads to formation of aluminum hydroxide particles (b), while prolonged ammonia exposure causes growth of these particles (c), which results in larger $Al_2O_3$ crystallites after removal of the carbon matrix (d).

To sum up, it was shown that prolonged ammonia vapor exposure increases the crystallinity in almost the same way as a high calcination temperature of 900 °C instead of 700 °C. The role of the ammonia vapor treatment during the synthesis was investigated; this step has turned out to be beneficial for the crystallinity of the final $Al_2O_3$ products, whereas at the same time the mesoscopic order and the porosity of the material suffer from prolonged vapor treatment. A model was proposed to explain this relation between crystallinity and mesoscopic order.

The structural data obtained from powder X-ray diffraction analysis and $N_2$ physisorption measurements of the mesoporous $Al_2O_3$ products with ammonia vapor treatment of different durations are listed in Table 21.

**Table 21.** Structural parameters from P-XRD and $N_2$ physisorption of mesoporous $Al_2O_3$ materials prepared with variable duration of ammonia vapor treatment.

| NH$_3$ vapor treatment / h | $d_{211}$/ nm | average pore diameter [a] / nm | specific BET surface area / $m^2g^{-1}$ | specific pore volume / $cm^3g^{-1}$ |
|---|---|---|---|---|
| None | - | 7.0 | 430 | 0.68 |
| 1 | 10.7 | 4.6 | 424 | 0.98 |
| 3 | 10.0 | 7.4 | 416 | 0.99 |
| 7 | 9.1 | 8.1 | 367 | 1.01 |
| 24 | - | 9.1 | 452 | 1.29 |
| 48 | - | 12.1 | 414 | 1.20 |

[a] average pore diameter was determined by BJH method

# 5   SUMMARY

In this thesis three mesoporous metal oxide systems of spinel-type crystal structure were successfully synthesized by nanocasting. As structure matrices both mesoporous SBA-15 and KIT-6 silica phases with hexagonal and cubic ordered pore system symmetry as well as mesoporous CMK-3 and CMK-8 carbon materials were utilized. The thus-obtained metal oxide replica materials were characterized by powder X-ray diffraction analysis, nitrogen physisorption measurements, electron microscopy and energy-dispersive X-ray spectroscopy.

Mesoporous cobalt oxide ($Co_3O_4$), which is interesting for various applications in advanced technologies (*e.g.* in gas sensors or as an electrode material), was synthesized by structure replication from both SBA-15 and KIT-6 silica phases, each with different pore sizes and pore wall thicknesses. It was shown that by utilizing different structure matrices the mesostructural parameters of the resultant $Co_3O_4$ replica materials can be varied. The replica materials exhibit ordered pore systems with pore sizes between 4.2 nm and 5.6 nm while the pore wall thicknesses are between 5.6 nm and 6.7 nm, depending on the respective structure matrix. The replica materials are particularly different from each other with respect to their specific surface areas which is lower for the replica from large-pore silica compared to the replica samples from small-pore silica (80 $m^2g^{-1}$ vs. 130 $m^2g^{-1}$). The size of the crystalline domains ranges from 15 nm to 20 nm, thus extending over various repete distances of the mesopores. Additionally, the relation between the structure matrices and the replica materials on the micrometer scale was investigated. In this study it was shown that by the choice of the structural mold the morphology of the resultant replica particles can be varied. The pore interconnectivity turns out to play a major role for the different morphologies. Replication from a well-interconnected silica material, such as KIT-6 or large-pore SBA-15, yields spherical or ellipsoidal $Co_3O_4$ replica particles whereas a fibrous morphology is obtained when small-pore SBA-15 with only weak interconnectivity served as structure matrix. However, in all cases the resulting morphology is not associated with that of their utilized structural mold: mesoporous $Co_3O_4$ replica particles can be obtained either from a mesoporous silica matrix with (SBA-15) or without (KIT-6) defined particle morphology of their own. These findings can be explained by assuming the formation of

droplets inside the pores of the matrix and by a similar growth/formation mechanism as recently proposed for $In_2O_3$. With respect to potential applications the temperature stability as well as influences on the crystallinity was investigated. It was shown that mesoporous $Co_3O_4$ is thermally stable up to 500 °C, while at 600 °C the material suffers from substantial loss in mesoscopic order. However this loss in mesoscopic order is associated with a higher degree in crystallinity. In a further experiment the latter was shown to be strongly affected by the environmental atmosphere during the oxide formation, *i.e.* conversion of cobalt nitrate into cobalt oxide inside the pores of the structure matrix. However, it could not be clearly resolved if the substantial higher degree in crystallinity is actually caused by larger crystalline domains of the pore walls or by formation of bulk-phase material attached to the mesoporous material as it could be observed in the images by electron microscopy. The magnetic behavior of mesoporous $Co_3O_4$ was shown to be different from that of bulk-phase $Co_3O_4$: (i) particularly the slope of the field-dependent magnetization curve is steeper indicating higher magnetic moments, (ii) the Néel temperature is decreased, and (iii) a low ferromagnetic contribution evolves. These findings are explained by disruption of the antiferromagnetic ordering in the surface-near regions which becomes more significant the higher the surface-to volume ratio is. It was further shown that this applies to both types of interfaces, 'solid-gas interface' (BET surface area) and 'solid-solid interface' (between adjacent single crystalline domains).

The second synthesized material is cobalt iron oxide ($CoFe_2O_4$), which, as a hard magnetic material (high $H_C$), is of particular interest for application in data storage. This ternary metal oxide was also synthesized by a structure replication procedure with KIT-6 serving as structure matrix and cobalt - and iron nitrate as precursor. The thus-obtained spherical replica particles exhibit a well-ordered pore system over large distances. The material possesses a large specific surface area of about 160 $m^2g^{-1}$ and an average pore diameter of 4.9 nm, the size of the crystallite domains (*ca.* 11 nm) are slightly smaller compared to those of $Co_3O_4$. Similar to the $Co_3O_4$ system the magnetic behavior of mesoporous $CoFe_2O_4$ was investigated. Cobalt ferrite as a ferrimagnetic material shows hysteresis in its field-dependent magnetization which is also an indication for the successful synthesis of the ternary system since presence of substantial amounts of by-phases would affect the magnetic behavior. It was shown that the magnetic behavior of the mesoporous sample is different from that of bulk-phase material; with an increase of the surface-to volume ratio

the saturation magnetization and the remanence of the obtained hystereses decrease. This correlation can again be attributed to disruption of magnetic ordering in the surface-near regions. Here, however, the disruption in ferrimagnetic ordering near the surface results in reduced magnetic moments while in case of the antiferromagnetic $Co_3O_4$ material an enhancement of the magnetic moments was resulted; this reflects the characteristics of the magnetic sublattices. The described ferrimagnetic cobalt ferrite was combined with barium titanate ($BaTiO_3$), which is a well-known ferroelectric material, resulting in a composite material ($CoFe_2O_4/BaTiO_3$) which is a promising material with multiferroic properties. This composite material was obtained by combining a matrix-assisted synthesis with the citrate route: the pores of $CoFe_2O_4$ were infiltrated with a precursor solution (titanium isopropoxide and barium citrate) to create $BaTiO_3$ inside the pores of the matrix. The successful incorporation was particularly verified by X-ray diffraction analysis and nitrogen physisorption measurements. First measurements of the magnetization reveal that the ferrimagnetic behavior of the $CoFe_2O_4$ matrix remains almost unaffected by the incorporation of $BaTiO_3$ inside the pores.

Mesoporous aluminum oxide ($\gamma$-$Al_2O_3$), which plays an important role as catalyst and catalyst support material, was synthesized successfully by nanocasting, as well. Since $Al_2O_3$ is not resistant against sodium hydroxide or hydrofluoric acid, required for leaching the silica matrix in the structure replication procedure, mesoporous carbon materials (CMK-3 and CMK-8) were used as the structural molds instead. Another difference from the before-described systems is the *in-situ* precipitation with ammonia vapor to convert aluminum nitrate into aluminum hydroxide inside the pores of the matrix previously to the oxide formation. The thus-obtained $Al_2O_3$ replica materials possess high specific surface areas up to 450 $m^2g^{-1}$. However, the mesostructural order of the materials is lower than that of the before-described systems caused by substantial amounts of non-ordered domains as it could be observed in the TEM images. Also the degree of crystallinity, with crystallite sizes of about 5 nm, is lower compared to the other two systems. Variation of the synthesis conditions, by employing a melt of aluminum nitrate instead of a saturated solution of aluminum nitrate in THF results in only one single impregnation/oxide formation step required (instead of four). Thus the synthesis is more economical and less elaborate while the mesostructural properties are comparable to those of the replica materials obtained by impregnation with a precursor solution. Additionally, the relation between crystallinity and mesoscopic order was

investigated. The ammonia vapor treatment has turned out to be crucial for the degree of crystallinity. It was shown that prolonged ammonia vapor exposure increases the crystallinity of the final $Al_2O_3$ replica in just the same way as a high temperature for calcination of 900 °C (instead of 700 °C) whereas the mesoscopic order and the porosity substantially suffer from the longer ammonia exposure.

# 6 OUTLOOK

Apart from elucidating several aspects concerning synthesis details and investigation of structure-related properties for the described metal oxide systems, this thesis also offers a variety of new issues that might be considered in further investigations.

To start with mesoporous $Co_3O_4$, it was shown that the crystallinity was substantially increased by variation of the surrounding atmosphere. However, it was not clarified if the larger crystallites are actually caused by larger crystalline domains in the pore walls or by formation of bulk-like material attached to the mesoporous material as was observed by electron microscopic images. These origins need to be distinguished when control of the crystallite sizes is intended. Additionally, the gas-sensing properties of mesoporous $Co_3O_4$ will be investigated in further studies; mesoporous $Co_3O_4$ as a *p*-type semiconducting material was already shown to be sensitive to CO,[138-140] $CH_4$, $H_2$, $NH_3$ and $Cl_2$ at low temperature.[138] In this context the structure-related properties of mesoporous $Co_3O_4$ with different particle sizes and morphologies should be focused.

In this work the nanocasting approach was shown to be also successful for the synthesis of the ternary cobalt ferrite. Further work shall be dedicated to synthesis of further ternary metal oxides (*e.g.* ferrites and cobaltites) with interesting magnetic properties. Two kinds of such materials with (different) magnetic properties should be combined to composite materials, and the influence of the two magnetic ordering phenomena should be investigated. The synthesized mesoporous $CoFe_2O_4$ may also be further investigated with respect to potential applications. For instance the photocatalytic properties of this material may be analyzed, as recently reported for bulk-phase $CoFe_2O_4$.[151]

The most interesting issue addresses the obtained composite material of $CoFe_2O_4/BaTiO_3$ which needs to be further characterized. A more detailed study on the magnetic behavior should be carried out followed by characterization of the ferrielectric behavior. Particularly, the most important and interesting investigation with respect to multiferroic properties will focus on potential coupling between the two ordering phenomena.

Concerning the synthesized mesoporous $Al_2O_3$ which is frequently used as support material in catalysis, experiments should be carried out to investigate the catalytic performance of the obtained mesoporous $Al_2O_3$. The influence of the crystallinity on the catalytic performance may be investigated in additional experiments. Furthermore, in this thesis it was shown that an *in-situ* precipitation by ammonia vapor treatment turned out to be essential for the degree in crystallinity: a prolonged ammonia exposure result in $Al_2O_3$ with higher crystallinity. Therefore it should be examined if this precipitation step previously to the oxide formation could be also applied for other metal oxide systems, such as ZnO, MgO or even for metal oxide systems replicated from silica materials.

# 7 ZUSAMMENFASSUNG

Im Rahmen dieser Arbeit wurden drei verschiedene mesoporöse Metalloxid-Systeme mit Spinellstruktur erfolgreich mittels "Nanocasting" hergestellt. Als Strukturmatrices wurden zwei Silicaphasen, SBA-15 und KIT-6 mit hexagonal und kubisch geordnetem Porensystem, verwendet sowie deren mesoporöse Kohlenstoff-Analoga CMK-3 und CMK-8. Die erhaltenen Metalloxid Replika-Materialien wurden mittels Pulver-Röntgendiffraktometrie, Stickstoff-Physisorptionsmessungen, Elektronenmikroskopie und energiedispersiver Röntgenspektroskopie charakterisiert.

Zunächst wurde mesoporöses Cobaltoxid ($Co_3O_4$), das für Anwendungen in der Gassensorik oder als Elektrodenmaterial interessant ist, durch Strukturreplikation aus beiden Silicaphasen, SBA-15 und KIT-6, hergestellt. Hierbei wurden beide Arten von Silica mit unterschiedlichen Porengrößen und -wandstärken verwendet. Es wurde gezeigt, dass durch die Wahl der Strukturmatrix die mesoskopischen Struktureigenschaften der resultierenden $Co_3O_4$ Replika-Materialien variiert werden können. Die erhaltenen Replika-Materialien verfügen in Abhängigkeit der eingesetzten Strukturmatrix über geordnete Porensysteme mit Porengrößen zwischen 4.2 nm und 5.6 nm, während die Porenwandstärken zwischen 5.6 nm und 6.7 nm liegen. Die erhaltenen Cobaltoxid-Materialien unterscheiden sich jedoch vor allem im Hinblick auf ihre spezifischen Oberflächen, die mit 80 $m^2g^{-1}$ für $Co_3O_4$, welches aus großporigem Silica hergestellt wurde, niedriger ist als für $Co_3O_4$ aus kleinporigem Silica, welches eine Oberfläche von etwa 130 $m^2g^{-1}$ hat. Die Größe der kristallinen Domänen liegt zwischen 15 nm und 20 nm und erstreckt sich somit über die Länge mehrerer Porenabstände. Des Weiteren wurden strukturelle Zusammenhänge, sowohl auf mesoskopischer als auch makroskopischer Ebene, zwischen der Strukturmatrix und dem resultierenden Replika-Material untersucht. Hierbei wurde gezeigt, dass durch die Wahl der Strukturmatrix die Morphologie des erhaltenen Replika-Materials variiert werden kann und die Poreninterkonnektivität der Strukturmatrix dafür wesentlich verantwortlich ist. Während man im Falle einer Strukturreplikation, ausgehend von einem Silica-Material mit guter Poreninterkonnektivität, wie im KIT-6 oder im großporigen SBA-15, sphärische bzw. elliptische $Co_3O_4$ Partikel erhält, beobachtet man eine faserartige Morphologie für die Replikation eines kleinporigen SBA-15, welches eine schlechtere Interkonnektivität der

Poren aufweist. In allen Fällen jedoch bestand kein Zusammenhang zwischen der Morphologie der Strukturmatrix und der Replika-Materialien: Es konnten $Co_3O_4$-Partikel mit einer definierten Morphologie erhalten werden, ausgehend von einer Strukturmatrix, die entweder selbst eine (SBA-15) definierte Morphologie besitzt oder auch keine (KIT-6). Diese Ergebnisse lassen sich durch die Annahme der Bildung von Tröpfchen in den Poren der Strukturmatrix während der Synthese erklären. Dieser Bildungsmechanismus wurde bereits für mesoporöses Indiumoxid ($In_2O_3$) beschrieben und konnte somit auch für $Co_3O_4$ angewendet werden. Im Hinblick auf mögliche Anwendungen des Materials wurde die thermische Stabilität untersucht, wie auch verschiedene Einflüsse auf die Kristallinität. Hierbei konnte gezeigt werden, dass das hergestellte mesoporöse $Co_3O_4$ bis 500 °C stabil ist, während ab 600 °C die mesoskopische Ordnung deutlich leidet. Allerdings geht dieser Verlust an mesoskopischer Ordnung mit einer Bildung größerer Kristallite einher. In weiteren Untersuchungen konnte gezeigt werden, dass die Kristallinität sehr stark von der umgebenden Atmosphäre abhängt, die bei der Oxidbildung (Umsetzung von Cobaltnitrat in Cobaltoxid) vorherrscht. Allerdings konnte nicht festgestellt werden, ob der höhere Grad an Kristallinität tatsächlich von größeren Kristalliten in der Porenwand resultiert oder ob unporöses ("bulk") Material, welches sich um das mesoporöse Material herum gebildet hat, wie es in den elektronenmikroskopischen Aufnahmen zu sehen ist, die Ursache dafür ist. Darüber hinaus wurde gezeigt, dass sich das magnetische Verhalten von mesoporösem $Co_3O_4$ von dem des "bulk"-$Co_3O_4$ unterscheidet: (i) die Steigung in der feldabhängigen Magnetisierungskurve ist steiler, was auf ein größeres magnetisches Moment hinweist, (ii) die Néel-Temperatur ist geringer und (iii) ein schwacher Ferromagnetismus bildet sich aus. Diese Beobachtungen können durch Störung der antiferromagnetischen Ordnung in oberflächennahen Regionen erklärt werden, welche mit größerem Oberfläche-zu-Volumen-Verhältnis immer bedeutender wird. Des Weiteren konnte gezeigt werden, dass hierbei beide Grenzflächen berücksichtigt werden müssen, nämlich nicht nur 'fest-gasförmig' (BET Oberfläche), sondern auch 'fest-fest' Grenzflächen (zwischen benachbarten einkristallinen Domänen).

Das zweite hergestellte System war Cobalteisenoxid ($CoFe_2O_4$), welches als hartes magnetisches Material mit hoher Koerzitivität besonders für Anwendungen im Bereich der Datenspeicherung von Interesse ist. Dieses ternäre Metalloxid wurde ebenfalls durch ein Strukturreplikationsverfahren hergestellt, wobei KIT-6 Silica als Strukturmatrix diente und

Cobaltnitrat und Eisennitrat als Vorläuferverbindungen verwendet wurden. Die so erhaltenen sphärischen Replika-Partikel verfügen über ein weitreichend geordnetes Porensystem. Das Material verfügt über eine große spezifische Oberfläche von etwa 160 m$^2$g$^{-1}$ und einen durchschnittlichen Porenradius von 4.9 nm, die Größe der kristallinen Domänen war mit *ca.* 11 nm etwas kleiner als die von Co$_3$O$_4$. Ähnlich wie im Fall von mesoporösem Co$_3$O$_4$ wurde auch hier das magnetische Verhalten von mesoporösem CoFe$_2$O$_4$ untersucht. Im Gegensatz zu Co$_3$O$_4$ wurde für Cobaltferrit, welches ein ferrimagnetisches Material ist, eine Hysterese in der Messung der feldabhängigen Magnetisierung beobachtet. Diese ist im Übrigen ein weiteres Indiz dafür, dass die Synthese des ternären Systems erfolgreich war, denn im Falle von Nebenphasen würden diese das magnetische Verhalten beeinflussen. Es konnte auch hier wieder gezeigt werden, dass sich das magnetische Verhalten von mesoporösem Material von dem von bulk-Material unterscheidet; mit zunehmendem Oberfläche-zu-Volumen-Verhältnis nahmen die Sättigungsmagnetisierung und die Remanenz der erhaltenen Hysteresen ab. Dieser Zusammenhang kann ebenfalls auf Störung der magnetischen Ordnung in den oberflächennahen Regionen zurückgeführt werden. Diese Störung der ferrimagnetischen Ordnung führte hier allerdings zu einem geringeren magnetischen Moment, während im Fall des antiferromagnetischen Co$_3$O$_4$ ein verbessertes magnetisches Moment resultierte. Dies liegt an den Spin-Eigenschaften der einzelnen Untergitter. Das hier beschriebene CoFe$_2$O$_4$ wurde in einem weiteren Schritt mit Bariumtitanat (BaTiO$_3$), einem bekannten ferroelektrischen Material, zu einem Kompositmaterial kombiniert, welches ein vielversprechendes Material mit multiferroischen Eigenschaften ist. Dieses Komposit wurde in einer matrix-unterstützten Synthese mittels Citrat-Route hergestellt. Hierbei wurden die Poren des zuvor hergestellten mesoporösen CoFe$_2$O$_4$ mit einer Precursor-Lösung (Titanisopropoxid und Bariumcitrat) gefüllt und in den Poren *in situ* in das Oxid überführt. Die erfolgreiche Füllung der Poren mit BaTiO$_3$ wurde insbesondere mit Hilfe von Pulver-Röntgendiffraktometrie-Analyse und Stickstoff-Physisorptions-Messungen bestätigt. Erste magnetische Messungen zeigten, dass das ferrimagnetische Verhalten der CoFe$_2$O$_4$ Matrix durch das Vorhandensein von BaTiO$_3$ in den Poren nahezu nicht beeinflusst wurde.

Mesoporöses Aluminiumoxid ($\gamma$-Al$_2$O$_3$), welches eine wichtige Rolle als Katalysator bzw. Trägermaterial für die Katalyse spielt, wurde ebenfalls durch Nanocasting erfolgreich hergestellt. Da Al$_2$O$_3$ nicht beständig gegenüber Natronlauge oder Flusssäure ist, welche zum

Ätzen der Silicamatrix verwendet werden, musste hier mesoporöser Kohlenstoff (CMK-3 und CMK-8) als Strukturmatrix verwendet werden. Ein weiterer Unterschied zu den zuvor beschriebenen Systemen ist, dass vor der Oxidbildung zunächst mit Ammoniak-Dampf Aluminiumhydroxid in den Poren ausgefällt wurde. Die resultierenden Replika-Materialien verfügen über hohe spezifische Oberflächen von bis zu 450 $m^2g^{-1}$, jedoch ist die mesoskopische Ordnung der erhaltenen $Al_2O_3$ Replika-Materialien kleiner im Vergleich zu den zuvor beschriebenen Systemen, was durch größere Mengen an unporösem Material verursacht wird, welche man in den TEM Aufnahmen sehen konnte. Ebenso ist der Grad an Kristallinität deutlich geringer im Vergleich zu den anderen beiden Systemen; die Kristallitgröße betrug etwa 5 nm. Durch Variation der Synthesebedingungen, durch Verwenden einer Schmelze zum Imprägnieren anstelle einer gesättigten Aluminiumnitrat-Lösung in THF, konnte die Anzahl an Imprägnierungs-/Oxidbildungsschritten auf nur noch einen reduziert werden (von vier). Somit ist die Synthese ökonomischer und weniger zeitintensiv, während die mesoskopischen Eigenschaften vergleichbar sind mit den Proben, die mittels einer Precursor-Lösung imprägniert wurden. Außerdem wurde der Zusammenhang zwischen Kristallinität und mesoskopischer Ordnung untersucht. Die Behandlung mit Ammoniak-Dampf erwies sich als sehr ein sehr wesentlicher Syntheseschritt für die Kristallinität des $Al_2O_3$ Produktes. Es wurde gezeigt, dass eine längere Ammoniak-Dampf Behandlung zu einer Vergrößerung an Kristalliten führt, während jedoch gleichzeitig die mesoskopische Ordnung darunter leidet.

# 8 REFERENCES

[1] C. T. Kresge, M. E. Leonowicz, W. J. Roth, J. C. Vartuli and J. S Beck, *Nature* 359 (1992) 710.

[2] K. S. W. Sing, D. H. Everett, R. A. W. Haul, L. Moscou, R. A. Pierotti, J. Rouquérol and T. Siemieniewska, *Pure Appl. Chem.* 57 (1985) 603.

[3] A. Corma, *Chem. Rev.* 97 (1997) 2373.

[4] U. Ciesla and F. Schüth, *Microporous Mesoporous Mater.* 27 (1999) 131.

[5] J. Y. Ying, C. P. Mehnert and M. S. Wong, *Angew. Chem. Int. Ed.* 38 (1999) 56.

[6] A. Taguchi and F. Schüth, *Microporous Mesoporous Mater.* 77 (2005) 1.

[7] M. Hartmann, *Chem. Mater.* 17 (2005) 4577.

[8] M. Valles-Regí, F. Balas and D. Arcos, *Angew. Chem. Int. Ed.* 46 (2007) 7548.

[9] Y. Wan, Y. Shi and D. Zhao, *Chem. Commun.* (2007) 897.

[10] Y. Ren, Z. Ma and P. G. Bruce, *Chem. Soc. Rev.* 41 (2012) 4909.

[11] T. Wagner, S. Haffer, C. Weinberger, D. Klaus and M. Tiemann, *Chem. Soc. Rev.* 42 (2013) 4036.

[12] D. Gu and F. Schüth, *Chem. Soc. Rev.* (2013), DOI: 10.1039/c3cs60155b.

[13] G. J. A. A. Soler-Illia, C. Sanchéz, B. Lebeau and J. Patarin, *Chem. Rev.* 102 (2002) 4093.

[14] G. J. A. A. Soler-Illia, E. L. Crepaldi, D. Grosso and C. Sanchez, *Curr. Opin. Colloid Interface Sci.* 8 (2003) 109.

[15] A. Berggren, A. E. C. Palmqvist and K. Holmberg, *Soft Matt.* 1 (2005) 219.

[16] F. Hoffmann, M. Cornelius, J. Morell and M. Fröba, *Angew. Chem. Int. Ed.* 45 (2006) 3216.

[17] Y. Wan and D. Zhao, *Chem. Rev.* 107 (2007) 2821.

[18] J. S. Beck, J. C. Vartuli, W. J. Roth, M. E. Leonowicz, C. T. Kresge, K. D. Schmitt, C. T.-W. Chu, D. H. Olson, E. W. Sheppard, S. B. McCullen, J. B. Higgins and J. L Schlenker, *J. Am. Chem. Soc.* 114 (1992) 10834.

[19] J. C. Vartuli, K. D. Schmitt, C. T. Kresge, W. J. Roth, M. E. Leonowicz, S. B. McCullen, S. D. Hellring, J. S. Beck, J. L. Schlenker, D. H. Olson and E. W. Sheppard, *Chem. Mater.* 6 (1994) 2317.

[20] D. Zhao, J. Feng, Q. Huo, N. Melosh, G. H. Fredrickson, B. F. Chmelka and G. D. Stucky, *Science* 279 (1998) 548.

[21] D. Zhao, Q. Huo, J. Feng, B. F. Chmelka and G. D. Stucky, *J. Am. Chem. Soc.* 120 (1998) 6024.

[22] F. Kleitz, S. H. Choi and R. Ryoo, *Chem. Commun.* (2003) 2136.

[23] M. Tiemann, *Chem. Mater.* 20 (2008) 961.

24      Y. Wan, Y. Shi and D. Zhao, *Chem. Mater.* 20 (2008) 932.

25      P. Yang, D. Zhao, D. I. Margolese, B. F. Chmelka and G. D. Stucky, *Nature* 396 (1998) 152.

26      P. Yang, D. Zhao, D. I. Margolese, B. F. Chmelka and G. D. Stucky, *Chem. Mater.* 11 (1999) 2813.

27      F. Schüth, *Chem. Mater.* 13 (2001) 3184.

28      Y. Wan, H. Yang and D. Zhao, *Acc. Chem. Res.* 39 (2006) 423.

29      D. Grosso, F. Cagnol, G. J. A. A. Soler-Illia, E. L. Crepaldi, H. Amenitsch, A. Brunet-Bruneau, A. Bourgeois and C. Sanchez, *Adv. Funct. Mater.* 14 (2004) 309.

30      B. Smarsly and M. Antonietti, *Eur. J. Inorg. Chem.* (2006) 1111.

31      N. Ishizuka, H. Minakuchi, K. Nakanishi, N. Soga and N. Tanaka, *J. Chromatogr. A* 797 (1998) 133.

32      H. Yang, Q. Shi, B. Tian, S. Xie, F. Zhang, Y. Yan, B. Tu and D. Zhao, *Chem. Mater.* 15 (2003) 536.

33      O. Núñez, K. Nakanishi and N. Tanaka, *J. Chromatogr. A* 1191 (2008) 231.

34      B. Smarsly, D. Grosso, T. Brezesinski, N. Pinna, C. Boissière, M. Antonietti and C. Sanchez, *Chem. Mater.* 16 (2004) 2948.

35      T. Brezesinski, A. Fischer, K.Iimura, C. Sanchez, D. Grosso, M. Antonietti and B. Smarsly, *Adv. Funct. Mater.* 16 (2006) 1433.

36      J. H. Pan and W. I. Lee, *Chem. Mater.* 18 (2006) 847.

37      J. H. Pan, S. Y. Chai, C. Lee, S.-E. Park and W. I. Lee, *J. Phys. Chem. C* 111 (2007) 5582.

38      J. Konishi, K. Fujita, K. Nakanishi and K. Hirao, *Chem. Mater.* 18 (2006) 6069.

39      B. Gawel, K. Gawel and G. Øye, *Materials* 3 (2010) 2815.

40      M. Nedelcu, S. Guldin, M. C. Orilall, J. Lee, S. Hüttner, E. J. W. Crossland, S. C. Warren, C. Duacti, P. R. Laity, D. Eder, U. Wiesner, U. Stein and H. Snaith, *J. Mater. Chem.* 20 (2010) 1261.

41      G. Orsini and V. Tricoli, *J. Mater. Chem.* 20 (2010) 6299.

42      M. Antonelli and J. Y. Ying, *Angew. Chem. Int. Ed.* 34 (1995) 2014.

43      B. Tian, H. Yang, X. Liu, S. Xie, C. Yu, J. Fan, B. Tu and D. Zhao, *Chem. Commun.* (2002) 1824.

44      S. A. Bagshaw and T. J. Pinnavaia, *Angew. Chem. Int. Ed.* 35 (1996) 1102.

45      F. Vaudry, S. Khodabandeh and M. E. Davis, *Chem. Mater.* 8 (1996) 1451.

46      W. Deng, M. W. Toepke and B. H. Shanks, *Adv. Funct. Mater.* 13 (2003) 61.

47      Q. Yuan, A. X. Yin, C. Luo, L. D. Sun, Y. W. Zhang, W. T. Duan, H. C. Liu and C. H. Yan, *J. Am. Chem. Soc.* 130 (2008) 3465.

48      Y. Wang, C. Ma, X. Sun and H. Li, *Microporous Mesoporous Mater.* 49 (2001) 171.

49      N. Pal, M. Paul and Bhaumik, *Appl. Catal. A* 393 (2011) 153.

50      X. Fan, Y. Wang, X. Chen, L. Gao, W. Luo, Y. Yuan, Z. Li, T. Yu, J. Zhu and Z. Zhou, *Chem. Mater.* 22 (2010) 1276.

51    C. Reitz, C. Suchomski, C. Weidmann and T. Brezesinski, *Nano. Res.* 4 (2011) 414.

52    F. Schüth, *Angew. Chem. Int. Ed.* 42 (2003) 3604.

53    H. Yang and D. Zhao, *J. Mater. Chem.* 15 (2005) 1217.

54    A. H. Lu and F. Schüth, *Adv. Mater.* 18 (2006) 1793.

55    T. Valdés-Solís and A. B. Fuertes, *Mater. Res. Bull.* 41 (2006) 2187.

56    A. Thomas, F. Goettermann and M. Antonietti, *Chem. Mater.* 20 (2008) 738.

57    C. Liang, Z. Li and S. Dai, *Angew. Chem. Int. Ed.* 47 (2008) 3696.

58    Y. Xia, Z. Yang and R. Mokaya, *Nanoscale* 2 (2010) 639.

59    X. Sun, Y. Shi, P. Zhang, C. Zheng, X. Zheng, F. Zhang, Y. Zhang, N. Guan, D. Zhao and G. D. Stucky, *J. Am. Chem. Soc.* 133 (2011) 14542.

60    S. Lepoutre, J.-H. Smått, C. Laberty, H. Amenitsch, D. Grosso and M. Lindén, *Microporous Mesoporous Mater.* 123 (2009) 185.

61    B. Tian, X. Liu, H. Yang, S. Xie, C. Yu, B. Tu and D. Zhao, *Adv. Mater.* 15 (2003) 1370.

62    B. Tian, X. Liu, L. A. Solovyov, Z. Liu, H. Yang, Z. Zhang, S. Xie, F. Zhang, B. Tu, C. Yu, O. Terasaki and D. Zhao, *J. Am. Chem. Soc.* 126 (2004) 865.

63    C. Dickinson, W. Zhou, R. P. Hodgkins, Y. Shi, D. Zhao and H. He, *Chem. Mater.* 18 (2006) 3088.

64    S. C. Laha and R. Ryoo, *Chem. Commun.* (2003) 2138.

65    J. Roggenbuck, T. Waitz and M. Tiemann, *Microporous Mesoporous Mater.* 113 (2008) 575.

66    W. Yue and W. Zhou, *Chem. Mater.* 19 (2007) 2359.

67    Y. M. Wang, Z. Y. Wu, L. Y. Shi and J. H. Zhu, *Adv. Mater.* 17 (2005) 323.

68    W. Yue, A. H. Hill, A. Harrison and W. Zhou, *Chem. Commun.* (2007) 2518.

69    J. K. Shon, S. S. Kong, Y. S. Kim, J.-H. Lee, W. K. Park, S. C. Park and J. M. Kim, *Microporous Mesoporous Mater.* 120 (2009) 441.

70    M. Imperor-Clerc, D. Bazin, M.-D. Appay, P. Beaunier and A. Davidson, *Chem. Mater.* 16 (2004) 1813.

71    F. Jiao and P. G. Bruce, *Adv. Mater.* 19 (2007) 657.

72    T. A. Crowley, K. J. Ziegler, D. M. Lyons, D. Erts, H. Olin, M. A. Morris and J. D. Holmes, *Chem. Mater.* 15 (2003) 3518.

73    J. Deng, L. Zhang, H. Dai, Y. Xia, H. Jiang, H. Zhang and H. He, *J. Phys. Chem. C* 114 (2010) 2694.

74    J. Parmentier, L. A. Solovyov, F. Ehrburger-Dolle, J. Werckmann, O. Ersen, F. Bley and J. Patarin, *Chem. Mater.* 18 (2006) 6316.

75    J.-H. Smått, C. Weidenthaler, J. B. Rosenholm and M. Lindén, *Chem. Mater.* 18 (2006) 1443.

76    J.-H. Smått, N. Schüwer, M. Järn, W. Lindner and M. Lindén, *Microporous Mesoporous Mater.* 112 (2008) 308.

77    J.-H. Smått, M. Lindén, T. Wagner, C.-D. Kohl and M. Tiemann, *Sens. Actuators B* 155 (2011) 483.

78    S. Lepoutre, B. Julián-López, C. Sanchez, H. Amenitsch, M. Lindén and D. Grosso, *J. Mater. Chem.* 20 (2010) 537.

79    C. Yu, J. Fan, B. Tian, D. Zhao and G. D. Stucky, *Adv. Mater.* 14 (2002) 1742.

80    S. Haffer, T. Waitz and M. Tiemann, *J. Phys. Chem. C* 114 (2010) 2075.

81    V. Pillai and D. O. Shah, *J. Magn. Magn. Mater.* 163 (1996) 243.

82    J. Zhu and Q. Gao, *Microporous Mesoporous Mater.* 124 (2009) 144.

83    Q. Lu, Y. Chen, W. Li, J. G. Chen, J. Q. Xiao and F. Jiao, *J. Mater. Chem. A* 1 (2013) 2331.

84    Y. Sun, G. Ji, M. Zheng, X. Chang, S. Li and Y. Zhang, *J. Mater. Chem.* 20 (2010) 945.

85    H. Yen, Y. Seo, R. Guillet-Nicolas, S. Kaliaguine and F. Kleitz, *Chem. Commun.* 47 (2011) 10473.

86    M. M. Nair, F. Kleitz and S. Kaliaguine, *Chem. Cat. Chem.* 4 (2012) 387.

87    J. H. Smått, B. Spliethoff, J. B. Rosenholm and M. Lindén, *Chem. Commun.* (2004) 2188.

88    Y. Wang, C. M. Yang, W. Schmidt, B. Spliethoff, E. Bill and F. Schüth, *Adv. Mater.* 17 (2005) 53.

89    A. Rumplecker, F. Kleitz, E.-L. Salabas and F. Schüth, *Chem. Mater.* 19 (2007) 485.

90    P. Shu, J. Ruan, C. Gao, H. Li and S. Che, *Microporous Mesoporous Mater.* 123 (2009) 314.

91    M. Cabo, E. Pellicer, E. Rossinyol, M. Estrader, A. Lopéz-Ortega, J. Nogués, O. Castell, S. Suriñach and M. D. Baró, *J. Mater. Chem.* 20 (2010) 7021.

92    H. Tüysüz, E. L. Salabas, E. Bill, H. Bongard, B. Spliethoff, C. W. Lehmann and F. Schüth, *Chem. Mater.* 24 (2012) 2493.

93    H. Yang, Q. Shi, B. Tian, Q. Lu, F. Gao, S. Xie, J. Fan, C. Yu, B. Tu and D. Zhao, *J. Am. Chem. Soc.* 125 (2003) 4724.

94    T. Waitz, T. Wagner, T. Sauerwald, C.-D. Kohl and M. Tiemann, *Adv. Funct. Mater.* 19 (2009) 653.

95    H. Kim and J. Cho, *J. Mater. Chem.* 18 (2008) 771.

96    T. Waitz, B. Becker, T. Wagner, T. Sauerwald, C. D. Kohl and M. Tiemann, *Sens. Actuators B* 150 (2010) 788.

97    J. Zhao, W. Wang, Y. Liu, J. Ma, X. Li, Y. Du and G. Lu, *Sens. Actuators B* 160 (2011) 604.

98    E. Rossinyol, J. Arbiol, F. Peíro, A. Cornet, J. R. Morante, B. Tian, T. Bo and D. Zhao, *Sens. Actuators B* 109 (2005) 57.

99    P. Ji, J. Zhang, F. Chen and M. Anpo, *J. Phys. Chem. C* 112 (2008) 17809.

100  B. Puertolas, B. Solsona, S. Agouram, R. Murillo, A. M. Mastral, A. Aranda, S. H. Taylor and T. Garcia, *Appl. Catal. B: Environmental* 93 (2010) 395.

101  F. Jiao, A. H. Hill, A. Harrison, A. Berko, A. V. Chadwick and P. Bruce, *J. Am. Chem. Soc.* 130 (2008) 5262.

102  E. Rossinyol, A. Prim, E. Pellicer, J. Arbiol, F. Hernández-Ramírez, F. Peiró, A. Cornet, J. R. Morante, L. A. Solovyyov, B. Tian, T. Bo and D. Zhao, *Adv. Funct. Mater.* 17 (2007) 1801.

103  H. Liu, X. Du, X. Xing, G. Wang and S. Z. Qiao, *Chem. Commun.* 48 (2012) 865.

104  H. Tüysüz, C. Weidenthaler, T. Grewe, E. L. Salabas, M. J. B. Romero and F. Schüth, *Inorg. Chem.* 51 (2012) 11745.

105  F. Jiao, A. Harrison, J.-C. Jumas, A. V. Chadwick, W. Kockelmann and P. G. Bruce, *J. Am. Chem. Soc.* 128 (2006) 5468.

106  W. Yue, X. Xu, J. T. S. Irvine, P. S. Attidekou, C. Liu, H. He, D. Zhao and W. Zhou, *Chem. Mater.* 21 (2009) 2540.

107  W. Shen, J. Shi, H. Chen, J. Gu, Y. Zhu and X. Dong, *Chem. Lett.* 34 (2005) 390.

108  M. Gu, B. Yue, R. Bao and H. He, *Mater. Res. Bul.* 44 (2009) 1422.

109  H. Yen, Y. Seo, R. Guillet-Nicolas, S. Kaliaguine and F. Kleitz, *Chem. Commun.* 47 (2011) 10473.

110  X. Gu, W. Zhu, C. Jia, R. Zhao, W. Schmidt and Y. Wang, *Chem. Commun.* 47 (2011) 5337.

111  A. H. de Morais Batista, F. S. O. Ramos, T. P. Braga, C. L. Lima, F. F. de Sousa, E. B. D. Barros, J. M. Filho, A. S. de Oliveira, J. R. de Sousa, A. Valentini and A. C. Oliveira, *Appl. Catal. A: General* 382 (2010) 148.

112  S. Liu, B. Yue, K. Jiao, Y. Zhou and H. He, *Mater. Lett.* 60 (2006) 154.

113  Y. Wang, J. Ren, Y. Wang, F. Zhang, X. Liu, Y. Guo and G. Lu, *J. Phys. Chem. C* 112 (2008) 15293.

114  Y. Wang, X. Cui, Y. Li, Z. Shu, H. Chen and J. Shi, *Microporous Mesoporous Mater.* 176 (2013) 8.

115  J. Zhao, Y. Liu, X. Li, G. Lu, L. You, X. Liang, F. Liu, T. Zhang and Y. Du, *Sens. Actuators B* 181 (2013) 802.

116  Q. Liu, A. Wang, X. Wang and T. Zhang, *Chem. Mater.* 18 (2006) 5153.

117  Q. Liu, A. Wang, J. Xu, Y. Zhang, X. Wang and T. Zhang, *Microporous Mesoporous Mater.* 116 (2008) 461.

118  Z. Wu, Q. Li, D. Feng, P. A. Webley and D. Zhao, *J. Am. Chem. Soc.* 132 (2010) 12042.

119  J. Roggenbuck and M. Tiemann, *J. Am. Chem. Soc.* 127 (2005) 1096.

120  J. Roggenbuck, G. Koch and M. Tiemann, *Chem. Mater.* 18 (2006) 4151.

121  T. Waitz, M. Tiemann, P. J. Klar, J. Sann, J. Stehr and B. K. Meyer, *Appl. Phys. Lett.* 90 (2007) 123108.

122  T. Wagner, T. Waitz, J. Roggenbuck, M. Fröba, C.-D Kohl and M. Tiemann, *Thin Solid Films* 515 (2007) 8360.

123  S. Polarz, A. V. Orlov, F. Schüth and A.-H. Lu, *Chem. Eur. J.* 13 (2007) 592.

124  J. Roggenbuck, H. Schäfer, T. Tsoncheva, C. Minchev, J. Hanss and M. Tiemann, *Microporous Mesoporous Mater.* 101 (2007) 335.

125  X. Lai, X. Li, W. Geng, J. Tu, J. Li and S. Qiu, *Angew. Chem. Int. Ed.* 46 (2007) 738.

126  X.-L. Xu, Z.-H. Chen, Y. Li, W.-K. Chen and J.-Q. Li, *Surf. Sci.* 603 (2009) 653.

127  U. Müller, *Anorganische Strukturchemie*, 6. Auflage, Vieweg und Teubner, Wiesbaden, 2008.

128  W. L. Roth, *J. Phys. Chem. Solid* 24 (1964) 1.

129  B. Varghese, B. Mukherjee, K. R. G. Karthik, K. B. Jinesh, S. G. Mhaisalkar, E. S. Tok and C. H. Sow, *J. Appl. Physics* 111 (2012) 104306.

130  X. Wang, W. Tian, T. Zhai, C. Zhi, Y. Bando and D. Golberg, J. *Mater. Chem.* 22 (2012) 23310.

131  H. G. El-Shobaky, *Appl. Catal. A: General* 278 (2004) 1.

132  H. Tüysüz, M. Comotti and F. Schüth, *Chem. Commun.* (2008) 4022.

133  X. Xie, Y. Li, Z.Q. Liu, M. Haruta and W. Shen, *Nature* 458 (2009) 746.

134  D. Jiang and S. Dai, *Phys. Chem. Chem. Phys.* 13 (2011) 978.

135  H. F. Wang, R. Kavanagh, Y. L. Guo, G. Lu and P. Hu, *J. Catal.* 296 (2012) 110.

136  H. Tüysüz, Y. J. Hwang, S. B. Khan, A. M. Asin and P. Yang, *Nano Res.* 6 (2013) 47.

137  H. Yamaura, K. Moriya, N. Miura and N. Yamazoe, *Sens. Actuators B* 65 (2000) 39.

138  J. Wöllenstein, M. Burgmair, G. Plescher, T. Sulima, J. Hildenbrand, H. Böttner and I. Eisele, *Sens. Actuators B* 93 (2003) 442.

139  T. Wagner, J. Roggenbuck, C.-D. Kohl, M. Fröba and M. Tiemann, *Stud. Surf. Sci. Catal.* 165 (2006) 347.

140  C.-Y. Liu, C.-F. Chen and J.-P. Leu, *Sens. Actuators B* 137 (2009) 700.

141  K. I. Choi, H. R. Kim, K. M. Kim, D. Liu, G. Cao and J. H. Lee, *Sens. Actuators B* 146 (2010) 183.

142  G. Wang, H. Liu, J. Horvat, B. Wang, S. Qiao, J. Park and H. Ahn, *Chem. Eur. J.* 16 (2010) 11020.

143  K. M. Shaju, F. Jiao, A. Debárt and P. G. Bruce, *Phys. Chem. Chem. Phys.* 9 (2007) 1837.

144  W.-Y. Li, L. N. Xu and J. Chen, *Adv. Funct. Mater.* 15 (2005) 851.

145  G. A. Sawatzky, F. Van der Woude and A. H. Morrish, *Phys. Rev.* 187 (1969) 747.

146  Y. H. Hou, Y. J. Zhao, Z. W. Liu, H. Y. Yu, X. C. Zhong, W. Q. Qiu, D. C. Zeng and L. S. Wen, *J. Phys. D: Appl. Phys.* 43 (2010) 445003.

147    A. H. Morrish, *The Physical Principle of Magnetism*, R. E. Krieger Publishing Company, Inc., Huntington (NY), 1980, p. 507.

148    J.-G. Lee, J. Y. Park, Y.-J. Oh and C. S. Kim, *J. Appl. Physics* 84 (1998) 2801.

149    P. Lavela, G. F. Ortiz, J. L. Tirado, E. Zhecheva, R. Stoyanova and S. Ivanova, *J. Phys. Chem. C* 111 (2007) 14238.

150    G. Baldi, D. Bonacchi, C. Innocenti, G. Lorenzi and C. Sangregorio, *J. Magn. Magn. Mater.* 311 (2007) 10.

151    Z. Zhu, X. Li, Q. Zhao, Y. Shi, H. Li and G. Chen, *J. Nanopart. Res.* 13 (2011) 2147.

152    E. Manova, T. Tsoncheva, D. Paneva, I. Mitov, K. Tenchev and L. Petrov, *Appl. Catal. A: General* 277 (2004) 11.

153    K. Sreekumar, T. Mathew, R. Rajgopal, R. Vetrivel and B.S. Rao, *Catal. Lett.* 65 (2000) 99.

154    K. Sreekumar and S. Sugunan, *J. Mol. Catal. A: Chemical* 185 (2002) 259.

155    F. H. Streitz and J. W. Mintmire, *Phys. Rev. B* 60 (1999) 773.

156    G. W. Watson and D. J. Willock, *Chem. Commun.* (2001) 1076.

157    A. Vijay, G. Mills and H. Metiu, *J. Chem. Phys.* 117 (2002) 4509.

158    W. D. Bancroft and A. B. George, *J. Phys Chem.* 35 (1931) 2943.

159    L. Kaluža, M. Zdražil, N. Žilková and J. Čejka, *Catal. Commun.* 3 (2002) 151.

160    J. Čejka, *Appl. Catal. A: General* 254 (2003) 327.

161    M. Digne, P. Sautet, P. Raybaud, P. Euzen and H. Toulhoat, *J. Catal.* 226 (2004) 54.

162    S. M. Morris, P. F. Fulvio and M. Jaroniec, *J. Am. Chem. Soc.* 130 (2008) 15210.

163    Z. D. Huang, W. Bensch, A. Lotnyk, L. Kienle, S. Fuentes, J. Bocarando, G. Alonso and C. Ornelas, *J. Mol. Catal. A: Chemical* 323 (2010) 45.

164    L. E. Smart and E. A. Moore, *Solid State Chemistry*, 3rd edition, CRC Press, Boca Raton, 2005.

165    S. Saha, T. P. Sinha and A. Mookerjee, *Phys. Rev. B* 62 (2000) 8828.

166    M. Kinka, J. Banys, W. Böhlmann, E. Bierwirth, M. Hartmann, D. Michael, G. Völkel and A. Pöppl, *IEEE Transactions on Ultrasonics, Ferroelectrics, and Frequency Control* 53 (2006) 2305.

167    R. Z. Hou, P. Ferreira and P. M. Vilarinho, *Microporous Mesoporous Mater.* 110 (2008) 392.

168    A. Ianculescu, D. Berger, C. Matei, P. Budrugeac, L. Mitoseriu and E. Vasile, *J. Electroceram* 24 (2010) 46.

169    X. D. Huang, J. K. O. Sin and P. T. Lai, *Solid State Electronics* 79 (2013) 285.

170    P. Keller, H. Ferkel, K. Zweiacker, J. Naser, J.-U. Meyer and W. Riehemann, *Sens. Actuators B* 57 (1999) 39.

171    D. Khomskii, *Physics* 2, 20 (2009).

172    L. W. Martin and D. G. Schlom, *Current Opin. Solid State Mater.* 16 (2012) 199.

173    M. Fiebig, *J. Phys. D: Applied Physics* 38 (2005) R123.

174    D. I. Khomskii, *J. Magn. Magn. Mater.* 306 (2006) 1.

175    R. Ramesh and N. A. Spaldin, *Nature Mater.* 6 (2007) 21.

176    S.-W. Cheong and M. Mostovoy, *Nature Mater.* 6 (2007) 1.

177    M. P. Singh, W. Prellier, L. Mechin, Ch. Simon and B. Raveau, *Thin Solid Films* 515 (2007) 6526.

178    K. F. Wang, J. M. Liu and Z. F. Ren, *Adv. Phys.* 58 (2009) 321.

179    K. Maaz, A. Mumtaz, S. K. Hasanain and A. Ceylan, *J. Magn. Magn.* 308 (2007) 289.

180    E. L. Salabas, A. Rumplecker, F. Kleitz, F. Radu and F. Schüth, *Nano. Lett.* 6 (2006) 2977.

181    P. Dutta, M. S. Seehra, S. Thota and J. Kumar, *J. Phys. Condens. Matter* 20 (2008) 015218

182    A. Minevich, Y. Marcus and L. Ben-Dor, *J. Chem. Eng. Data* 49 (2004) 1451.

183    M. Thommes: 'Physical Adsorption Characterization of Ordered and Amorphous Mesoporous Materials', in: G. Q. Lu, X. S. Zhao (Eds.), *Nanoporous Materials: Science and Engineering*, Imperial College Press, London, 2004, p. 317-364.

184    S. Lowell, J.E. Shields, M.A. Thomas, M. Thommes, *Characterization of Porous Solids and Powders: Surface Area, Pore Size and Density*, Springer/Kluwer Academics Publishers, 2004, Dordrecht (Netherlands), p. 129-154.

185    B. P. Feuston and J. B. Higgins, *J. Phys. Chem.* 98 (1994) 4459.

186    A. Galarneau, H. Cambon, F. Di Renzo, R. Ryoo, M. Choi and F. Fajula, *New. J. Chem.* 27 (2003) 73.

187    F. Kleitz, F. Bérubé, R. Guillet-Nicolas, C.-M. Yang and M. Thommes, *J. Phys. Chem. C* 114 (2010) 9344.

188    A. B. Fuertes, *Microporous Mesoporous Mater.* 67 (2004) 273.

189    A. Galarneau, H. Cambon, T. Martin, L.-C. De Ménorval, D. Brunel, F. Di Renzo and F. Fajula, *Stud. Surf. Sci. Catal.* 141 (2002) 395.

190    M. Kruk, M. Jaroniec, C. H. Ko and R. Ryoo, *Chem. Mater.* 12 (2000) 1961.

191    H. Tüysüz, C. W. Lehmann, H. Bongard, B. Tesche, R. Schmidt and F. Schüth, *J. Am. Chem. Soc.* 130 (2008) 11510.

192    S. Jun, S. H. Joo, R. Ryoo, M. Kruk, M. Jaroniec, Z. Liu, T. Ohsuna and O. Terasaki, *J. Am. Chem. Soc.* 122 (2000) 10712.

193    D. R. Lide (Ed.), *CRC Handbook of Chemistry and Physics,* 87th edition, CRC Press, Boca Raton, 2005.

194    R. Ryoo, S. H. Joo and S. Jun, *J. Phys. Chem. B* 103 (1999) 7743.

195    T. Waitz, *Ordered Mesoporous Oxides of Zinc, Indium and Tin: Synthesis by Structure Replication, Characterization and Gas Sensing*, Thesis, Gießen, 2009.

[196]  T.-J. Park, G. C. Papaefthymiou, A. J. Viescas, A. R. Moodenbaugh and S. S. Wong, *Nano Lett*. 7 (2007) 766.

[197]  Y. Ichiyanagi and S. Yamada, *Polyhedron* 24 (2005) 2813.

[198]  S. A. Makhlouf, *J. Magn. Magn. Mater.* 246 (2002) 184.

[199]  S. Ammar, A. Helfen, N. Jouini, F. Fiévet, I. Rosenman, F. Villain, P. Molinié and M. Danot, *J. Mater. Chem.* 11 (2001) 186.

[200]  S. Chikazumi, *Physics of Ferromagnetism*, Oxford University Press, Oxford, 2005, p. 503-517.

[201]  G. A. Sawatzky, F. van der Woude and A. H. Morrish, *J. Appl. Phys.* 39 (1968) 1204.

[202]  K. Haneda and A. H. Morrish, *J. Appl. Phys.* 63 (1988) 4258.

[203]  M. P. Pechini, *Method of Preparing Lead and Alkaline Earth Titanates and Niobates and Coating Method Using the Same to Form a Capacitor*, US 3.330.697, 1967.

[204]  A. Ianculescu, D. Berger, M. Viviani, C. E. Ciomaga, L. Mitoseriu, E. Vasile, N. Drăgan and D. Crişan, *J. Eur. Cer. Soc.* 27 (2007) 3655.

[205]  S. G. Rudisill, N. M. Hein, D. Terzic and A. Stein, *Chem. Mater.* 25 (2013) 745.

[206]  Q. Liu, A. Wang, X. Wang and T. Zhang, *Stud. Surf. Sci. Catal.* 170 (2007) 1819.

## LIST OF ABBREVIATIONS

BET        BRUNAUER, EMMETT and TELLER; method to determine the specific surface area

BJH        BARETT, JOYNER and HALENDA; method to determine the pore size distribution

$\chi_{mol}$        molar susceptibility

CMK        Carbon Mesostructured by Korea Advanced Institute of Science and Technology

EDX        Energy-dispersive X-ray spectroscopy

EISA        Evaporation-induced self-assembly

FC          field-cooled; measurement of magnetization in an applied field

FE          ferroelectricity

FM          ferromagnetism

FWHM      full width at half maximum

$H_C$        coercivity field

HDS        hydrodesulfurization

IUPAC      International Union of Pure and Applied Chemistry

JCPDS      Joint Committee on Powder Diffraction Standards

KIT          Korea Advance Institute of Science and Technology

$M_S$        saturation magnetization

$M_{spec}$      specific magnetization

MCM        Mobile Composition of Matter

NLDFT      non-local density functional theory

P-123      Pluronic 123

PEO        polyethylene oxide

PPO        polypropylene oxide

P-XRD      powder X-ray diffraction

SAED       selected area electron diffraction

SBA        University of California Santa Barbara

SDA        structure-directing agent

SEM        scanning electron microscopy

TEM        transmission electron microscopy

TLCT       true liquid-crystal templating

$T_{Néel}$    Néel temperature

TEOS       tetraethyl orthosilicate

THF        tetrahydrofurane

ZFC        zero-field-cooled; measurement of magnetization without an applied field

## LIST OF CHEMICALS

| SUBSTANCE | PICTOGRAM | HAZARD STATEMENTS | PRECAUTIONARY STATEMENTS |
|---|---|---|---|
| aluminum(III) nitrate nonahydrate | | H315-H319 | P305 + P351 + P338 |
| ammonia solution, 12.5 % | | H314-H335-H400 | P261-P273-P280-P305 + P351 + P338-P310 |
| barium carbonate | | H302 | |
| *n*-butanol | | H226-H302-H315-H318-H335 + H336 | P261-P280-P305 + P351 + P338 |
| citric acid | | H319 | P305 + P351 + P338 |
| cobalt(II) nitrate hexahydrate | | H272-H302-H317-H334-H341-H350i-H360-H410 | P201-P220-P261-P273-P280-P308 + P313 |
| ethanol | | H225 | P210 |
| hydrochloric acid, 32 % | | H290-H314-H335 | P280-P301 + P330 + P331 P305 + P351 + P338-P309 + P310 |
| hydrofluoric acid, 40 % | | H300-H310-H314-H330 | P260-P264-P280-P284-P301 + P310-P302 + P350 |
| iron(III) nitrate nonahydrate | | H272-H315-H319-H335 | P220-P261-P305 + P351 + P338 |
| Pluronic® P-123 | | | |
| sodium hydroxide | | H314 | P280-P305 + P351 + P338-P310 |
| sucrose | - | - | - |

| | | | |
|---|---|---|---|
| sulfuric acid, 3 % | | H314 | P280-<br>P305 + P351 + P338-<br>P310 |
| tetraethyl orthosilicate | | H226-H319-H322-H335 | P261-<br>P305 + P351 + P338 |
| tetrahydrofurane | | H225-H319-H335-H351 | P210-P261-P281-<br>P305+P351+P338 |
| titanium isopropoxide | | H226-H319-H331 | P261-<br>P305 + P351 + P338-<br>P311 |

## HAZARD STATEMENTS

| | |
|---|---|
| H225 | Highly flammable liquid and vapor. |
| H226 | Flammable liquid and vapor. |
| H272 | May intensify fire; oxidizer. |
| H290 | May be corrosive to metals. |
| H300 | Fatal if swallowed. |
| H302 | Harmful if swallowed. |
| H310 | Fatal in contact with skin. |
| H314 | Causes severe skin burns and eye damage. |
| H315 | Causes skin irritation. |
| H317 | May cause an allergic skin reaction. |
| H318 | Causes serious eye damage. |
| H319 | Causes serious eye irritation. |
| H330 | Fatal if inhaled. |
| H331 | Toxic if inhaled. |
| H332 | Harmful if inhaled. |
| H334 | May cause allergy or asthma symptoms or breathing difficulties if inhaled. |
| H335 | May cause respiratory irritation. |
| H335 + H336 | May cause respiratory irritation, and drowsiness or dizziness. |
| H341 | Suspected of causing genetic defects. |
| H350i | May cause cancer by inhalation. |
| H351 | Suspected of causing cancer. |
| H360 | May damage fertility or the unborn child. |
| H400 | Very toxic to aquatic life. |
| H410 | Very toxic to aquatic life with long lasting effects. |

PRECAUTIONARY STATEMENTS

| | |
|---|---|
| P201 | Obtain special instructions before use. |
| P210 | Keep away from heat/ sparks/ open flames/ hot surfaces – No smoking. |
| P220 | Keep/ Store away from clothing/ combustible materials. |
| P260 | Do not breathe dust/ fume/ gas/ mist/ vapors/ spray. |
| P261 | Avoid breathing dust/ fume/ gas/ mist/ vapors/ spray. |
| P264 | Wash hands thoroughly after handling. |
| P273 | Avoid release to the environment. |
| P280 | Wear protective gloves/ protective clothing/ eye protection/ face protection. |
| P281 | Use personal protective equipment as required. |
| P284 | Wear respiratory protection. |
| P301 + P310 | IF SWALLOWED: Immediately call a POISON CENTER or doctor/ physician. |
| P301 + P330 + P331 | IF SWALLOWED: rinse mouth. Do NOT induce vomiting. |
| P302 + P350 | IF ON SKIN: Gently wash with plenty of soap and water. |
| P305 + P351 + P338 | IF IN EYES: Rinse cautiously with water for several minutes. Remove contact lenses, if present and easy to do. Continue rinsing. |
| P308 + P313 | IF exposed or concerned: Get medical advice/ attention. |
| P309 + P310 | IF exposed or if you feel unwell: Immediately call a POISON CENTER or doctor/ physician. |
| P310 | Immediately call a POISON CENTER or doctor/physician. |
| P311 | Call a POISON CENTER or doctor/ physician. |

## LIST OF PUBLICATIONS

### REVIEW ARTICLES

- **Mesoporous Materials as Gas Sensors**
  T. WAGNER, S. HAFFER, C. WEINBERGER, D. KLAUS, M. TIEMANN
  *Chem. Soc. Rev.* 42 (2013) 4036-4053

### PEER-REVIEWED PAPERS

- **Towards Multiferroics: Synthesis of a Mesostructured $CoFe_2O_4$/$BaTiO_3$ Composite Material**
  S. HAFFER, C. LÜDER, T. WALTHER, R. KÖFERSTEIN, S. G. EBBINGHAUS, M. TIEMANN
  *Chem. Commun.* (2013) submitted

- **Nanoporous Materials: Synthesis Concepts and Model Experiments for School Chemistry Education**
  T. WILKE, S. HAFFER, C. WEINBERGER, M. TIEMANN, T. WAGNER, T. WAITZ
  *J. Nano Educ.* (2013) in press

- **Nanostructure-Related Magnetic Properties of Various Mesoporous Cobalt Oxide and Cobalt Ferrite Spinel Phases**
  S. HAFFER, T. WALTHER, R. KÖFERSTEIN, S. G. EBBINGHAUS, M. TIEMANN
  *J. Phys. Chem. C* 117 (2013) 24471-24478

- **Ordered Mesoporous $Al_2O_3$ by Nanocasting: Relation between Crystallinity and Mesoscopic Order**
  S. HAFFER, C. WEINBERGER, M. TIEMANN
  *Eur. J. Inorg. Chem.* (2012) 3283-3288

- **Mesoporöse Silica – Moderne Funktionsmaterialien im Chemieunterricht**
  T. WILKE, S. HAFFER, M. TIEMANN, T. WAITZ
  *Chemie Konkret* 19 (2012) 67-72

- **Periodic Mesoporous Organosilica (PMO) Materials with Uniform Spherical Core-Shell Structure**
  S. HAFFER, M. TIEMANN, M. FRÖBA
  *Chem. Eur. J.* 16 (2010) 10447-10452

- **Mesoporous $In_2O_3$ with Regular Morphology by Nanocasting: A Simple Relation between Defined Particle Shape and Growth Mechanism**
  S. HAFFER, T. WAITZ, M. TIEMANN
  *J. Phys. Chem. C* 114 (2010) 2075-2081

REPORTS AND EXTENDED ABSTRACTS

- **Porous Metal Oxides and Composites with Ferroic Properties**
  S. HAFFER, C. LÜDER, S. EBBINGHAUS, M. TIEMANN
  *Z. Anorg. Allg. Chem.* 638 (2012) 1577

- **Relation between Crystallinity and Mesoscopic Order of Mesoporous $Al_2O_3$**
  S. HAFFER, C. WEINBERGER, M. TIEMANN
  *Z. Anorg. Allg. Chem.* 638 (2012) 1578

- **One-Step Synthesis of Mesoporous Carbon Utilizing a Fructose Melt**
  C. WEINBERGER, S. HAFFER, M. TIEMANN
  *Z. Anorg. Allg. Chem.* 638 (2012) 1578

- **The Application of Learning Management Systems in Chemistry Teacher Trainees´ Practical Courses**
  K. WOLF, S. HAFFER, A. GEUTHER, H. BARTH, T. WAITZ
  *Ninth Multidisciplinary Symposium on the Design and Evaluation of Digital Content for Education,* University of Alicante (2012) 149-159

ORAL PRESENTATIONS

- **Mesoporous Cobalt Spinels with Structure-Related Magnetic Properties**
  S. HAFFER, C. LÜDER, T. WALTHER, S. EBBINGHAUS, M. TIEMANN
  $8^{th}$ International Mesostructured Materials Symposium, 20.-24.05.2013, Awaji Island, Hyogo, Japan

- **Mesoporous Cobalt Spinels: Synthesis by Nanocasting and Magnetic Properties**
  S. HAFFER, C. LÜDER, R. KÖFERSTEIN, T. WALTHER, S. EBBINGHAUS, M. TIEMANN
  25. Deutsche Zeolith-Tagung, 06.-08.03.2013, Hamburg

POSTER PRESENTATIONS

- **Mesoporous Cobalt Spinels with Structure-Related Magnetic Properties**
  S. HAFFER, M. TIEMANN, T. WALTHER, S. EBBINGHAUS
  MRS Fall Meeting 2013, 01.-06.10.2013, Boston, USA

- **Formation Mechanism of Ordered Mesoporous $Al_2O_3$: Relation between Mesoscopic Order and Crystallinity**
  C. WEINBERGER, S. HAFFER, M. TIEMANN
  ACS Northeast Regional Meeting 2013, 23.-26.10.2013, New Haven, USA

- **Ordered Mesoporous Carbon Materials from Novel Molten Precursor containing Nitrogen**
  C. WEINBERGER, S. HAFFER, T. WAGNER, M. TIEMANN
  ACS Northeast Regional Meeting 2013, 23.-26.10.2013, New Haven, USA

- **Temperature-Dependent CO Sensing Properties of Nanoporous $Co_3O_4$: Identification of Distinct Reaction Mechanism**
  S. Vetter, S. Haffer, M. Tiemann, T. Wagner
  EnFI-2013 Engineering of Functional Interfaces, 08.-09.07.2013, Hasselt, Belgium

- **Formation Mechanism of Ordered Mesoporous $Al_2O_3$: Relation between Crystallinity and Mesoscopic Order**
  S. Haffer, C. Weinberger, M. Tiemann
  8th International Mesostructured Materials Symposium, 20.-24.05.2013, Awaji Island, Hyogo, Japan

- **Nitrogen Containing Ordered Mesoporous Carbon from Novel Precursor Mixtures**
  C. Weinberger, S. Haffer, T. Wagner, M. Tiemann
  8th International Mesostructured Materials Symposium, 20.-24.05.2013, Awaji Island, Hyogo, Japan

- **Nitrogen-Containing Ordered Mesoporous Carbon Prepared by Nanocasting Using Precursor Melts**
  C. Weinberger, S. Haffer, T. Wagner, M. Tiemann
  25. Deutsche Zeolith-Tagung, 06.-08.03.2013, Hamburg

- **Porous Metal Oxides and Composites with Ferroic Properties**
  S. Haffer, C. Lüder, S. Ebbinghaus, M. Tiemann
  16. Vortragstagung Fachgruppe Festkörperchemie und Materialforschung, 17.-19.09.2012, Darmstadt

- **Relation between Crystallinity and Mesoscopic Order of Mesoporous $Al_2O_3$**
  S. Haffer, C. Weinberger, M. Tiemann
  16. Vortragstagung Fachgruppe Festkörperchemie und Materialforschung, 17.-19.09.2012, Darmstadt

- **One-Step Synthesis of Mesoporous Carbon Utilizing a Fructose Melt**
  C. Weinberger, S. Haffer, M. Tiemann, T. Wagner
  16. Vortragstagung Fachgruppe Festkörperchemie und Materialforschung, 17.-19.09 2012, Darmstadt

- **Straightforward One-Step Synthesis for Mesoporous Carbon Utilizing a Fructose Melt**
  C. Weinberger, S. Haffer, M. Tiemann
  24. Deutsche Zeolith-Tagung, 07.- 09.03.2012, Magdeburg

- **Ordered Mesoporous $Al_2O_3$ by Nanocasting: Relation between Crystallinity and Mesoscopic Order**
  S. Haffer, C. Weinberger, M. Tiemann
  24. Deutsche Zeolith-Tagung, 07.- 09.03.2012, Magdeburg

- **Mesoporous Ternary Metal Oxides and Composites with Ferroic Properties**
  S. Haffer, C. Lüder, S. Ebbinghaus, M. Tiemann
  24. Deutsche Zeolith-Tagung, 07.- 09.03.2012, Magdeburg

- **Semiconducting Metal Oxides as Gas-Sensors in Chemistry Education: Function and School Experiments**

  S. HAFFER, T. WAITZ

  11. Europäischer Chemielehrerkongress, 27.- 30.04.2011, Klagenfurt

- **Porous Materials in the Didactics of Chemistry: An Interdisciplinary Topic at Both School and University Level**

  T. WAITZ, S. HAFFER, T. WAGNER, M. TIEMANN

  23. Deutsche Zeolith-Tagung, 02.- 04.03.2011, Erlangen

- **Mesoporous Carbon as an Electrode Material for Lithium-Sulfur Batteries**

  S. DIEGELMANN, J. JANEK, S. HAFFER, M. TIEMANN

  23. Deutsche Zeolith-Tagung, 02.- 04.03.2011, Erlangen

- **Spherical Mesoporous Materials by Nanocasting: Strategies of Morphology Control**

  S. HAFFER, M. TIEMANN

  23. Deutsche Zeolith-Tagung, 02.- 04.03.2011, Erlangen

- **The Performance of Different Carbon Materials as Electrodes for Lithium Ion Batteries**

  S. DIEGELMANN, S. HAFFER, T. WAITZ, M. TIEMANN, J. JANEK

  15th International Meeting on Lithium Batteries, 27.06.-02.07.2010, Montreal, Canada

- **Mesoporous In$_2$O$_3$ with Controlled Morphology and Promising Gas-Sensing Properties**

  T. WAITZ, S. HAFFER, M. TIEMANN

  22. Deutsche Zeolith-Tagung, 03.- 05.03.2010, München

- **Mesoporous Metal Oxides by Structure Replication: Investigation of the Growth in Porous Silica Matrices**

  S. HAFFER, T. WAITZ, M. TIEMANN

  22. Deutsche Zeolith-Tagung, 03.- 05.03.2010, München

- **Spherical Silica and Organosilica Materials with Core-Shell Structure**

  S. HAFFER, M. FRÖBA, M. TIEMANN

  Materialforschungstag Mittelhessen 2009, 10.07.2009, Giessen

- **Spherical Silica and Organo-Silica Materials with Solid Core and Mesoporous Shell**

  S. HAFFER, M. FRÖBA, M. TIEMANN

  21. Deutsche Zeolith-Tagung, 04.- 06.03.2009, Kiel